![University of South-Eastern Norway logo]

**University of
South-Eastern Norway**

**FMH606 Master's Thesis 2024
Electrical Power Engineering**

Utilizing novel laser scanning techniques to anticipate PD inception voltages in HV cable interfaces

Harald Korpås

Faculty of Technology, Natural Sciences and Maritime Sciences

Campus Porsgrunn

University of South-Eastern Norway

www.usn.no

Course: FMH606 Master's Thesis 2024
Title: *Utilizing novel laser scanning techniques to anticipate PD inception voltages in HV cable interfaces*
Pages: *108*
Keywords: *PDIV, Paschen's Law, laser scanning, COMSOL*

Student: *Harald Korpås*
Supervisor: *Elin Fjeld*
External partner: *Nexans Norway AS*

Summary:

High-voltage (HV) cable systems are the foundation for the transmission of electricity, but they are susceptible to partial discharges (PD), particularly at joint locations, which can cause insulation failure leading to breakdown.

This thesis investigates the potential of advanced laser scanning techniques, combined with simulations and calculations, to predict and mitigate such discharges by identifying the voltage levels at which they initiate. The predicted voltages were compared with empirical testing results to validate the methodology used.

Utilizing a HandySCAN BLACK™|Elite handheld 3D scanner, the study generated detailed 3D models of deliberately implemented cuts in cable insulation. These models were analyzed to derive the depths of the cuts, which were used in electric field simulations to calculate the Field Enhancement Factor (FEF), quantifying the increase in electric field intensity due to the defects. Subsequent calculations of Partial Discharge Inception Voltage (PDIV) were based on these FEFs and Paschen's Law to predict the voltage at which PD would initiate. Empirical tests measured the PDIV of the physical cable end, validating the accuracy of the simulation model through comparison. The findings confirm the effectiveness of using 3D laser scanning for defect detection and subsequent simulations and calculations for PDIV estimations, indicating significant enhancements in HV cable installation processes and quality control.

Preface

This thesis is the result of work on the Master's degree in Electrical Power Engineering, conducted at the University of South-Eastern Norway, campus Porsgrunn. The thesis is written during the spring of 2024.

I am very grateful for the support, guidance, and contributions from multiple individuals making this work possible. Firstly, I would like to thank my supervisor, Elin Fjeld, for her insightful feedback and constructive suggestions for writing and structuring the report.

A special thanks goes to the team at Nexans' HV lab. To all the technicians who assisted with the laboratory setups, making the experiments possible. To Jostein-Marken Mjølnerød, whose insights into both theoretical problems, as well as practical work were invaluable. Furthermore, I want to thank Espen Doedens at the R&D department for his deep technical knowledge and our enriching discussions around the theory behind this work.

Lastly, my heartfelt thanks to my family, and especially my fiancée, who has been my devoted support through the challenges that arose in the work of this thesis. Your support was essential in maintaining my motivation and focus throughout this journey.

Porsgrunn, 15th May 2024

Harald Korpås
Harald Korpås

Contents

List of Figures

7

List of Tables

Nomenclature

Abbreviation	Explanation
3D	Three-dimensional
AC	Alternating Current
BEM	Boundary Element Method
CAD	Computer-Aided Design
CB	Carbon Black
EPDM	Ethylene Propylene Diene Monomer
FDM	Finite Difference Method
FEF	Field Enhancement Factor
FEM	Finite Element Method
GIS	Gas-insulated switchgear
HFCT	High Frequency Current Transformer
HV	High-Voltage
HVAC	High-Voltage Alternating Current
IEC	International Electrotechnical Commission
kV	kilovolt
LiDAR	Light Detection And Ranging
PD	Partial Discharge
PDIV	Partial Discharge Inception Voltage
PMJ	Pre-molded Joint
PRPD	Phase Resolved Partial Discharge
PSA	Pulse Sequence Analysis
SiR	Silicone Rubber
STL	Stereolithography
Surfical	Surface Inspection and Control Algorithms
TOF	Time of flight
UHF	Ultra-high frequency
UV	Ultraviolet
XLPE	Cross-linked polyethylene

1 Introduction

1.1 Background

High-voltage (HV) cable systems are the foundation of modern electricity transmission, yet their safety and operational efficiency are compromised by the occurrence of partial discharges (PD). PD often occurs from minuscule defects or geometric irregularities in the insulation, particularly at the material interfaces in the cable system, such as those encountered during jointing and termination processes [1]. These processes are often performed on-site and are therefore not always subjected to the same rigorous protocols as when manufactured in the factory for practical reasons. The defects that may arise during these processes are preferably detected by the operator and removed or fixed.

The introduction of 3D laser scanning technology provides a promising solution for enhancing quality control in HV cable preparation and installation. This technology is widely used in fields such as reverse engineering and quality control [2], and its high precision and adaptability make it exceptionally suited for detecting defects that could potentially lead to PD [3]. These capabilities are essential in managing the risks associated with the manual preparation of HV cable ends, where even skilled execution can introduce inconsistencies that result in sites susceptible to PD initiation [1].

To mitigate the risk of this, a digital process involving the laser scanning of cable ends has been developed [4]. This process includes subsequent mathematical processing and field calculation to compute local PD inception voltages for cavities. This could provide operators with immediate go/no-go criteria based on the calculated local field enhancements, which are critical indicators of the reliability of the cable interface. While this methodology may have shown promise, proof and calibration of its effectiveness remain necessary.

1.2 Previous work

Recent studies have emphasized the utilization of 3D scanning technology in quality control across various industries. A notable case study [5] investigated the use of 3D scanning as a verification method in technical quality control. In their study, they detailed the usage of a 3D scanner to evaluate the technical specifications of projectiles by comparing scanned models to pre-existing Computer-Aided Design (CAD) models. The research highlighted the precision and efficiency of 3D scanning in detecting minuscule deviations and irregularities, thus supporting its potential to enhance quality control processes. Despite the positive outcomes, the case study also emphasized the need for precise scanner settings and thorough surface preparation to mitigate issues such as gaps that are not detected by scanner light, which are typically filled in by software approximations.

Furthermore, a recent study specifically addressed the application of 3D scanning technology to HV cable joints [6]. This research developed an innovative method that combines point cloud remapping with image segmentation to effectively measure and quantify surface defects on manually polished cross-linked polyethylene (XLPE) cable joints. The study addressed challenges like low detection accuracy due to weak textures and strong reflections on cable joint surfaces. By using a modified radius filtering algorithm to refine disordered point clouds and a method to enhance feature visibility from point clouds, the approach significantly improved the precision in identifying and measuring defects. The effectiveness of this method was confirmed through extensive experiments on both simulated and actual cable joints, which showed substantial enhancements in defect detection and quantification compared to traditional methods. These advancements mark a significant step forward in quality assurance techniques for HV cable installations.

While 3D scanning has been researched for quality control and defect detection, predictive modeling of the Partial Discharge Inception Voltage (PDIV) has been studied as well. A notable study [7] utilized Finite Element Method (FEM) simulations to obtain electric potential values, which were compared with values given by Paschen's Law to predict PDIV in motor coils constructed with enameled wire. This approach improved the precision of PDIV predictions by incorporating actual electric field line lengths and considering various physical and environmental parameters such as electrode material, gas pressure, and gap distance between electrodes. In addition, [8] investigated PDIV in medium voltage cable accessories through experimental and theoretical approaches. The study utilized hollow glass microspheres embedded in silicone to simulate defects and subjected these to varying electric fields at different frequencies to empirically determine PDIV. The theoretical estimation of PDIV incorporated Paschen's Law and the Field Enhancement Factor (FEF). Further, FEM simulations were utilized to analyze field enhancements, providing an understanding of the factors influencing PD inception in practical scenarios.

1.3 Objective

The primary objective of this thesis is to investigate how laser scanning technology can be used to predict the PDIV of defects at HV cable ends through both simulations and actual PDIV measurements.

To achieve this objective, the thesis is structured around several specific sub-objectives:

1. **Defect introduction and detection**

   - Intentionally introduce controlled defects in the form of cuts on the insulation surface of a prepared HV cable end to simulate common on-site issues.

   - Use 3D laser scanning technology to detect these defects accurately and create precise 3D models for detailed geometrical analysis.

2. **PDIV measurements**

   - Conduct empirical testing to determine the PDIV for the cable end with the introduced defects.

3. **Simulations and calculations**

   - Perform electric field simulations based on the cuts in the cable end insulation, to find the Field Enhancement Factor (FEF) caused by these cuts under various conditions.

   - Do calculations to predict the PDIV based on the FEF from these simulations.

4. **Comparison of predicted and empirical data**

   - Compare the PDIV predicted from simulations and calculations with the PDIV measured during empirical testing to validate the accuracy and effectiveness of the 3D scanning technology in predicting PD initiation in HV cables.

1.4 Limitations

- The study is limited to examining cuts as the only type of defect and focuses on just one defect at a time on a single cable end. This limits the generalizability of the findings to other defect types or multiple defects on the same cable end.

- The thesis focuses exclusively on PDIV measurements. It does not consider the apparent charge, which might provide additional insights into the severity and characteristics of the discharges.

- Details regarding the preparation of the cable, 3D scanning, and other laboratory procedures are confidential and, therefore, are not disclosed in this thesis, and may limit the reproducibility of the study.

2 Theory

This chapter lays the foundational theory relevant to the research conducted in this thesis. It begins with an overview of HV power cables and their components, followed by electric field theory and its behavior. Subsequently, the mechanisms of air breakdown are explained, before the PD phenomena, along with methods for their detection and analysis are presented. Lastly, the principles of 3D laser scanning technology are described.

2.1 The high-voltage power cable

HV power cables are fundamental in electrical power systems, enabling the transmission of electricity over long distances. The design of HV cables includes a central conductor insulated by a material capable of withstanding high electrical stress. In general, HV cables can be categorized into paper-insulated and plastic-insulated categories.

These cables are used in various contexts, from underground and underwater transmission to the interconnection of electrical substations, designed to operate at various voltage levels. A significant advancement in their technology was the introduction of XLPE as the insulating material, which has improved HV cable design due to its superior properties. This section will focus on plastic-insulated cables, highlighting their structural design and the roles of these layers in the cables' functionality and reliability in HV applications [9].

2.1.1 The components of a plastic-insulated HV cable

Figure 2.1 provides a general illustration of the components in an HV plastic-insulated power cable, demonstrating the arrangement of layers from the conductor to the outer jacket. Each component is specifically designed to serve a unique purpose, ensuring safe operation under HV conditions.
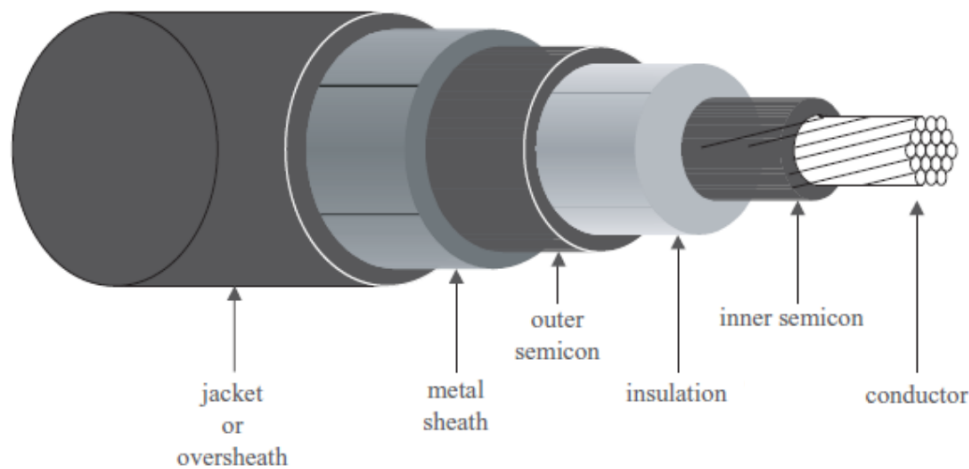
Figure 2.1: General illustration of an HV plastic-insulated power cable [9]

The conductor

The main task of the conductor is to efficiently transfer electrical energy. The effectiveness of an electrical conductor is determined by the ability of electrons to move freely between atoms. The conductor is primarily made of copper or aluminum, where the selected metal is based on various factors like weight, cost, and specific transmission needs. Aluminum is widely used for its affordability and lightness, whereas copper is chosen for high-demand scenarios or where flexibility is an important factor [10].

Copper stands out for its superior conductivity, ease of handling due to its flexibility, and its natural corrosion resistance. On the other hand, aluminum, though less conductive and more susceptible to corrosion when exposed to moisture, benefits from a protective oxide layer that forms on its surface. This layer, while protective, requires careful handling during installation to ensure effective electrical connections. Despite its drawbacks, aluminum's cost-effectiveness and lighter weight make it a viable option as a conductor material [10].

Inner and outer semiconductor

The semiconductive layers, commonly referred to as semicons or semiconductors, serve as essential components in bridging the conductive and insulating parts of a power cable. These layers are divided into the inner semiconductor, which interfaces between the cable conductor and its insulation, and the outer semiconductor, which interfaces between the insulation and the metal sheath.

The primary role of the inner semiconductor is to even out surface irregularities and eliminate air pockets between the conductor and insulation. This is essential for ensuring a uniform distribution of the electric field across the insulation layer, significantly reducing the risk of PD and further degradation of the insulation.

Similarly, the outer semiconductor serves the same role as the inner layer, by smoothing out irregularities between the insulation and the metal sheath. This effectively encloses the electric field within the insulation, aiding in a uniform radial distribution of electric field lines. Both semiconductive layers are typically vulcanized together with the insulation, making it necessary to utilize specialized tools for their removal.

The semiconductors consist of a polymer blend, containing XLPE in the case of XLPE-insulated cables, combined with carbon black (CB). CB is highly conductive, giving the semiconductor its conductive properties while maintaining the thermal characteristics of XLPE. The right amount of CB in the blend ensures that the layers maintain consistent conductivity, which is important for managing the electric fields [10].

Insulation

The primary function of the insulation in HV power cables is to act as an effective barrier between conducting surfaces with significant potential differences. The insulation needs to be clean and free from defects to maintain its structural integrity and functional performance. Additionally, the insulation must possess mechanical strength, be resistant to temperature variations, and demonstrate long-term durability.

XLPE is a preferred insulation material due to its superior properties. Unlike standard polyethylene (PE), which softens and melts around 80-110 °C, XLPE maintains its structural integrity at higher temperatures, displaying high dielectric strength until it undergoes pyrolysis at temperatures above 300°C. XLPE is developed from PE through the addition of organic peroxides, followed by extrusion around the cable's conductor in a high-pressure, high-temperature environment. This process is done to prevent the formation of gas bubbles within the insulation, which could weaken the material and lead to PD or complete dielectric breakdown [11].

Metal sheath

The metal sheath protects the insulation from water ingress, necessary for maintaining the insulation's dielectric strength. These sheaths are typically made of aluminum, lead, or copper, each chosen for their protective properties and specific application.

Lead sheaths provide excellent protection against water and humidity. However, the density of lead also adds significant weight to the cables, which, while beneficial in stabilizing submarine cables on the seafloor, can pose challenges during the installation of land cables. Additionally, lead is a soft material and must be protected against mechanical damage. It is susceptible to fatigue due to vibrations, repeated bending, and thermal cycling, which can lead to the formation of cracks. Such damage can compromise the integrity of the sheath, potentially affecting the cable's overall water-tightness and durability [11].

Jacket

The jacket, also known as the oversheath or outer sheath, serves to mechanically and chemically protect the inner layers of the cable. The most commonly used materials for the jacket are plastics, typically PE or polyvinyl chloride (PVC). PE is favored for its stability against aging, low water absorption, and minimal chemical and biological reactivity. Additionally, it is recyclable and resistant to ultraviolet (UV) light [10].

2.1.2 Joints and terminations in high-voltage cable systems

Pre-molded joints (PMJ) are accessories that ensure secure and durable connections between cable segments. They consist of multiple semi-conductive and insulating materials, designed for high electrical stresses and durability. Their construction allows for quick and reliable connections, which is particularly beneficial during repairs or cable jointing in the field. These joints are fabricated and assembled under controlled factory conditions, where they undergo comprehensive testing, including PD tests, to ensure that they are free from defects.

The PMJs are also compatible with various conductor connections, such as welding, compression sleeves, and screw connectors. Furthermore, the alignment of the joint is made easy due to its expandable body, which contracts after installation to maintain radial pressure on the jointed cable segments [11].

Figure 2.2 illustrates the electrical layers of an HV cable joint utilizing a PMJ body. The insulating materials in PMJs are usually rubbers, such as ethylene propylene diene monomer (EPDM) and silicone rubber (SiR) [12].
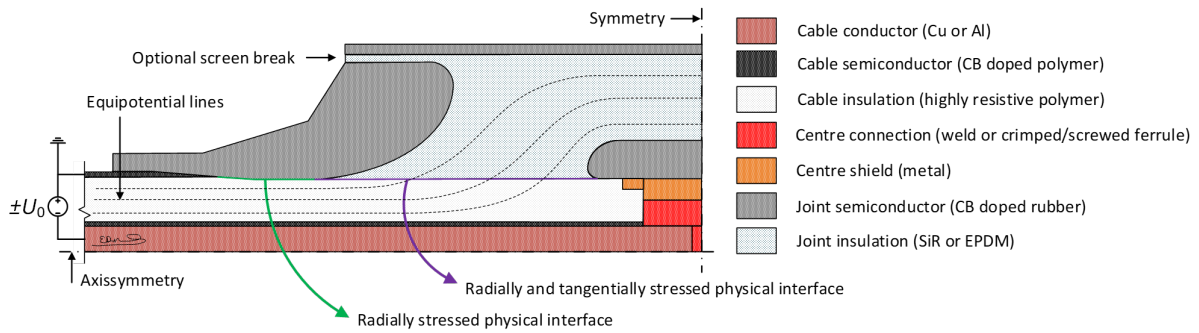
Figure 2.2: General illustration of an HV cable joint, using a PMJ body (not to scale) [12]

Terminations are accessories that connect the ends of HV cables to other electrical infrastructure, such as bus bars, gas-insulated switchgear (GIS), and overhead lines, ensuring secure and efficient electrical connections.

Terminations are categorized based on their insulation and sealing mechanisms into fluid-filled, gas-insulated, and dry types. Fluid-filled and gas-insulated types are favored for their ability to handle environmental variations and thermal stresses, while dry types are valued for their maintenance-free operation and environmental friendliness. Figure 2.3 illustrates a simplified model of a gas-insulated or fluid-filled termination.
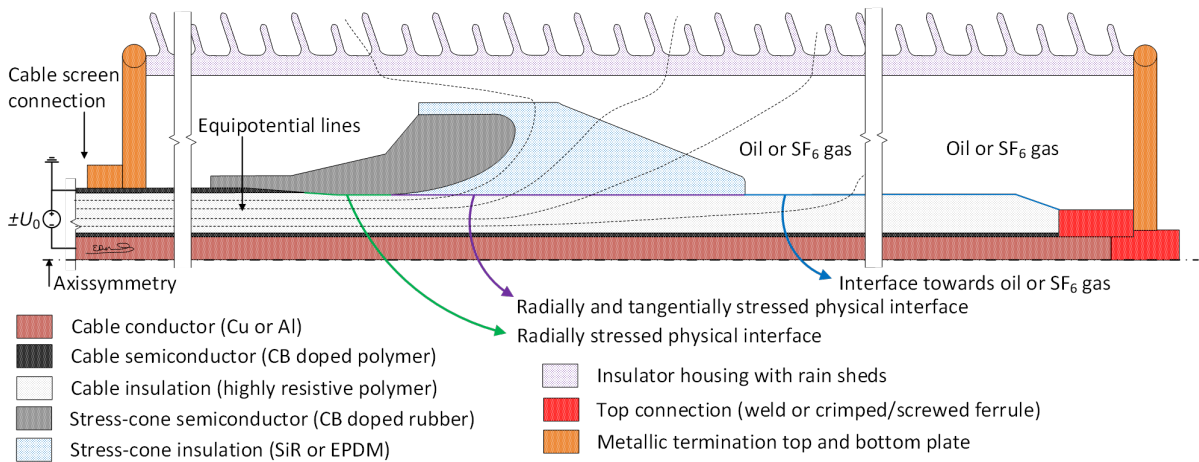
Figure 2.3: General illustration of an HV cable termination (not to scale) [12]

Similar to PMJs, these terminations incorporate a stress cone that employs geometric field control. These are designed for managing the electric stress at the point where the cable insulation terminates, ensuring that the electrical field is distributed evenly and preventing high field concentrations.

19

Managing the interface between cable ends and the accessories presents a significant challenge. Minor geometric deviations can create air pockets, weakening the insulation's integrity. To prevent this, a medium such as grease or oil is used, aiding in proper fitting and enhancing the overall reliability of the installation. Additionally, the stress cone is designed to maintain steady contact pressure through its radial extension, increasing the strength of the interface and ensuring operational reliability [12] [13].

2.2 The electric field

An electric field is a vector field that surrounds a charged particle, representing the force that other charged particles would experience within its vicinity. The strength and direction of this field ($\vec{E}$) can be described by (2.1).

$$\vec{E} = \frac{\vec{F}}{q_0} \tag{2.1}$$

where $\vec{F}$ is the force experienced by the test charge q_0. The direction of $\vec{E}$ is determined by the force acting on a charge [14].

The electric field can be visualized by electric field lines, which provide a representation of its behavior. These lines are directed outwards from positive charges and inwards to negative charges. Additionally, they never intersect, providing a consistent direction and magnitude of the field at any given point. The density of these lines is indicative of the field's strength, whereas closely spaced lines indicate a stronger field [14]. Figure 2.4 visualizes the electric field by field lines of an electric dipole.
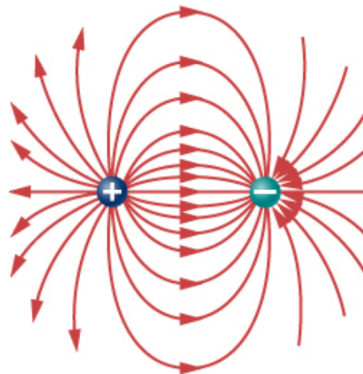
Figure 2.4: Visualization of the electric field through field lines of an electrical dipole [15].

2.2.1 Relation between electric potential and electric fields

The electric field is connected to the electric potential, where the electric potential (V) at a point indicates the electric field strength at that location, and the change in electric potential across space is what creates the electric field, expressed mathematically by (2.2).

$$\vec{E} = -\nabla V \qquad (2.2)$$

This equation reveals that the electric field vector, $\vec{E}$, points in the direction where the potential decreases most rapidly and its magnitude is proportional to the rate of decrease of potential with distance.

In dielectrics, the concept of the electric field is expanded to include the electric flux density or electric displacement field, $\vec{D}$. This field adapts the idea of electric fields to account for how the dielectric reacts to the electric field and is given by (2.3), where ε is the relative permittivity of the dielectric.

$$\vec{D} = \varepsilon \vec{E} \qquad (2.3)$$

The displacement field is linked to the volume charge density, ρ_v. The divergence of the displacement field then leads to Poisson's equation (2.4).

$$\nabla \cdot \vec{D} = \rho_v \longrightarrow \nabla^2 V = -\frac{\rho_v}{\varepsilon} \qquad (2.4)$$

When there are no free charges within a region, such as in the insulating materials of HV systems, Poisson's equation simplifies to Laplace's equation (2.5) [16].

$$\nabla^2 V = 0 \qquad (2.5)$$

2.2.2 Electric field distribution in coaxial cylinders

Gauss's Law establishes a relationship between the electric flux passing through a closed surface and the net charge enclosed within it, making it particularly useful for calculating electric fields in symmetrical geometries, such as cylinders. The formal expression of Gauss's Law in integral form is given by (2.6).

$$\Phi_E = \oint \vec{E} \cdot d\vec{A} = \frac{Q_{encl}}{\varepsilon_0} \qquad (2.6)$$

where Φ_E is the electric flux through a closed surface, $\vec{E}$ is the electric field vector, $d\vec{A}$ is the vector area element of the closed surface, and ε_0 is the permittivity of vacuum, quantified as $8.854 \cdot 10^{-12} \frac{C^2}{N \cdot m^2}$ [14].

In coaxial cylinders, the electric field distribution is influenced by this symmetry, resulting in force lines that radially extend outward from the cylinder's axis. This configuration allows the magnitude of the electric field, E, to vary only with the radial distance, x, from the central axis, as visualized in Figure 2.5.
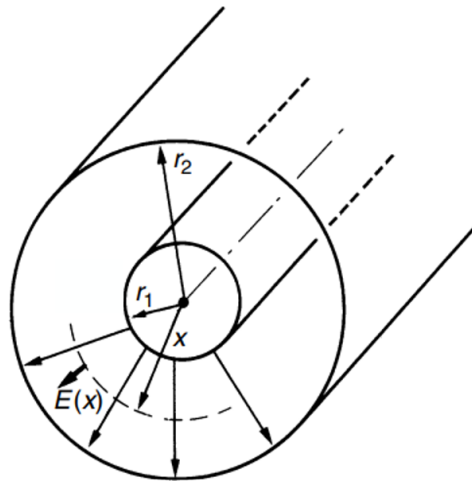
Figure 2.5: Representation of the electric field in a coaxial cylinder [17].

Assuming uniform charge distribution across the surfaces of the cylinders, with a charge per unit length λ, and a voltage V applied across the electrodes, Gauss's Law can be used to derive the electric field intensity at any radial distance x by (2.7).

$$E(x) = \frac{\lambda}{2\pi\varepsilon} \cdot \frac{1}{x} = \frac{V}{\ln(\frac{r_2}{r_1})} \cdot \frac{1}{x} \quad [\text{V/m}] \tag{2.7}$$

where λ represents the charge per unit length (C/m), ε is the permittivity of the material between the cylinders (F/m), V is the applied voltage (V), r_1 and r_2 is the radius of the inner and outer cylinder (m), and x is the radial distance from the center (m) [17].

2.2.3 Numerical methods for electric field and potential distribution

For calculating the electric field and potential in unsymmetrical and complicated geometries, numerical methods are commonly used for solving Poisson's (2.4) and Laplace's (2.5) equations. These methods are also beneficial when dealing with two- or three-dimensional

fields that have complicated boundary conditions or are within materials with variable permittivities and conductivities. The most commonly utilized numerical methods are:

- **Finite Difference Method (FDM):**
  This method organizes the problem area into a grid. At each grid intersection, a Taylor expansion of the differential equations is used to derive numerical equations, which are typically solved using iterative methods. While effective for two-dimensional geometries, its accuracy diminishes with the inclusion of curved or irregular three-dimensional volumes.

- **Finite Element Method (FEM):**
  FEM transforms complex domains into manageable subdivisions, simplifying the approximation of field quantities within discretized elements that can vary in physical properties. It converts partial differential equations into algebraic expressions through the minimization of an energy functional, leading to a sparse matrix that allows for efficient computational solutions.

- **Boundary Element Method (BEM):**
  BEM simplifies problems by modeling only the surfaces of regions, using one- or two-dimensional elements, thus reducing computational complexity and eliminating the need to discretize air spaces.

Each method comes with its unique set of advantages and limitations, and often they are used in a complementary fashion depending on the specific problem at hand [9]. This section will focus on FEM due to its extensive use in the field and this thesis.

Finite Element Method (FEM)

FEM discretizes the domain of complicated geometries into a finite set of subdomains called elements, which enables a piecewise approximation of the potential V.
The electric potential V is then approximated by minimizing an energy functional for each element. Assuming constant permittivity and absence of charge density, reducing Poisson's equation to Laplace's equation, the energy functional for a two-dimensional domain is given by (2.8).

$$F = \frac{\varepsilon}{2} \iint \left(\left(\frac{\partial V}{\partial x}\right)^2 + \left(\frac{\partial V}{\partial y}\right)^2 \right) dx, dy \qquad (2.8)$$

This functional represents the stored electric energy and its minimization with respect to the potential at the nodes of the elements, producing a system of algebraic equations. When solved, these equations provide the distribution of the electric potential V over

the entire mesh by ensuring the potential is continuous across element boundaries and satisfies the governing differential equations.

Figure 2.6 illustrates a completed FEM mesh of the cross-section of a simplified HV cable, showing how the computational domain is discretized into triangular elements.
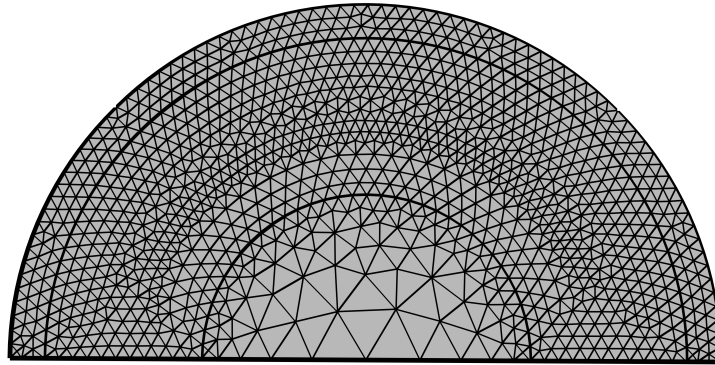
Figure 2.6: Mesh of a simplified HV cable's cross-section in 2D, utilizing triangular elements of different sizes.

All elements in the mesh are connected through shared nodes, as shown in Figure 2.7, which shows the typical connectivity at a common node i in a FEM mesh. Each node receives potential contributions from every connected element, ensuring a continuous solution across the entire domain and compliance with the governing differential equations.
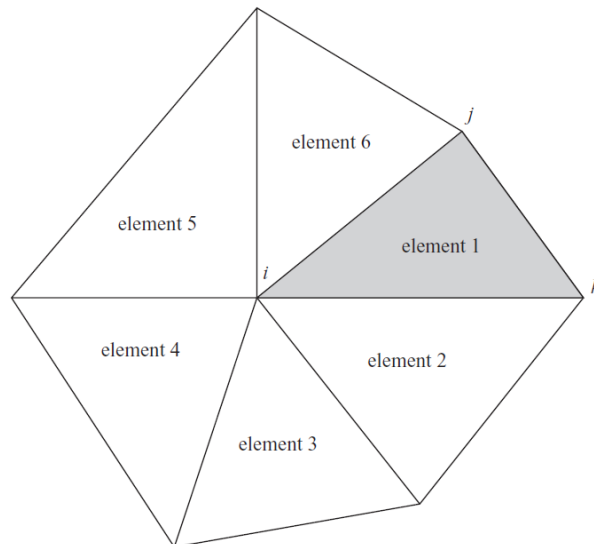
Figure 2.7: The connections of triangular elements at a common node i in a FEM mesh, illustrating the potential contributions from each bordering element [9].

For node i, the relationship with the neighboring elements is expressed by (2.9).

$$\frac{\partial F}{\partial V_i} = \sum_e \frac{\partial F_e}{\partial V_i} \qquad (2.9)$$

Where the sum of the contributions from the elements connected to node i is represented by $\sum_e$. Based on this equation, the global stiffness matrix $[S]$ and the nodal potential vector $\{V\}$ are assembled, resulting in the system equation (2.10).

$$[S]\{V\} = 0 \qquad (2.10)$$

Where the stiffness matrix $[S]$ represents how the nodes are connected and is derived from the geometric and material properties of the mesh. This leads to a sparse matrix that is computationally efficient for solving large-scale problems [9].

2.2.4 Electric field distribution in various geometries

The distribution of electric fields over different geometric configurations can significantly influence the local field intensities due to the geometry's features, such as edges or corners. In the context of HV cables, local surface irregularities can distort the electric field distribution, creating areas of increased or decreased field strength. The Field Enhancement Factor (FEF) quantifies the local variation in electric field strength caused by these irregularities. It provides a means to analyze how surface features affect field intensity without altering the bulk material properties [12]. The FEF can be expressed by (2.11).

$$FEF = \frac{E_{local}}{E_{reference}} \qquad (2.11)$$

where E_{local} represents the local electric field intensity at a specific point on the surface that includes irregularities, and $E_{reference}$ is the electric field intensity at the same point under idealized conditions, considering no surface imperfections.

Surface roughness and geometry play pivotal roles in the local redistribution of the electric field. This redistribution occurs because the electric field lines are normal to the conductor's surface, and any deviation in this surface can either concentrate or disperse the field lines. Consequently, regions with acute protrusions or indentations often exhibit higher local field strengths due to the concentration of field lines, leading to higher FEF values. Conversely, smoother or more gradually curved areas might show a decrease in local field intensity, hence a lower FEF [12].

2.3 Breakdown of air

The electrical breakdown of air signifies a transition where air ceases to be an insulator and becomes conductive. This phenomenon is caused by the electric field reaching a threshold that enables a series of ionization events, fundamentally changing the dielectric properties of air [9].

2.3.1 The Townsend Mechanism

The Townsend mechanism further explains how these ionization events occur, leading to the breakdown of air. When charged particles, such as electrons, are subjected to intense electric fields, they can accumulate sufficient kinetic energy to ionize neutral molecules upon collisions. This energy accumulation and following ionization initiate with primary electrons near the cathode, which are forced toward the anode by the electric field. As these electrons move, they ionize the neutral molecules, leading to an exponential increase in electron numbers and the creation of positive ions, known as an electron avalanche. These ions then migrate back towards the cathode, inducing secondary electron emission upon collision with the electrode surface. This interaction of primary and secondary processes, which includes both ionizing and non-ionizing collisions, is central to Townsend's theory [16] [18].

To describe these phenomena, Townsend proposed three specific coefficients, which he then combined to formulate the criteria for electrical breakdown in gases. These coefficients were:

- **The first Townsend coefficient (α)**
  Often referred to as the ionization coefficient, represents the number of additional electrons one electron generates per unit path length in the electric field's direction.

- **The second Townsend coefficient (β)**
  This coefficient describes the ionization caused by the positive ions during breakdown. However, this coefficient was found to be less important, because the energy of an ion is too low to effectively ionize a neutral gas. Therefore, $\beta \approx 0$ is generally assumed.

- **The third Townsend coefficient (γ)**
  This coefficient is known as the secondary electron emission coefficient, which quantifies the number of secondary electrons emitted from a surface per incident particle that bombards the surface [18].

The Townsend breakdown criterion is formulated from these coefficients and is given by the condition when the growth of the electron avalanche, driven by α, and the generation of secondary electrons, driven by γ, reach a critical point where the gas transitions from

being an insulator to a conductor. This transition occurs when the criterion in (2.12) is met.

$$\gamma \cdot e^{(\alpha d)} = 1 \qquad (2.12)$$

where d is the distance between the electrodes, and e is the base of the natural logarithm, indicating an exponential increase in ionization events. This criterion represents the self-sustained nature of the discharge, where the gas no longer quenches the ionization process, leading to a complete breakdown [18].

2.3.2 The Streamer Mechanism

While the Townsend mechanism is dominant under low pressure and electrode separation, characterized by a pressure and distance product ($p \cdot d$) typically below 5 bar·mm, the streamer mechanism becomes more relevant under different conditions. Specifically, the streamer mechanism provides an explanation for electrical breakdown at a higher $p \cdot d$, typically over 5 bar·mm, where the configuration leads to different electrical discharge behaviors.

In this configuration, the streamer mechanism provides an explanation for electrical breakdown that differs from the Townsend mechanism. It begins with a single electron, which triggers an electron avalanche due to the influence of a strong electric field, similar to the Townsend mechanism. However, when this avalanche travels towards the anode, it generates a trail of positive ions. The front part of the avalanche accumulates space charges, which increase the local electric field, while the back part forms a plasma-like region with a balanced charge.

The transition from an avalanche to a streamer occurs when the enhanced electric field at the leading edge of the avalanche leads to increased ionization. This ionization process releases numerous photons, which ionize nearby neutral molecules in areas of high electric field. The resulting photoionization events initiate secondary avalanches that merge with the initial one, enlarging the plasma column and eventually spanning the gap between electrodes. The formation of this conductive plasma path is the fundamental step in establishing a streamer discharge.

Streamer discharges are characterized by their rapid development, with photon-induced ionization occurring more quickly than ionization due to electron impact. Typically, streamer breakdown occurs within a brief time frame, from 1 to 10 nanoseconds, compared to the longer duration associated with the Townsend mechanism, which can extend from several tens to hundreds of nanoseconds for gaps of 0.1 to 1 mm [19].

2.3.3 Pashcen's Law

Paschen's Law, which fundamentally relies on the Townsend mechanism (Section 2.3.1), provides an understanding of electrical breakdown in gases under varying pressure and electrode separation conditions. This law predicts the breakdown voltage (V_b) required to initiate a discharge between electrodes in a gaseous medium. In analytical form, Paschen's Law is expressed by (2.13) [13].

$$V_b = \frac{B \cdot pd}{\ln\left(\frac{A \cdot pd}{\ln(1+1/\gamma)}\right)} \tag{2.13}$$

where p is the pressure of the gas (bar), d is the distance between the electrodes (mm), and A, B, and γ are empirical constants specific to the gas and electrode materials. For air, and copper as electrode material, these values are $A = 1130\ 1/(mm \cdot bar)$, $B = 27.4\ kV/(mm \cdot bar)$, and $\gamma = 0.025$ [13].

This equation highlights how breakdown voltage varies with the product (pd), displaying a characteristic curve known as Paschen's curve, shown in Figure 2.8.
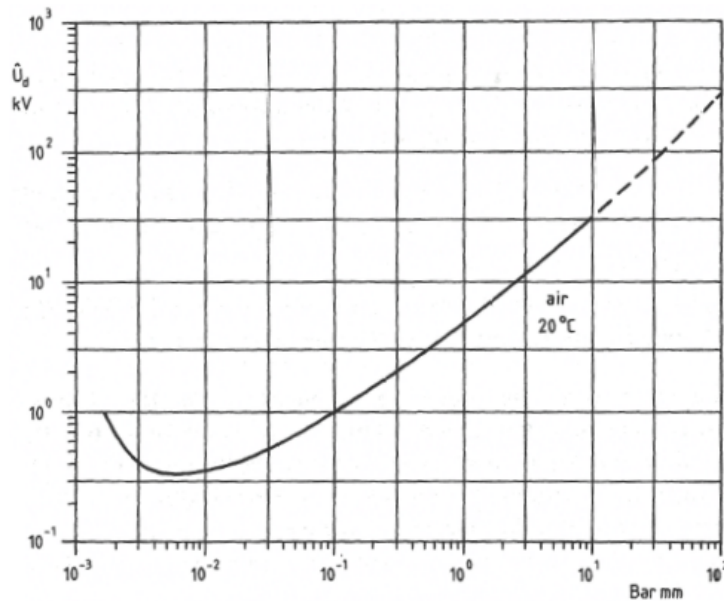
Figure 2.8: Paschen's curve for air, illustrating the relationship between pd and breakdown voltage [19].

The curve demonstrates that at a critical pd value, known as the Paschen minimum, the breakdown voltage reaches its lowest point, derived from Equation 2.13 to be approximately 350 V for air. Below this pd value, the breakdown voltage rises sharply, due to the lack of sufficient gas molecules to sustain the avalanche process needed for a discharge. At higher pd values, the breakdown voltage also increases, but the rise is more

gradual compared to the sharp increase observed at lower values. This is due to both the reduction in the electric field strength per unit length due to longer distances between the electrodes, and the decrease in the mean free path of electrons caused by higher gas pressures [13].

2.4 Partial Discharges

PD are localized electrical breakdowns occurring within the insulation system of HV equipment. These discharges may occur when the local electric field surpasses the local dielectric strength at or near an energized object [20]. Since these discharges only affect a part of the insulation, they do not lead to immediate breakdown. PD can occur across various types of insulation systems and under different electrical stress conditions. Although PD might not significantly impact short-term electric strength, they are particularly detrimental to the long-term integrity of organic insulating materials. Frequent and repetitive discharge impulses, especially at alternating current (AC) voltages and repetitive impulse voltages, lead to erosion of the insulation. This erosion typically results in a drastically reduced service life of the insulation material. Consequently, the occurrence and characteristics of PD serve as an essential criterion for assessing the quality of insulation [9] [13].

2.4.1 Methods for PD detection and measurements

Various methods have been developed and employed to identify and quantify PD. The main methods and their uses are:

- **Electrical measurement**
  Quantifies PD by directly measuring electrical parameters such as current and voltage, offering precise data on the intensity and nature of the discharges.

- **Ultra-high frequency (UHF) detection**
  Captures the high-frequency electromagnetic waves emitted by PD, offering insights into the characteristics and location of the discharges.

- **Acoustic detection**
  Utilizes sensitive microphones to detect the sound waves produced by PD, useful in pinpointing the location of discharges, especially in enclosed systems.

- **UV light camera**
  Uses UV cameras to visually detect PD by capturing the UV light emissions during discharge events, particularly effective in outdoor HV applications [20].

Among these methods, electrical measurement is the most common one and is the method that will be discussed further in this thesis.

2.4.2 Different Types of Discharges

PD can appear in various forms and types, primarily divided into two main categories based on their location within or around the insulation system:

- **External PD:** Occurs on the surface or around the insulation material.

  - **Corona discharges**
    Occur at high electric field concentrations, often at sharp edges or conductor points, leading to ionization of the surrounding air and potential insulation degradation.

  - **Surface discharges**
    Develops along the surfaces of exposed insulating materials, potentially leading to flashover, an increase in current due to air breakdown around the insulator.

- **Internal PD:** Occurs within the insulation material.

  - **Void discharges**
    Localized electrical breakdowns within cavities in the insulation, may lead to further degradation such as electrical treeing.

  - **Electrical treeing**
    Progressive degradation resulting from prolonged exposure to void discharges, leading to branching conductive paths through the insulation and eventual breakdown [16].

Each category and type of discharge presents unique features that impact the integrity of the electrical system. The different discharge types is illustrated in Figure 2.9 and 2.10

(a) Corona discharges

(b) Surface discharges
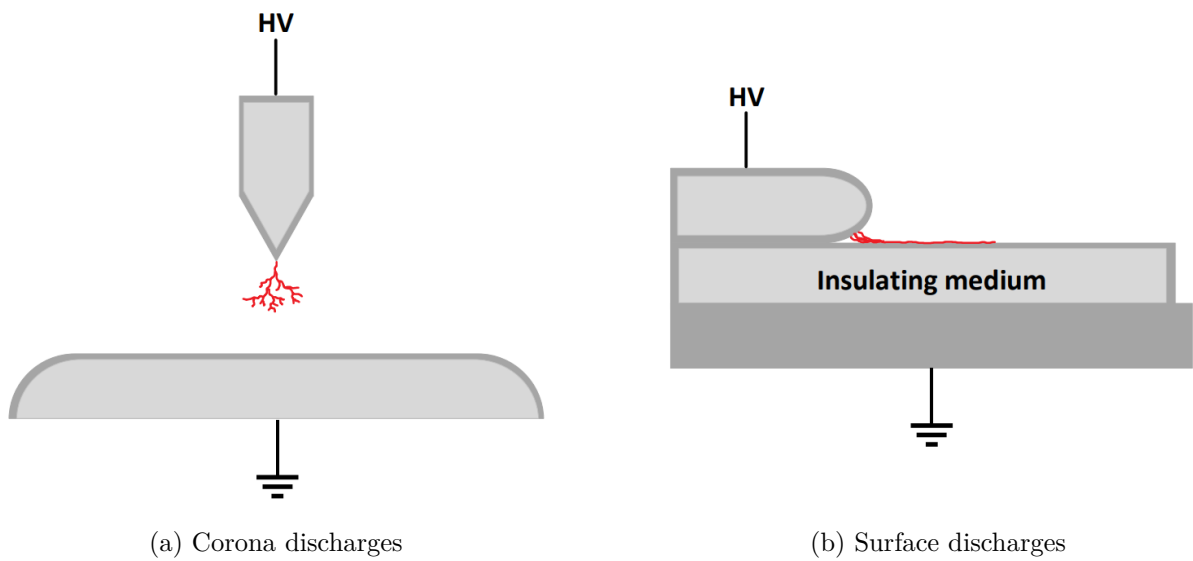
Figure 2.9: Illustrations of external PD types, based on [20].

(a) Void discharges

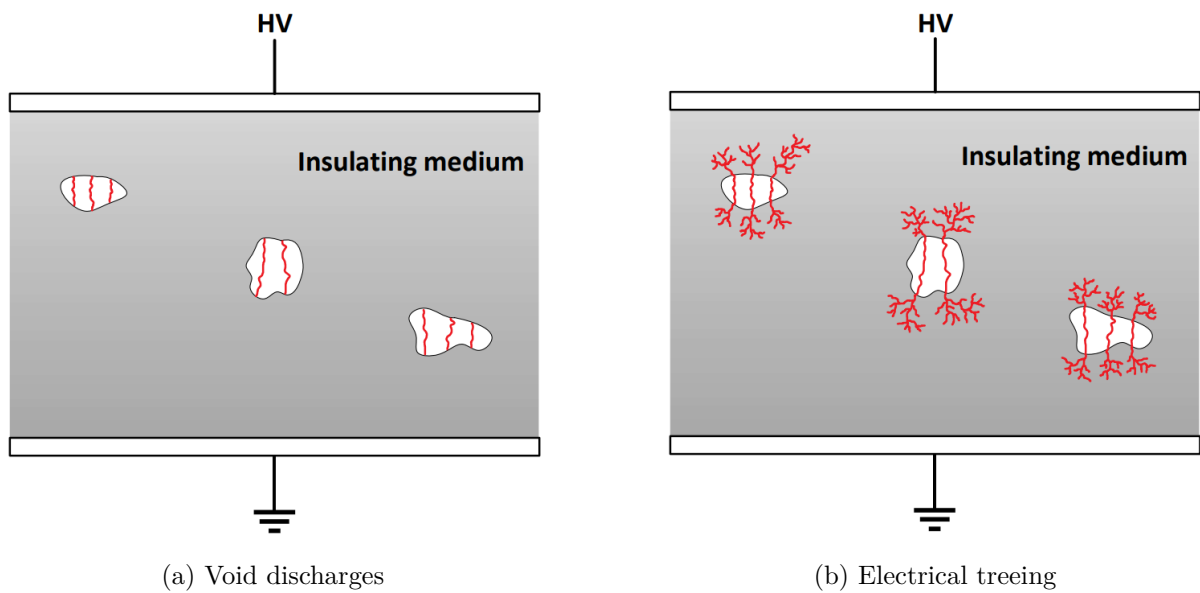(b) Electrical treeing

Figure 2.10: Illustrations of internal PD types, based on [20].

Corona discharges

Corona discharges are typically initiated at points where the electric field is intensified, such as at sharp metallic points or edges. These discharges are not exclusively associated with the HV electrode and can also be observed at the grounded side or even midway between two electrodes.

These discharges do not only indicate a physical phenomenon but also serve as a source of electrical noise, causing a challenge during PD testing. To reduce this, it's essential to ensure the testing environment is free of any elements that could induce corona, not just on the HV apparatus but also within the surrounding testing area [19].

Surface discharges

Surface discharges occur at the interface between gas and solid insulating materials within electrical systems. These are most evident in scenarios such as cable terminations where insulation is partially stripped, creating areas of dense inhomogeneous electric fields. This leads to increased electrical stress and possible initiation of discharges along the surface of the insulating material [13].

The critical point for surface discharges to initiate, where gas, insulator, and electrode meet is known as the triple-point. Figure 2.11 illustrates the triple-point, where discharges are prone to igniting due to the distorted field caused by surface irregularities, contaminants, or moisture. Once discharges occur, they tend to escalate and progress along the insulation's surface, eventually leading to flashover when reaching the opposite electrode.
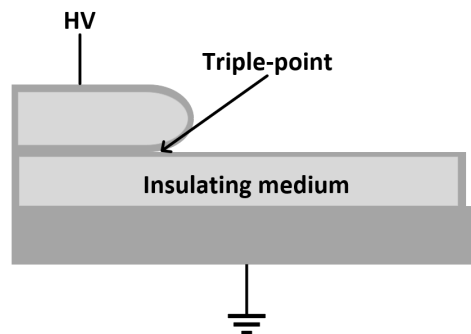
Figure 2.11: Insulating medium between two electrodes with the triple-point marked.

By managing the inhomogeneities at the triple-point, and ensuring that the insulating material is free from damage and contaminants, the possibility of surface discharges leading to flashover can be significantly reduced [13].

Internal PD

Internal PD occurs in defects of both solid and liquid insulation, often associated with gas-filled voids. Figure 2.12 illustrates a dielectric medium with such a void. Here, each part of the material is visualized as an individual capacitance, indicating the material's ability

32

to store electrical charge. The specific geometry of the insulating material influences the formation of these capacitances, which affects the distribution of electrical stress. As the applied voltage increases, the void may become the point of PD inception, due to enhanced field gradients caused by the difference in permittivities and the geometry of the void [16] [21].
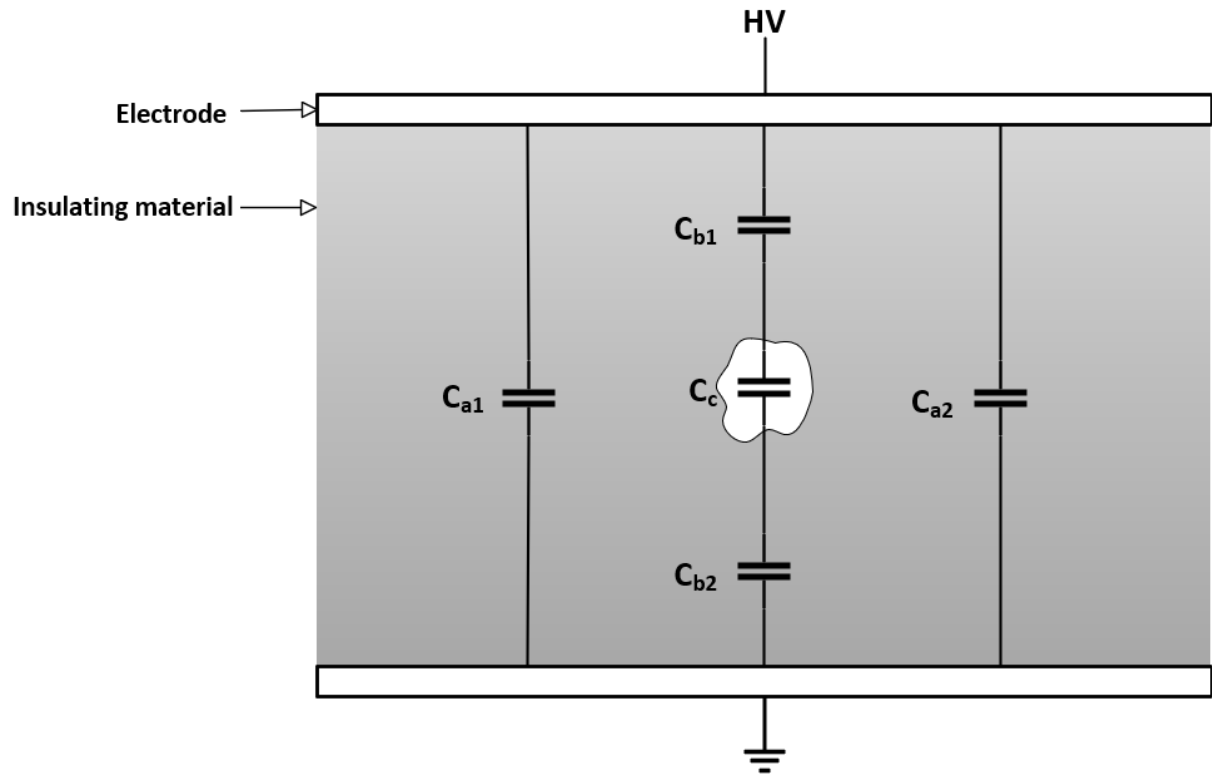
Figure 2.12: Dielectric medium with a gas-filled void, based on [16].

An equivalent circuit of the dielectric material containing a gas-filled void can be made, considering (2.14) and (2.15) for the capacitances.

$$C_a = C_{a1} + C_{a2} \tag{2.14}$$

$$C_b = \frac{C_{b1} \cdot C_{b2}}{C_{b1} + C_{b2}} \tag{2.15}$$

This circuit is shown in Figure 2.13, where C_a is the equivalent capacitance of the dielectric, C_b is the equivalent capacitance of the dielectric in contact with the void, and C_c is the capacitance of the void.
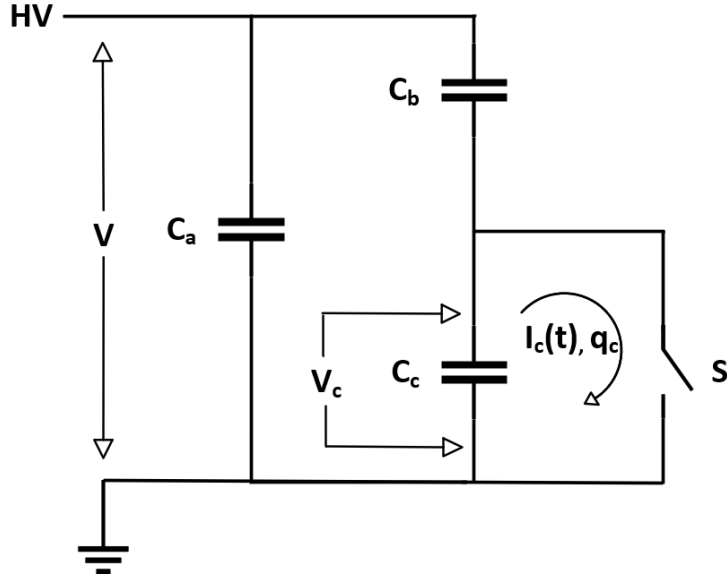
Figure 2.13: Equivalent circuit of a dielectric medium with a gas-filled void, based on [16].

Applying a voltage V over the electrodes, thereby charging the sample, the voltage V_c across the void rises, potentially leading to a discharge if it reaches the inception voltage, modeled by the closure of switch S. This discharge initiates a current $i_c(t)$, which then releases a charge q_c, defined by (2.16).

$$q_c = \Delta V_c C_c \tag{2.16}$$

where ΔV_c represents the voltage drop across the void due to the discharge and C_c is the capacitance of the void. However, in practical scenarios, C_b and C_c are usually unknown, making it impossible to directly measure the actual charge q_c. This leads to the PD detection circuit, used to measure a related quantity, the apparent charge Q_{ap}, by introducing a coupling capacitor. [16] [21] [22].

2.5 The PD detection circuit

The IEC 60270 standard outlines the technique for detecting and measuring PD through a dedicated test circuit, illustrated in Figure 2.14. In this circuit, the coupling capacitor (C_K) serves as a voltage supply to the test object during PD events, where Q_{ap} can be measured based on the discharge produced by C_K. The test object (C_T) represents the entire assembly of capacitors $(C_a, C_b, \text{ and } C_c \text{ in Figure 2.14})$ [21].
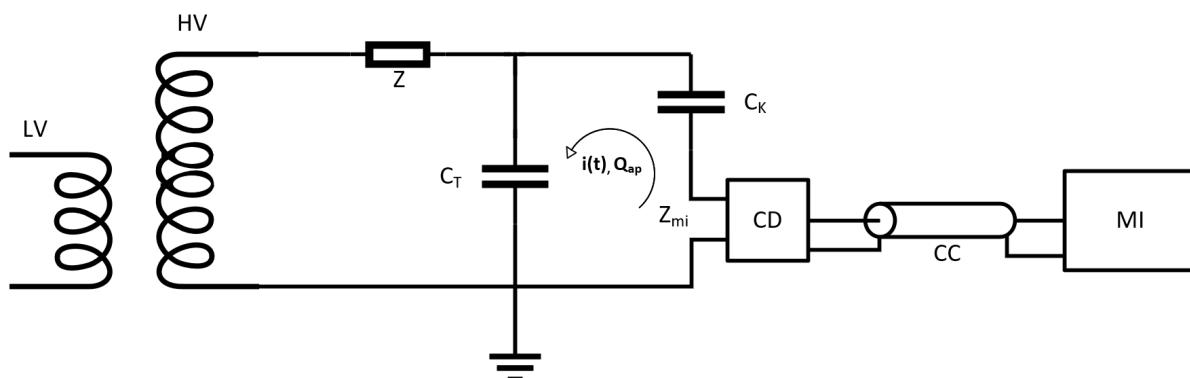
Figure 2.14: Schematic of the PD test circuit, based on [22].

When a PD event is initiated, the impulse current, $i(t)$, resulting from Q_{ap} flows through the measurement impedance (Z_{mi}) and the coupling device (**CD**) which converts the current into voltage signals ultimately registered by the measuring instrument (**MI**) via the transmission system (**CC**). The low- and high-voltage sides are represented by **LV** and **HV** respectively, while the optional impedance (**Z**) functions as a filter for reducing background noise from the HV source [21] [22] [23].

The sensitivity and accuracy of the PD measurements are significantly influenced by the ratio of capacitance between C_K and C_T. To maintain high measurement sensitivity without imposing excessive demand on the HV supply, C_K is typically chosen to have a minimum capacitance of 1 nF [23].

Calibration of the PD detection circuit

To accurately quantify Q_{ap}, the PD detection circuit needs to be calibrated. This process involves injecting a specific, short-duration charge pulse (q_0) into the terminals of the test object, as illustrated in Figure 2.15. This pulse is generated by a calibrator that combines voltage steps (U_0) with a capacitor (C_0), resulting in repetitive charges defined by (2.17) [21]. To ensure that the measurement system is quick and accurate enough to capture the PD events, IEC states that the rise time of the voltage steps should not exceed 60 ns [22].

$$q_0 = U_0 C_0 \tag{2.17}$$

Calibration establishes a reference scale, which is adjusted to account for the influence of the test object's capacitance on the measurement circuit. Since each test object can introduce unique variations due to different designs and materials, the calibration is specifically tailored for each new object to avoid inaccuracies in the readings. A new calibration is needed when the test object or circuit has been altered in any way.
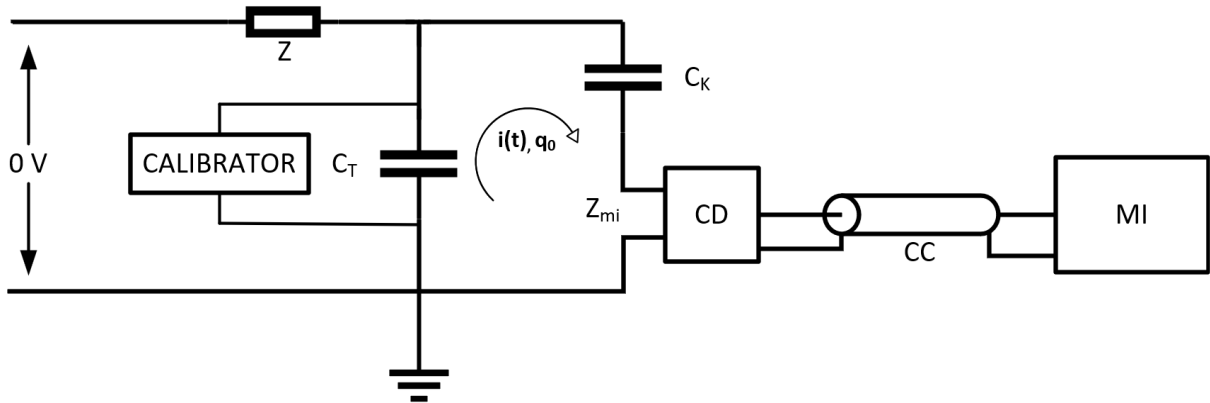
Figure 2.15: Schematic of the PD test circuit with a calibrator injecting charge q_0 to the terminals of the C_T, based on [22].

It is important to ensure that the circuit has no supplied voltage, as well as that the test object is de-energized during calibration, especially since the calibrator's capacitor (C_0) typically is a low-voltage component. Additionally, the choice of q_0 should be close to the expected Q_{ap} to enhance the accuracy of the PD magnitude measurement. This calibration approach ensures the detection circuit is finely tuned and capable of providing reliable, accurate measurements under varying test conditions [21] [22].

2.5.1 Noise and frequency range

During PD measurements, external noise is a factor that can impact the accuracy of PD measurements. To minimize the influence of this, selecting an appropriate frequency range for the measurements is necessary. The range should be somewhere noise is minimized, but PD is still measured accurately [21, pp. 599-614].

When considering frequency range, two separate PD measurement systems are specified: wide-band and narrow-band systems [21].

Wide-band systems feature a broad frequency range, extending from f_1 to f_2, that allows for capturing various pulse shapes and sizes of PD over a wide range. The frequency specifications for wide-band systems, as set by the IEC, are:

$$30 \text{ kHz} \leq f_1 \leq 100 \text{ kHz}$$
$$f_2 \leq 1 \text{ MHz}$$
$$100 \text{ kHz} \leq \Delta f \leq 400 \text{ kHz}$$

where Δf is the frequency bandwidth. However, the increased measurement sensitivity in a wide-band system also raises the likelihood of detecting pulses that do not originate from actual PD events, potentially leading to false readings [9] [22].

In contrast, narrow-band systems utilize a smaller bandwidth, which is advantageous for filtering out unwanted frequencies and reducing noise, thereby providing a clearer signal in environments with significant noise interference. The frequency specifications for narrow-band systems, as established by the IEC, are:

$$9 \text{ kHz} \leq \Delta f \leq 30 \text{ kHz}$$
$$50 \text{ kHz} \leq f_m \leq 1 \text{ MHz}$$

where f_m is the midband frequency [21] [22].

2.5.2 The Partial Discharge Inception Voltage (PDIV)

Linking the discharge magnitude of PD to the durability of electrical insulation systems has proven impossible. Consequently, modern PD testing primarily relies on go/no-go criteria based on the measured Q_{ap}, ensuring that no discharges with a magnitude over a set threshold occur under operational voltages [24].

Despite the established testing criteria based on the magnitude of Q_{ap}, identifying the precise voltage at which PD begins is essential for accurately assessing the operational thresholds of insulation systems. This voltage level is specified by the Partial Discharge Inception Voltage (PDIV), defined by IEC 60270 as "*the applied voltage at which repetitive partial discharges are first observed in the test object when the voltage applied to the object is gradually increased from a lower value at which no partial discharges are observed*" [22].

Determining the PDIV is important since it helps in assessing the reliability and longevity of insulation systems. A higher PDIV indicates better insulation quality, reducing the risk of insulation failure due to PD, and extending the system's operational life [25].

Imperfections such as irregularities, contaminants, and voids can significantly lower the PDIV. In addition, variables such as the physical condition of the insulation material, temperature, and pressure can further influence the PDIV. Pressure influences PDIV by altering the air's breakdown voltage, as explained by Paschen's Law in Section 2.3.3. Therefore, the PDIV can be identified as the lowest voltage at which the air gap's voltage meets the air's breakdown voltage [25]. To establish the PDIV of a test object, the initial step involves applying a voltage below the anticipated PDIV, and incrementally increasing it until discharges that meet or surpass a set discharge magnitude are detected [22].
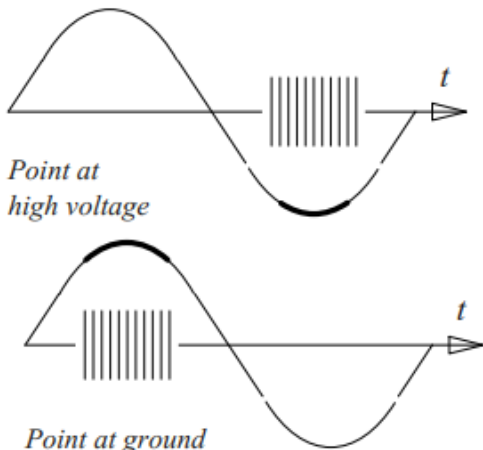
2.5.3 Analyzing PD activities

Different types of PD display distinctive patterns influenced by their characteristic phase angles and magnitudes, which can indicate the type of discharge present [13]. To effectively analyze PD activities, two main methods are used: Phase Resolved Partial Discharge (PRPD) analysis and Pulse Sequence Analysis (PSA). This thesis focuses on the PRPD method due to its detailed characterization of discharge patterns [26].

The PRPD method involves analyzing PD events based on their phase and magnitude within a voltage cycle. It utilizes a plotting mechanism where the phase angle of the applied voltage, covering a complete cycle of 360° (1 period), is represented on the x-axis, and the detected PD charge magnitude is plotted on the y-axis. Consequently, the PRPD pattern, which emerges by mapping these PD events to specific phase angles of the applied voltage cycle and correlating them with their respective charge magnitudes, provides a visual representation of the PD activity over several voltage cycles [26]. However, the PRPD pattern is extremely dependent on the voltage shape of the supply voltage, meaning that a supply voltage distorted by harmonics could produce inaccurate PRPD patterns [13].
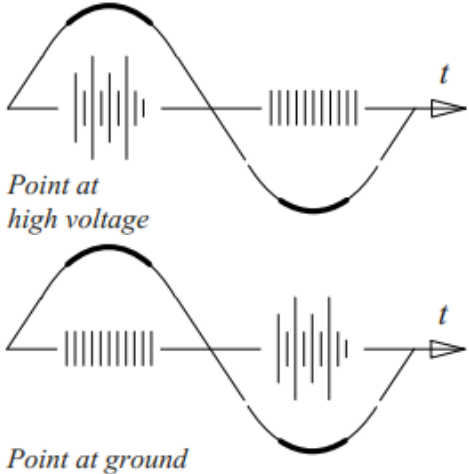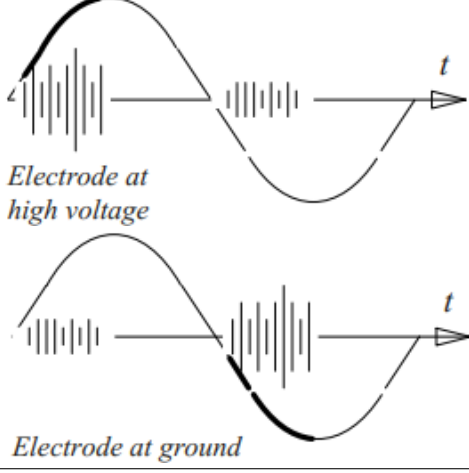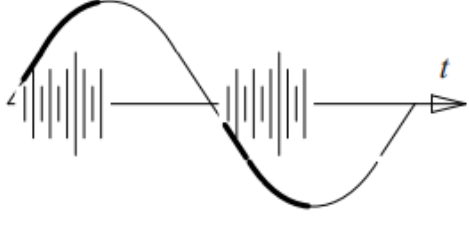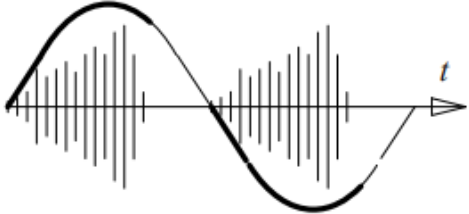
The typical PRPD patterns and a description of the types of PD that generate these are detailed in Table 2.5.3.

Table 2.1: Typical PRPD patterns for different types of discharges [13].

Type of discharge	Description	PRPD pattern
Corona discharge: Point-plane configuration in gas.	Impulses maintain a consistent amplitude, with their frequency rising as the voltage increases. At higher voltages, these discharges also occur in the opposite half-cycle.	*Point at high voltage* / *Point at ground*
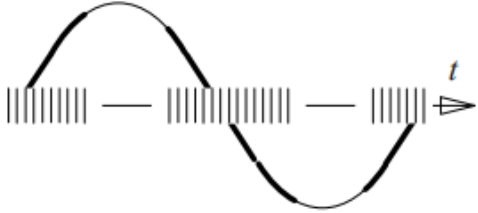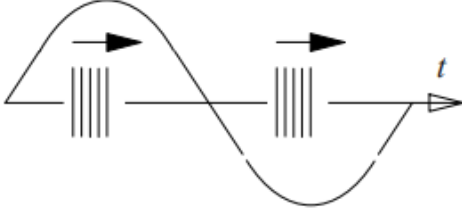
Table 2.1: Typical PRPD patterns for different types of discharges [13]. (Continued)

Corona discharge: Point-plane configuration in oil.	Represented by smaller, constant impulses that consistently hold their amplitude as the voltage increases, leading to a higher frequency of events.	*Point at high voltage* *Point at ground*
Surface or cavity discharge with direct electrode contact.	This type of discharge shows significant variations in amplitude across each half-cycle, changing by a minimum factor of 3.	*Electrode at high voltage* *Electrode at ground*
Surface or cavity discharge between insulators, with no direct electrode contact.	These discharges show less variability in amplitude across each half-cycle, changing by a maximum factor of 3.	
Surface or creepage discharge.	The magnitude of these discharges typically increases from the zero crossing to the peak.	

Table 2.1: Typical PRPD patterns for different types of discharges [13]. (Continued)

Contact noise.	These discharges occur primarily between loosely connected conductors near the zero voltage crossing. This noise continues throughout the entire cycle and stops once the conductors are securely connected.	
Discharges from electrodes on floating potential.	These discharges are shown as discharges with constant amplitude at regular intervals. The discharge frequency increases with the increase of voltage.	

2.6 3D scanning

3D scanning technology has become a large part of modern engineering fields for product development, manufacturing, and quality control. This technology transforms physical objects into accurate three-dimensional models by utilizing advanced software and hardware. The 3D scanners operate by collecting surface data from physical objects to recreate their shapes in digital form [27].

2.6.1 Types of 3D scanners

There is a variety of 3D scanners currently available, where the different types are suited for different needs and precision levels. Simple structures can be scanned using modern smartphones with LiDAR (Light Detection And Ranging) sensors, creating basic 3D models. However, this type of scanning does not meet the standards required for industrial applications, where metrology-grade 3D scanners are superior [27].

The three most common types of 3D laser scanners for industrial applications are:

- **Time of flight (TOF) laser scanners**
  These scanners function by emitting a laser pulse towards an object and calculating the distance based on the time it takes for the pulse to bounce back. This technology allows for accurate 3D data collecting over distances typically ranging from 5 to 300 meters, with precision levels between 4 to 10 mm, making it useful for long-range measurements [2]. The precision of these scanners is limited by the difficulty in accurately timing the return of laser pulses, due to the high speed of light. Additionally, scanning moving objects at high resolutions is especially challenging with TOF scanners. These scans require capturing multiple sample points over an extended period, where slight movements or vibrations can significantly distort the data [28].

- **Phase shift laser scanners**
  These scanners utilize alternating laser frequencies to measure distances by evaluating the phase difference between emitted and reflected light signals. They are optimized for shorter distances, usually within 1 to 50 meters, but can extend up to 120 meters. Because of their rapid data capture rates, some models can achieve up to a million points per second, offering better accuracy and resolution compared to TOF scanners [2]. However, these scanners are more susceptive to noise than TOF scanners [28].

- **Triangulation laser scanners**
  These types of laser scanners use a method where laser light is projected onto an object and the reflected light is captured by an image sensor within the scanner. This then forms a triangle between the laser source, the sensor, and the point on the object where the laser hits, as illustrated in Figure 2.16. By knowing the distance and angle between the laser source and the sensor, the scanner calculates the distance to the object using trigonometry. This results in precise measurements of the angle of returned light and therefore the distance from the scanner to the object's surface. These scanners are designed for shorter ranges, typically less than 5 meters. They are especially proficient at capturing details of small objects, making them ideal for high-resolution scans of smaller items [2]. Like all scanners, triangulation scanners are susceptible to inaccuracies when scanning shiny, reflective, or transparent materials due to distortions caused by reflections [28].
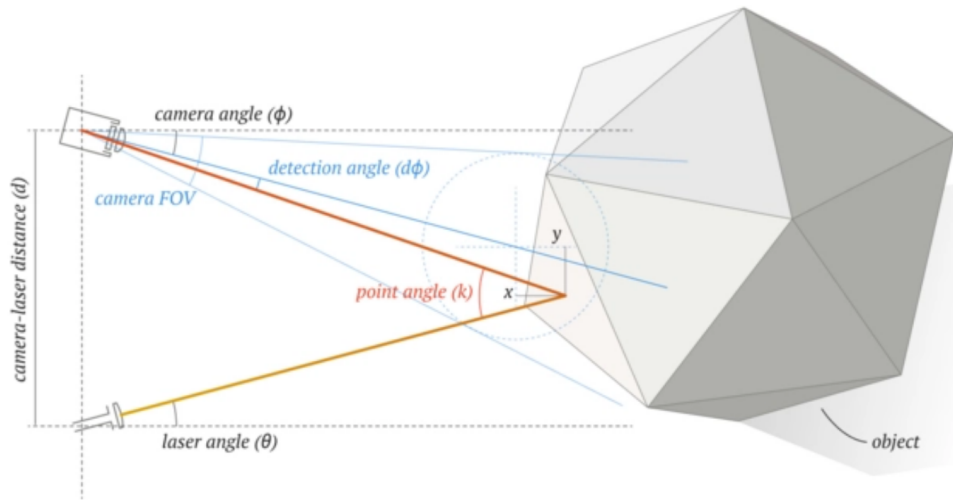
Figure 2.16: The principle of triangulation 3D scanning illustrated [2].

2.6.2 Markers

Markers in 3D scanning serve as reference points that significantly enhance the precision and reliability of combining multiple scans into a 3D model. They provide stable points recognized by the scanner, which is necessary in environments with limited scanner visibility or dynamic conditions.

Markers are classified into two main types: coded and non-coded. Coded markers offer superior precision and ensure clear tracking by preventing confusion with other markers. Non-coded markers, circular and available in various sizes, are typically arranged in triangular groups to help effectively align data points across scans. The varying sizes are used for different scanning distances and scenarios, enhancing their versatility.

The use of markers not only reduces errors and simplifies post-processing but also improves the quality of the resulting 3D model and accelerates the scanning process [29].

3 Test object

This chapter presents the test object and setup used in this study. It begins with a description of the test object, detailing its specifications. Following this, the components of the test setup are outlined. The methodology for introducing defects in the form of cuts to the cable end is then explained. Finally, the implications of the defects' location and other factors on the subsequent PDIV measurements are discussed.

3.1 The HV cable

The test object utilized in the study was an HVAC cable manufactured by Nexans, specifically designed for submarine installation, rated for voltages up to 300 kV. This cable featured an 1800 mm^2 copper conductor, surrounded by XLPE insulation. The cable's construction included CB doped XLPE as both the inner and outer semiconductive layers. A swellable tape was positioned directly above the outer semiconductive layer, designed to expand upon contact with water, thereby sealing off the cable's interior from moisture ingress.

Further protection was provided by a lead sheath, which not only shields the internal components from physical and chemical damage but also prevents moisture ingress. Over this, a PE outer sheath served as the final protective layer of the object. The cable was tested prior to the application of its additional armoring for subsea installation.

Figure 3.1 illustrates the layered construction of the cable, and Table 3.1 presents the technical specifications, including test voltages specified in IEC 62067 [30].
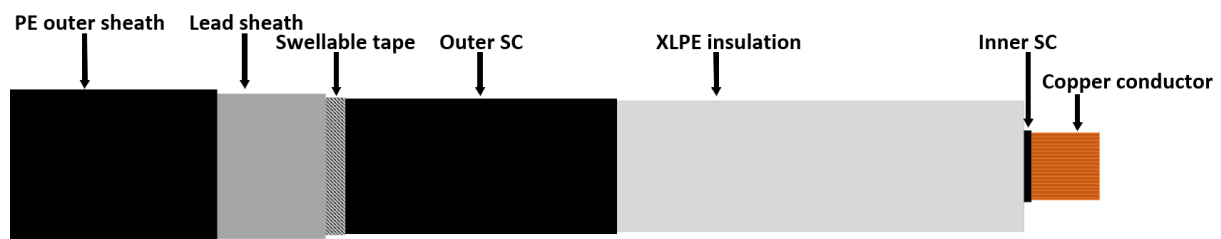
Figure 3.1: Illustration of the layered structure of the test object (not to scale).

Table 3.1: Technical specifications of the test object.

Component	Description
Conductor material	Copper
Conductor cross-section	1800 mm²
Maximum operational voltage	300 kV
Insulation material	XLPE
Additional protection	Swellable tape, lead sheath, PE outer sheath
Specified voltages from IEC 62067 [30]	
Rated highest voltage (U_m):	300 kV
Value of U_0 for determination of test voltages:	160 kV
Pre-stress voltage for PD measurements ($1.75 \cdot U_0$):	280 kV
PD measurement voltage ($1.5 \cdot U_0$):	240 kV

3.2 Test setup

In the test configuration of the cable, one end was connected to a gas-insulated termination, which was to be connected to an HVAC source. The opposite end was jointed to an insulating plastic utilizing a PMJ, effectively simulating a real-world jointing scenario. This setup is illustrated in Figure 3.2.
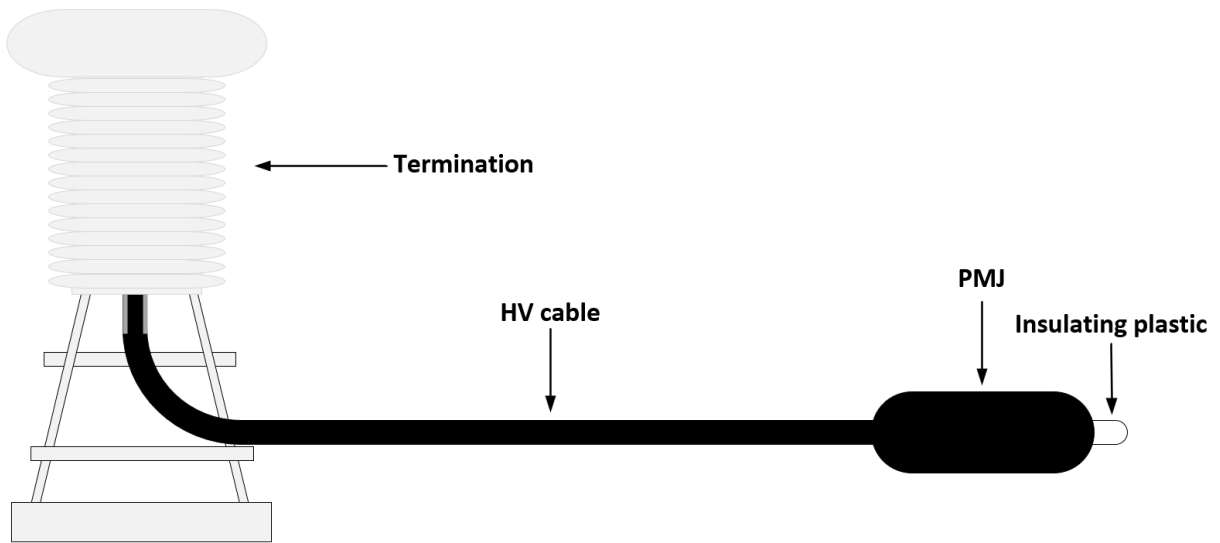
Figure 3.2: The test setup, illustrating the HV cable configuration with one end terminated and the other end jointed to an insulating plastic using a PMJ (not to scale).

The jointed end was the primary focus of the test setup, where later damage to the cable's XLPE insulation was inflicted and subsequently tested for measuring the PDIV. A detailed illustration of this connection within the PMJ is provided in Figure 3.3.
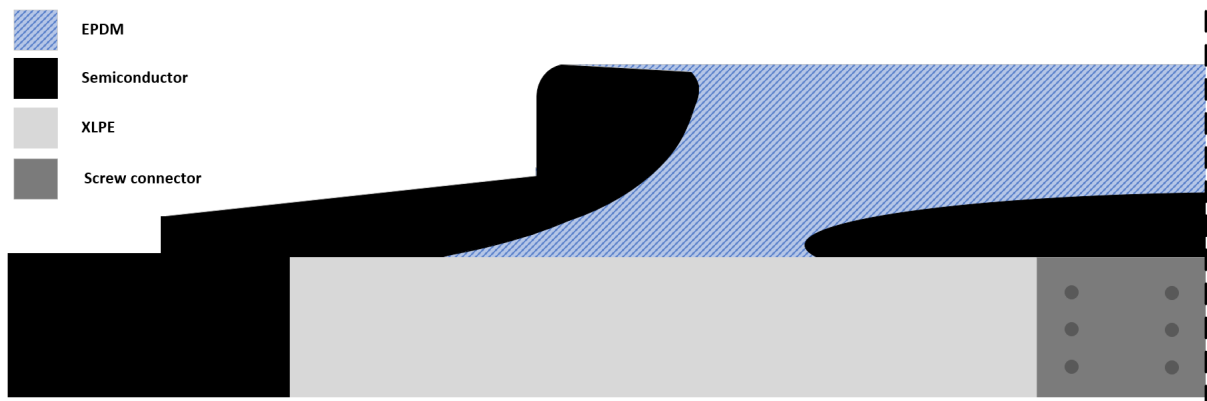
Figure 3.3: Detailed view of the cable end connected via a screw connector to an insulating plastic (not shown) within a PMJ (not to scale).

3.3 Damage implementation on XLPE insulation

To introduce defects in the form of cuts on the XLPE insulation surface of the cable end, a specialized template was designed. This design allowed for control over both the depth and length of the cuts. The schematics of the template are shown in Figure 3.4.
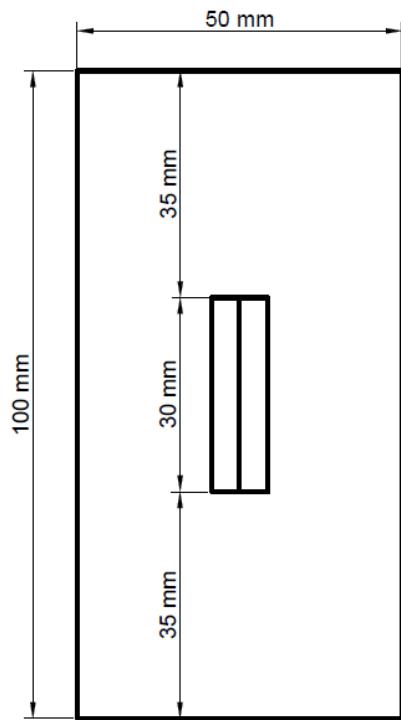
(a) Top view of the template's schematic.
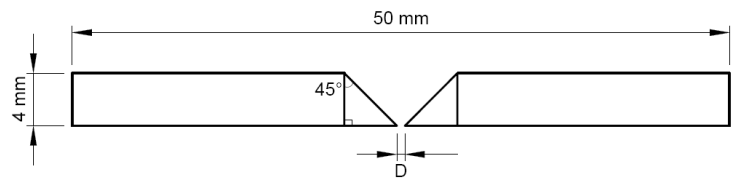
(b) Detailed schematic of template's center, where "D" marks the variable distance for different cut depths.

Figure 3.4: Schematics for the template used for implementing cuts to the XLPE insulation.

Sørlie Verktøyindustri AS, a local tool manufacturer in Halden, was commissioned to produce the template and a custom knife specific to the template. Five templates were fabricated, enabling cuts at depths of 1.0 mm, 1.2 mm, 1.4 mm, 1.6 mm, and 1.8 mm. The manufactured templates and the custom knife are shown in Figure 3.5.

Figure 3.5: The manufactured templates with the custom knife for implementing cuts to the XLPE insulation.

The cable end was prepared for jointing by removing the outer layers, thus exposing the XLPE insulation surface. The template and insulation surface were thoroughly cleaned with isopropanol before the template was positioned on the insulation surface, where it was secured by straps to prevent movement during the cutting process. The cuts were then implemented, starting with a depth of 1 mm, and deepened incrementally for each subsequent test after 3D scanning and PDIV measurements.

The motivation for reusing the same cable end for each cut depth was to maintain consistency, save time in preparing new cable ends for each experiment, and minimize variables that could influence the results.

The prepared cable end, with the exposed insulation and a cut in the insulation surface, is illustrated in Figure 3.6.
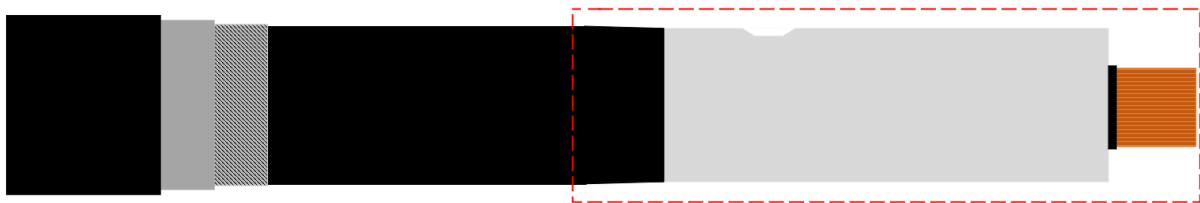
Figure 3.6: Illustration of the prepared cable end with a cut in its insulation (not to scale).

The marked area in Figure 3.6, zoomed in to show the cut area with distances and depths, is presented in Figure 3.7. Here, "y" marks the distance from the semiconductor cutback, which is where the exposed insulation transitions to the cable's semiconductor, to the

47

cut, and "x" marks the intended cut depths of 1.0 mm, 1.2 mm, 1.4 mm, 1.6 mm, and 1.8 mm.
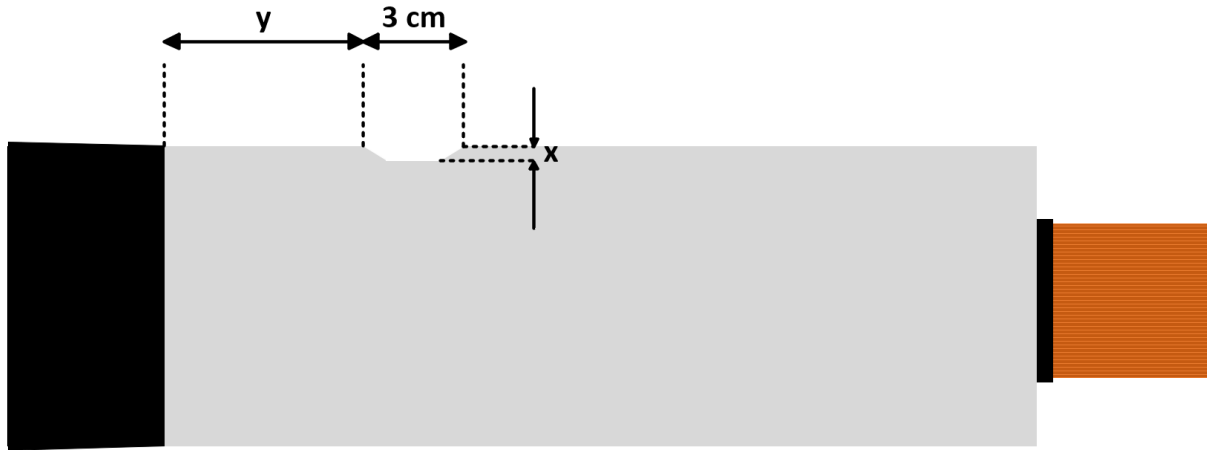
Figure 3.7: Zoomed in view of the cut region on the cable end. "y" marks the distance from the semiconductor cutback to the cut, and "x" marks the intended cut depths (not to scale).

3.4 Location of the cuts, the installation of the PMJ, and their implications

Ideally, the cuts would be located closer to the semiconductor cutback of the cable end. This placement would ensure that the cuts ended up directly beneath the PMJ's semiconductor. However, due to the size of the templates used, the cuts were positioned further out on the insulation surface, necessary to ensure that the template remained perfectly aligned with the insulation surface, keeping the depths along the cut length consistent and unaffected by any surface irregularities. Consequently, the cuts were positioned under the insulating EPDM material of the PMJ, close to the semiconductor, as visualized in Figure 3.8.
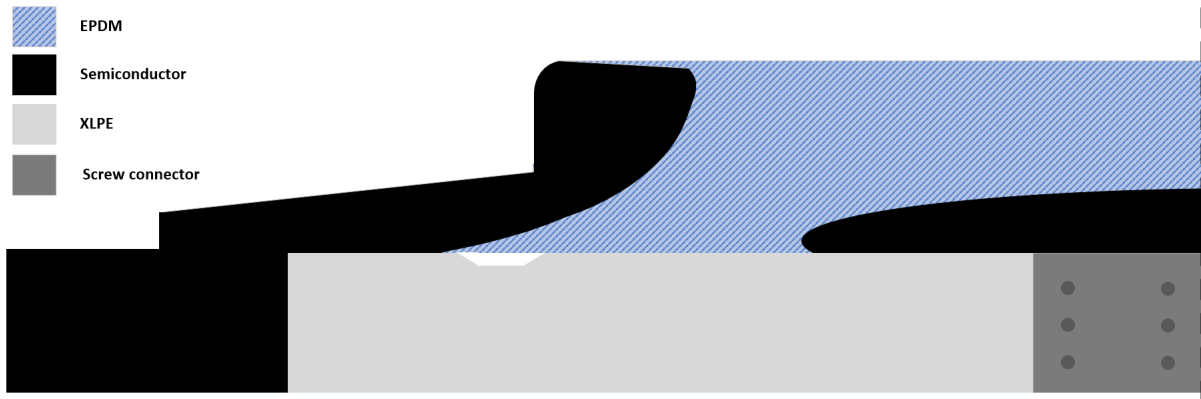
Figure 3.8: Visualization of the cable end connected via a screw connector to an insulating plastic (not shown) within a PMJ, showing the cut positioned beneath the PMJ's EPDM insulation (not to scale).

Although the PMJ was consistently placed at the same distance during each installation, the exact position of the cuts relative to the PMJ's semiconductor could vary due to the PMJ's slight contraction post-installation. The installation process required the use of silicone oil as a lubricant to protect the internal components of the PMJ while sliding it over the joint. Before finalizing the installation, the PMJ was moved back and forth over the exposed insulation and cut region, where the surface was thoroughly cleaned with isopropanol to ensure that the cuts remained oil-free in the final assembly. The reason for keeping the cuts oil-free was due to the later calculations on PDIV in air-filled voids, in addition to that oil-filled cuts would require a much higher PDIV, potentially exceeding the safe operating voltage of the test equipment.

After the PMJ installation, self-amalgamating tape was applied to further compress the PMJ over both the screw connector and the cut region. This step was intended to eliminate any unnecessary air pockets that could lead to destructive PD during the subsequent PDIV measurements. However, this manual process introduced uncertainties about the pressure in the voids created by the cuts, which could not be consistently replicated due to the variability in tape application.

The implications of these variations are further analyzed through simulations, presented in Chapter 6.

3.5 Discussion

The use of silicone oil during the PMJ installation process, while necessary for lubrication, introduced an uncertainty of potential oil residue that could influence the resulting PDIV, despite the thorough cleaning procedure. Since the PMJ were installed to the cable end

multiple times, with different cut depths for PDIV measurements, maintaining consistent experimental conditions was needed for reliable results. Exploring alternative installation techniques or lubricants with minimal dielectric strength could enhance the reliability of the later PDIV measurements.

The cuts implemented on the cable end were more rift-like than precise, resulting in irregular and uneven surfaces that potentially influence the initiation of PD. Using alternative methods and tools to make these cuts could further standardize the test conditions, leading to more consistent and reliable PDIV measurements.

The manual application of self-amalgamating tape, which was repeated for each installation of the PMJ, further supports the need for more standardized procedures. Inconsistencies in tape application could lead to uncontrolled void pressures, potentially resulting in variable PDIV results. Establishing a more standardized method for the application of this tape would improve the reproducibility of the test setup.

4 3D scanning

This chapter outlines the 3D scanning process used to create precise models of the intentionally introduced defects at the HV cable end. It begins with an introduction to the scanning device, detailing its specifications and functionality. The procedure for scanning is then described, followed by a presentation of the mesh results generated from the cuts at various depths. Finally, the chapter discusses the post-processing methods used to analyze the scans further.

4.1 Scan device

The 3D scanner utilized in this thesis was the HandySCAN BLACK™|Elite laser scanner, produced and manufactured by CREAFORM. This portable, high-precision 3D scanning device is designed for industrial design, engineering, and quality control applications. It is specifically used for capturing the detailed geometry of physical objects to create accurate 3D models. A picture of the scanner is shown in Figure 4.1.

Figure 4.1: The HandySCAN BLACK™|Elite handheld 3D scanner [31].

The HandySCAN BLACK™|Elite operates together with CREAFORM's VXelements software, which has powerful processing capabilities that enable the capturing and refinement of the resulting geometric data efficiently. Furthermore, the scanner employs a triangulation laser scanning method with 11 blue laser crosses, enabling a rapid measurement rate of up to 1,300,000 measurements per second. With an accuracy of up to 0.025 mm and a mesh resolution of 0.1 mm, it was particularly suited for creating detailed and precise scans of the cuts. [31].

4.2 Scanning procedure and resulting mesh

The test object was thoroughly cleaned using isopropanol to remove any contaminants that could potentially influence the accuracy of the scan. Subsequently, markers were strategically placed around the cut region, enabling the scanner to capture the cuts with optimal detail and precision.

The HandySCAN BLACK™|Elite was calibrated according to the manufacturer's specifications using the calibration plate specifically provided for this scanner. This calibration step was required to ensure the precision of the scanning process by aligning the scanner's settings with the known dimensions and features of the calibration plate.

To optimize the conditions for the scan, the ceiling lights were turned off. This measure was taken to minimize potential interference from external light sources, which could negatively influence the quality of the scan by introducing noise.

The test object was then meticulously scanned from multiple angles to capture all surface details. The scanner and the laptop connected, running the VXelements software, then generated a detailed 3D mesh representation of the object, capturing the topography of the cut region.

4.2.1 Noise mitigation

Due to the reflective properties of the test object's XLPE insulation, certain scans were negatively affected by excessive noise, resulting in visual distortions that could blur necessary details in the generated 3D mesh.

To address this issue, the scanner's shutter speed, a setting that influences the amount of light captured during the scanning process, was adjusted. Reducing the shutter speed decreased the scanner sensor's exposure to intense reflections, thereby reducing both brightness and resultant noise.

This adjustment was performed through a series of scans, with the shutter speed being adjusted incrementally, where each resulting mesh was analyzed for detail capture and

noise levels. This process enabled the identification of an optimal shutter speed that minimized noise without compromising the detail capture of the scans. Figure 4.2 illustrates the impact of these adjustments, where (a) displays a section of the mesh generated with the initial shutter speed, and (b) shows the mesh after the shutter speed adjustment, revealing significant improvements in quality and noise reduction.

(a) Area with excessive noise
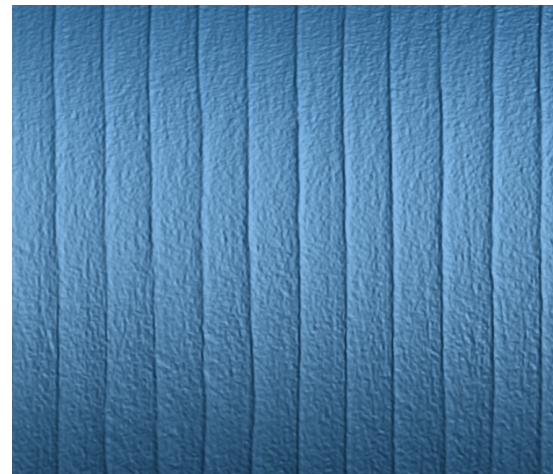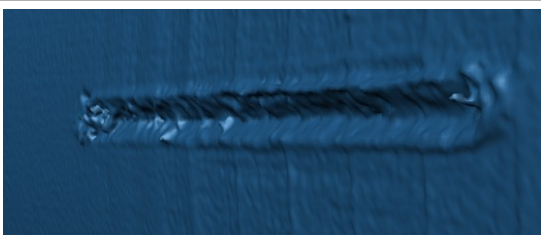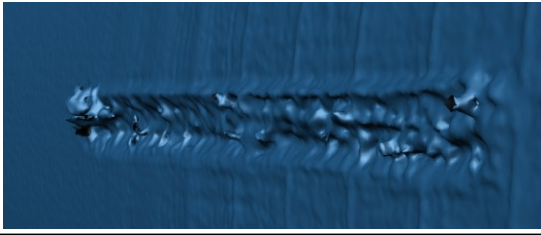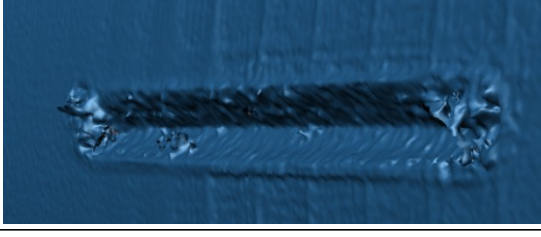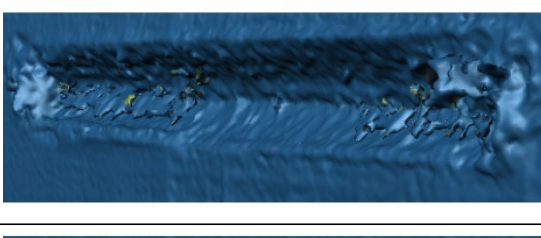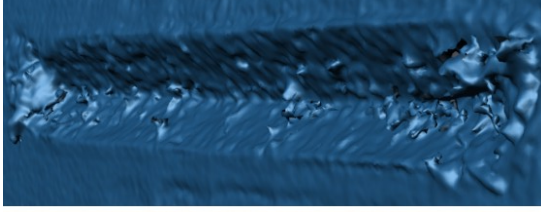
(b) Area with reduced noise

Figure 4.2: 3D scanned segment of the prepared cable end, comparing the mesh quality before (a) and after (b) the shutter speed adjustment.

4.2.2 Resulting 3D mesh of the cuts

The level of detail captured in the generated meshes from the scans displayed the scanner's ability to replicate the topography of the cuts. Table 4.1 presents the meshes for the five intended cut depths on the insulation surface of the cable end. Each image is zoomed in to focus on the area of the cut.

Table 4.1: Zoomed-in views of the mesh generated by the 3D scans, of the various cut depths.

Intended depth of cut	3D mesh from scan
1.0 mm	
1.2 mm	
1.4 mm	
1.6 mm	
1.8 mm	

4.3 Measurements of the scanned cut depths

To extract specific measurements from the mesh obtained through the 3D scans, the resulting data files were exported from VXelements as stereolithography (stl) files. These

files capture the surface geometry of the scanned cable ends, providing a detailed representation of their structure and the geometry of the cuts.
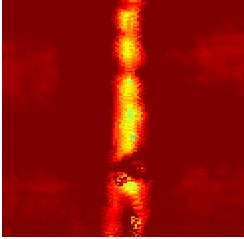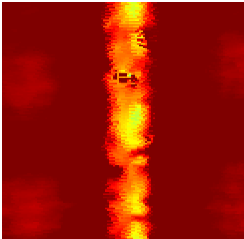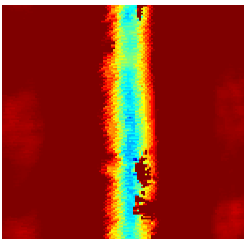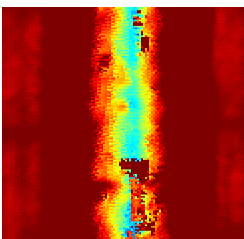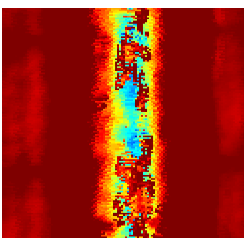
The .stl files were imported into Nexans' patented algorithm named Surfical (Surface Inspection and Control Algorithms), specifically developed to analyze laser scanning data of cylindrical cable ends. This advanced algorithm facilitates various operations such as loading, sectionalizing, computing, and displaying data, with a focus on detecting and analyzing areas of interest, particularly regions with defects [32].
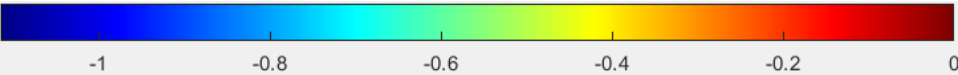
To accurately assess these defects made from the cuts, the algorithm was modified to extract the generated height maps from the specific areas surrounding the cuts. These maps provided a precise representation of surface topography at the cut locations, enabling accurate measurements of the cut depths. Afterward, a separate MATLAB script was developed to calculate the maximum depths of these cuts by analyzing the height variations within the maps. This script is to be found in Appendix A. The reason for finding the maximum depth was based on the assumption that this point would have the highest field concentration, due to both the sharp curvature at this point and being closest to the conductor, enhancing the electric field intensity and consequently resulting in the lowest PDIV.

4.3.1 Resulting cut depths

Table 4.2 presents the resulting height maps derived from the Surfical algorithm, alongside the intended cut depths for the five cuts and the maximum measured depths obtained from analyzing the height maps.

Table 4.2: Height maps and measured cut depths from 3D scans.

Intended cut depth	Height map	Maximum measured cut depth
1.0 mm		0.6525 mm
1.2 mm		0.5528 mm
1.4 mm		1.0712 mm
1.6 mm		1.0736 mm
1.8 mm		1.1152 mm

From this point on, the cut depths of 1.0 mm, 1.2 mm, 1.4 mm, 1.6 mm and 1.8 mm will be referred to as the intended cut depths, while the measured cut depths of 0.6525 mm, 0.5528 mm, 1.0712 mm, 1.0736 mm, and 1.1152 mm will be referred to as the intended cut depths.

4.4 Discussion

During the 3D scanning process, several challenges occurred that impacted the quality and accuracy of the scan data.

Initially, access to the Surfical algorithm, essential for processing and analyzing the scan data comprehensively, was delayed due to the need for a separate computer to run this confidential algorithm. As a result, most of the 3D scans were completed without being able to analyze the defects thoroughly. In an attempt to compensate for this limitation, there was conducted multiple scans of the various cut depths using different settings and shutter speeds, aiming to optimize the quality of the scans.

As illustrated in Table 4.1, each cut depth presented a unique geometry within the defects, highlighting inconsistencies in the method used to implement reproducible cuts of varying depths. The observed differences in the geometry of each cut indicate that the precision of the cutting tool may not be as good as anticipated. These differences could arise from the limitations of the tool itself or its interaction with the XLPE material.

One notable issue that emerged from the measured cut depths was that some cuts intended to be deeper were scanned and measured as shallower. This could be attributed to several factors, most likely the flings of XLPE within the cuts, which resulted from the tools used to make these cuts. These flings could have caused data points from the scanning to overlap, leading to a final mesh that inaccurately depicted the cuts as shallower than their actual depths.

Furthermore, the settings used in the VXelements scanning software played an important role in the quality of the resulting scans, particularly in terms of noise reduction. Adjustments made to the ambient lighting conditions around the scanning area also significantly reduced noise levels, enhancing the scan quality. Additionally, variations in the movement speed and angles of the scanner around the scanning area were found to contribute to noticeable differences in scan quality.

5 PDIV measurements

The PDIV measurements were carried out in an HV lab at Nexans in Halden, a laboratory frequently used for HV cable testing and PD analysis. The objective of these measurements was to examine the influence of various cut depths in the insulation of a cable on the PDIV.

This chapter outlines the laboratory setup for the PDIV measurements, describes the hardware and calibration process for PD detection, explains the experimental procedures for these measurements, and presents the results.

5.1 Laboratory setup

The laboratory setup consisted of an HVAC generator powered by a step-up transformer, to apply the needed voltage levels for measuring the PDIV of the test object. A voltage divider was used to ensure precise monitoring of these voltage levels, thereby protecting the test object from excessive voltage and securing the accuracy of the PDIV readings. Additionally, a coupling capacitor was utilized to transfer the PD signals to the measurement equipment, isolating them from the HV environment. The terminated end of the test object was connected to the coupling capacitor via a busbar. The laboratory setup and the arrangement of the components are visualized in Figure5.1.
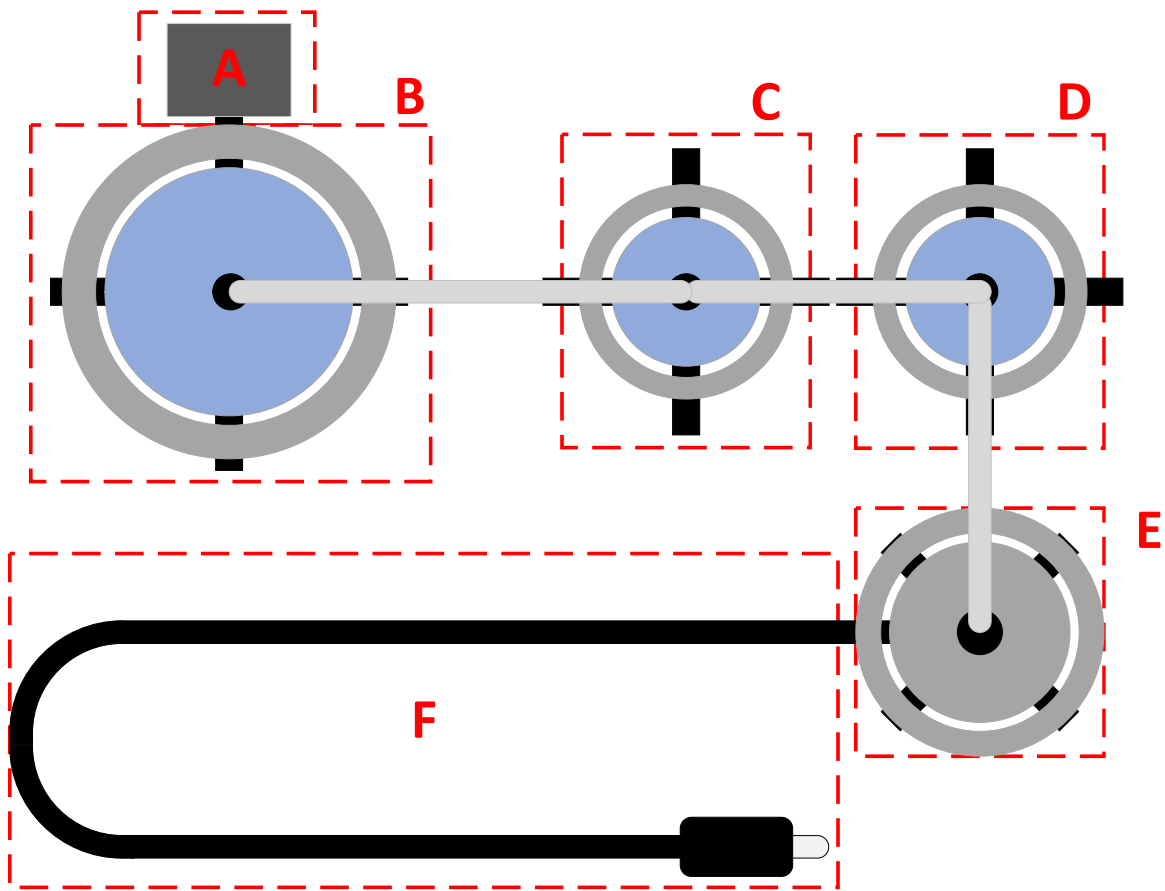
Figure 5.1: Laboratory setup, seen from above. A = Step-up transformer, B = HVAC generator, C = Voltage divider, D = Coupling capacitor, E = Termination, F = Test object. B, C, D, and E are connected with busbars.

5.1.1 Safety Measures

Due to the use of HV, strict safety protocols were established before applying voltage to the test object and the following PDIV measurements. The implemented safety measures included:

- **Safety interlock system**
  The laboratory was equipped with a comprehensive safety interlock system linked to the HVAC generator. This system incorporated sensors at all access points, including doors and ports leading to the test area. Protective barriers connected to the interlock system were set up to restrict access, and any breach in the interlock

system during testing would result in the immediate disconnection of the HVAC generator's power supply and its automatic grounding.

- **HV warning signs**
  Signs displaying "DANGER HIGH VOLTAGE" were placed around the testing area to alert individuals of the HV testing, further decreasing the risk of any breach to the interlock system.

- **Warning lights on fences**
  The protective barriers around the HV test were fitted with warning lights, indicating the status of the safety interlock system.

- **Post-test safety procedures**
  After testing, the HV source was required to be visibly turned off, and the automatic grounding of the generator through an earth rod had to be visually confirmed.

- **Manual grounding**
  When entering the test area post-test, all installation components of the test circuit were manually grounded using earthing sticks, connecting them to the same ground potential as that of the HVAC generator, ensuring a safe working environment.

5.2 PD detection hardware and setup

The detection of PD was performed using the Omicron MPD 800 universal PD measurement and analysis system. The MPD 800 system consisted of:

- **The MPD 800 acquisition unit**, which served as the PD measurement instrument, designed to capture and analyze PD signals in various HV applications accurately.

- **The RBP1 battery pack**, which provided an independent power source to the MPD 800 acquisition unit, enabled uninterrupted testing.

- **The CPL1 coupling device**, which connected the MPD 800 acquisition unit to the test circuit's coupling capacitor. This device is designed to handle higher reactive currents than the MPD 800 acquisition unit can alone.

- **The MCU2 control unit**, which was connected to the MPD 800 acquisition unit via fiber-optic cables, converting optical signals to electrical signals, which were transmitted to a PC via USB, where analysis was performed through the dedicated MPD Suite analysis software [33].

The components of the OMICRON MPD 800 system are visually presented in Figure 5.2, while Figure 5.3 illustrates how the system was connected to the test setup.
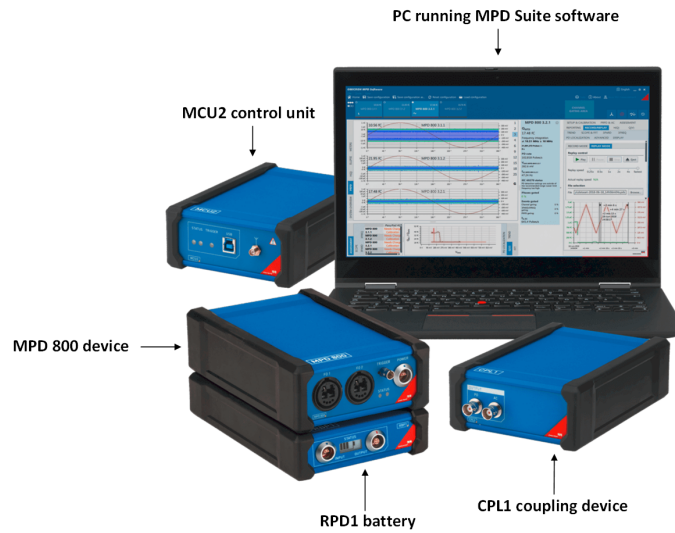
Figure 5.2: The components of the MPD 800 universal PD measurement and analysis system [34].
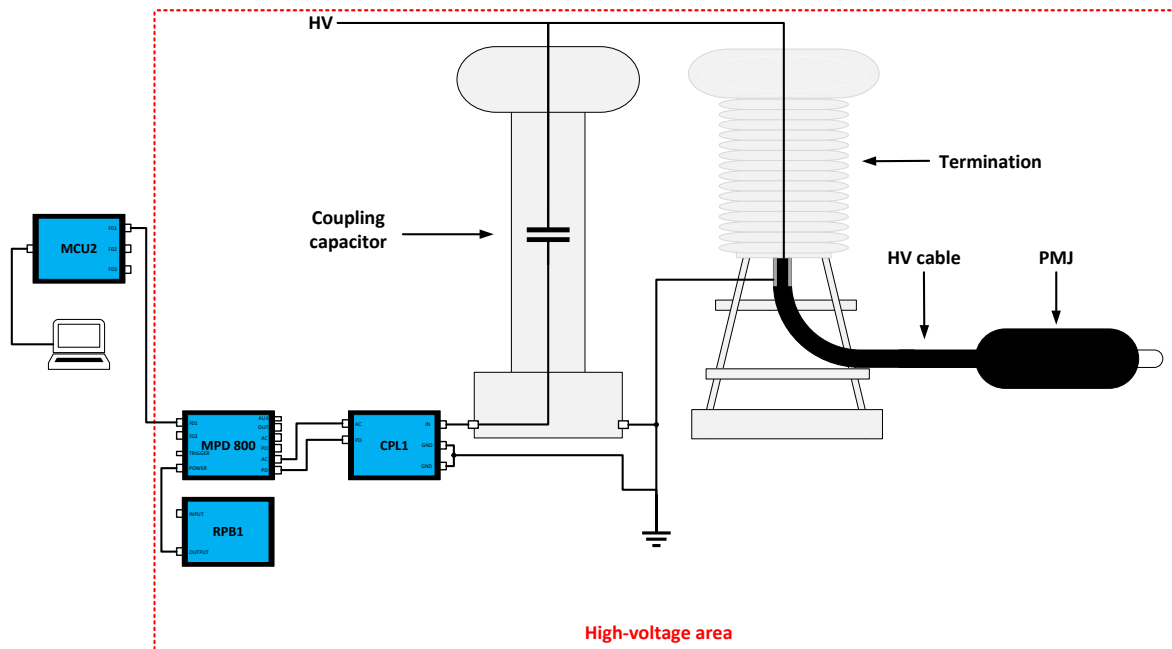
Figure 5.3: Connection of the MPD 800 system to the test setup, based on [33].

5.2.1 Calibration

The calibration of the PD measurement system was conducted using the OMICRON CAL 542 charge calibrator, which was capable of emitting charges at specified amplitudes: ± 100 pC, ± 50 pC, ± 20 pC, ± 10 pC, and ± 5 pC. This allowed for precise adjustment of the calibration charge based on the test conditions. The calibration unit is pictured in Figure 5.4.
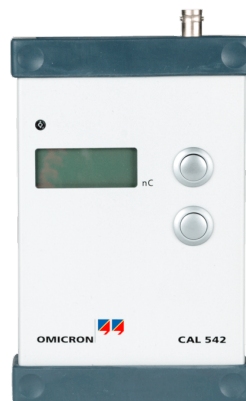
Figure 5.4: The OMNICRON CAL 542 charge calibrator [35]

The calibrator was connected to the terminals of the test object, specifically the termination and the lead sheath of the HV cable, which served as the ground. This setup is illustrated in Figure 5.5.
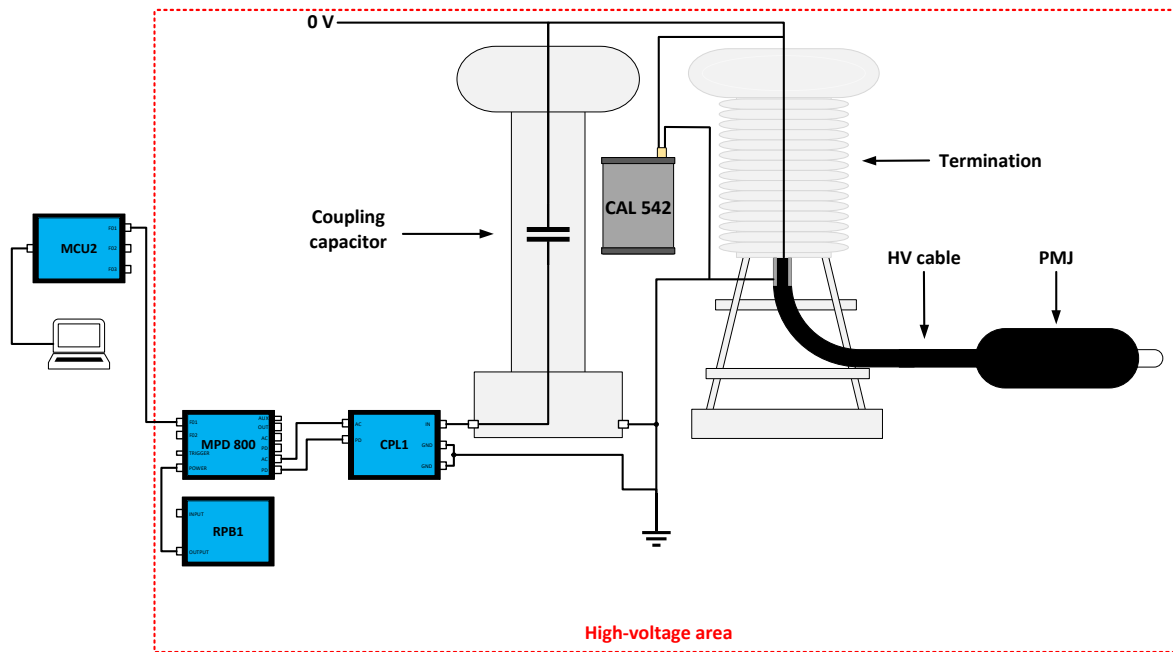
Figure 5.5: Connection of the OMICRON CAL 542 charge calibrator to the test setup

Before each PDIV measurement, the system was calibrated using a 5 pC charge, selected based on the anticipated apparent charge values to be measured during the tests, in accordance with IEC 60270 [22]. The calibration charges were measured using the MPD 800 system, with the MPD Suite software visualizing the pulses through a PRPD plot, as shown in Figure 5.6. The system was then calibrated based on the scale factor calculated by the MPD 800 system, ensuring accurate and reliable PD measurements.
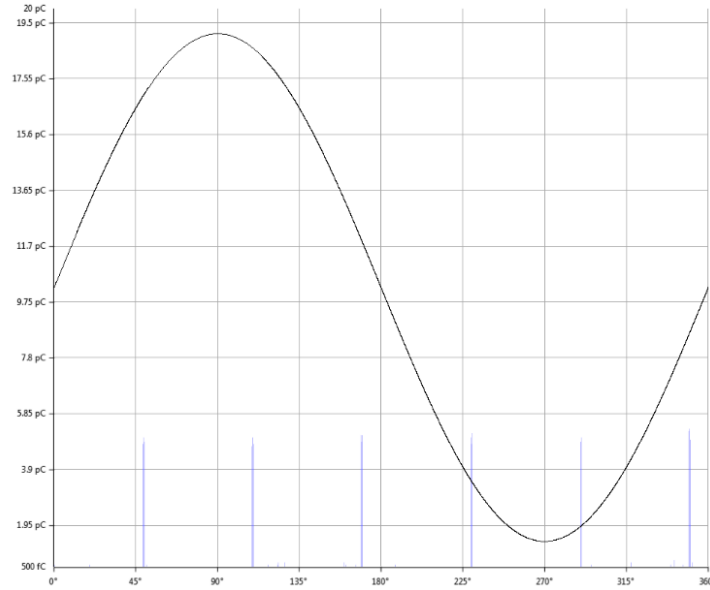
Figure 5.6: Visualization of the 5 pC calibration charge in a PRPD plot.

5.2.2 Frequency and bandwidth

The frequency range used for detecting PD was narrow-band, to specifically measure the PD pulses from the test object and minimize noise interference. The selected midband frequency and bandwidth utilized for all tests are presented in Table 5.1.

Table 5.1: Midband frequency and bandwidth used for PD detection

f_m	170.58 kHz
Δf	30 kHz

These parameters were chosen according to the specifications outlined in IEC 60270 [22]. The specific midband frequency of 170.58 kHz and bandwidth of 30 kHz were selected based on previous PD measurements performed in the laboratory, which demonstrated minimal external noise interference at these settings.

5.3 Procedure

Firstly, the OMICRON MPD 800 system was connected to the test setup as visualized in Figure 5.3. A laptop equipped with the OMICRON MPD Suite software was set up

64

outside the test area, next to the voltage regulation controls of the HVAC generator. The grounding connection of the test circuit was then removed, and the necessary safety measures, including the interlock system, were established to prevent unauthorized access to the test area during the testing. Thereafter, the output voltage of the HVAC generator was gradually increased by steps of 10 kV. Each step was maintained for 30 seconds to allow for stabilization and recording of the PRPD plots. The steps continued until initial changes were observed in the PRPD plot, indicating the beginning of PD activity. At this time, the voltage steps were reduced to 5 kV to enhance the sensitivity of the testing procedure as the test object approached the PDIV. Upon reaching the PDIV, where noticeable PD was detected, the PRPD plot was recorded for an additional 30 seconds to capture the discharge patterns. Following this, the output voltage of the HVAC generator was decreased to zero, and the test circuit was re-grounded.

5.4 Results

The resulting PDIV for the different cut depths is presented in Table 5.2, and visualized in in a bar chart in Figure 5.7.

Table 5.2: Measured PDIV for the various cut depths.

Cut depth		PDIV
Intended	Measured	
1.0 mm	0.6526 mm	85 kV
1.2 mm	0.5528 mm	100 kV
1.4 mm	1.0712 mm	230 kV
1.6 mm	1.0736 mm	95 kV
1.8 mm	1.1152 mm	85 kV
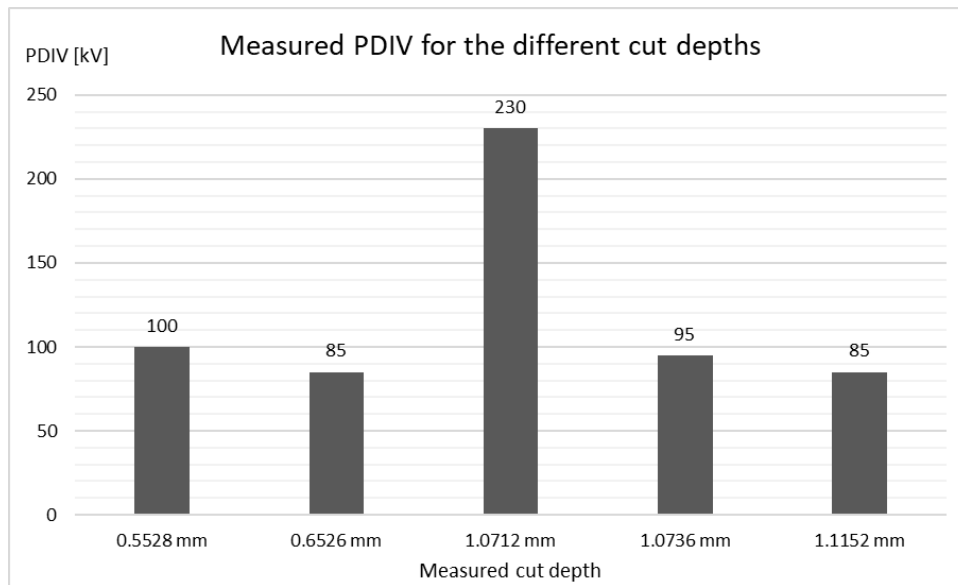
Figure 5.7: Visual representation of the measured PDIV for the different cut depths.

As seen in Figure 5.7, the resulting PDIV does not show a linear relationship between the cut depths and PDIV. Additionally, the high PDIV of 230 kV for the cut depth of 1.0712 mm differs substantially from the other depths.

The resulting PRPD plot for when the PDIV was reached for the cut depth of 0.6526 mm is presented in Figure 5.8. As one can see from the pattern, it corresponds to a surface or cavity discharge between insulators, with no direct electrode contact based on Table 2.5.3. All measurements for the various cut depths showed the same PRPD patterns and can be found in Appendix B.
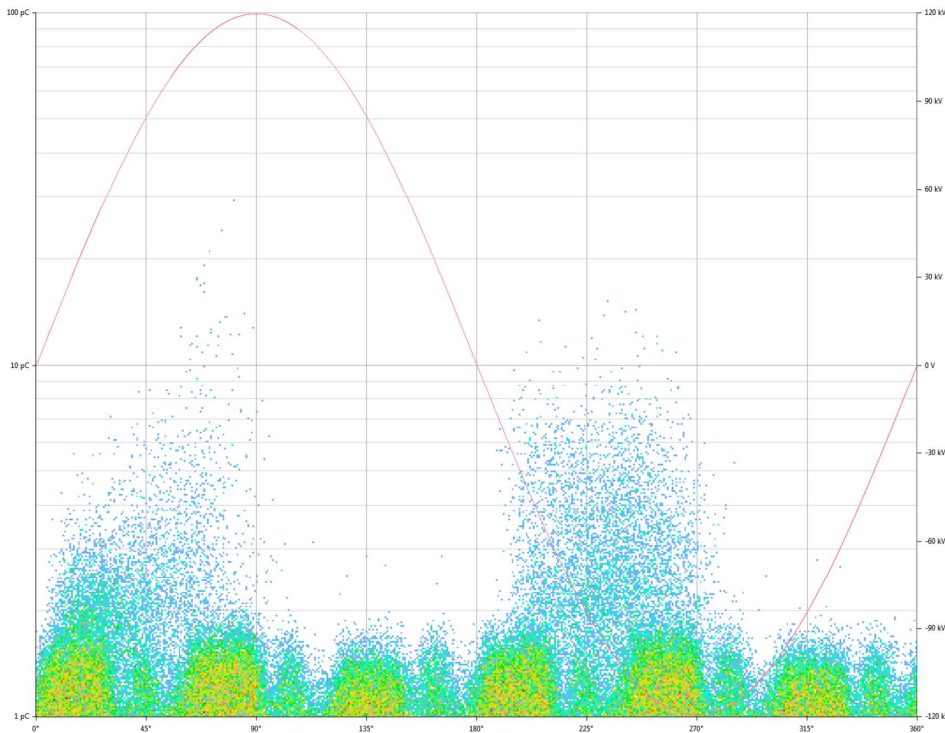
Figure 5.8: PRPD plot of the cable end with a cut depth of 0.6525 mm at its PDIV of 85 kV.

5.5 Discussion

Before the cable end presented in this thesis, the experiments were conducted on another cable end. At the first attempt at measuring PDIV on this sample, it suffered a flashover due to a mismatch in diameter between the screw connector and the XLPE insulation, creating an air gap that initiated surface discharges. This setback demonstrated how minor errors in the test setup could have severe consequences.

During the PDIV measurements, various challenges influenced the reliability of the results. One of these issues was the considerable amount of background noise from nearby machinery and vehicular traffic at times, occasionally hindering the ability to detect PD. To ensure a clear detection, the measurements were therefore postponed to times when the noise levels were lower.

The measurement procedure itself involved maintaining voltage steps for only 30 seconds. Extending this duration might have allowed for the initiation of PD at lower voltages, or potentially revealed a stabilization where discharges ceased to occur. This could potentially result in a more accurate representation of PDIV. In addition, the setup was further compromised by the HVAC generator's difficulty in maintaining stable voltage levels at

67

the stepwise voltage increase. The generator frequently fluctuated by several kV, which could have prematurely triggered PD at voltages higher than the PDIV presented.

Furthermore, pre-stressing was deliberately excluded from the PDIV measurement procedure due to the heightened risk of PD activity at these voltage levels, potentially leading to breakdown. Although conditioning of the test object through pre-stressing is a common procedure for PD measurements, it is not required by IEC for the determination of PDIV [22].

The nonlinear relationship between cut depths and measured PDIV, as shown in Figure 5.7, indicated an inconsistency in the test setup. This was most likely caused by either oil residue in the cuts, or a varying void pressure, as discussed in Section 3.5.

6 Simulations and calculations

This chapter examines the simulation and analytical evaluation of electric field distributions in voids created by cuts on the insulation surface of an HV cable end. The simulations and calculations aim to replicate and analyze conditions similar to those potentially present in the physical test setup, as discussed in Chapter 3. These conditions are represented through various simulated scenarios using COMSOL Multiphysics® to estimate the electric field distribution and intensity, which are used for the subsequent calculation of FEF and estimation of PDIV.

6.1 Simulation model

To simulate the electric field distribution and calculate the FEF in response to various depths of cuts in the insulation of an HV cable, a 3D model was developed in COMSOL Multiphysics®. This model utilized FEM for electrostatic calculations, employing Gauss' Law for the electric displacement field (6.1) and the relationship between electric field and potential (2.2) to solve the modified Poisson's equation for linear dielectrics (6.2) [36].

$$\nabla \cdot \vec{D} = \rho \tag{6.1}$$

$$-\nabla \cdot (\varepsilon_0 \varepsilon_r \nabla V) = \rho \tag{6.2}$$

The model consisted of a cylindrical conductor, a dielectric insulation layer, and an outer shield with ground potential, representing a simplified yet representative segment of the HV cable's end. The geometric parameters of the model were the same as the physical dimension of the HV cable described in Chapter 3. The primary objective of these simulations was to evaluate the impact of insulation surface defects, represented as cuts of different depths, on the local electric field intensity. These defects were introduced into the model as "ideal" cuts, and do not match the exact geometries of the actual defects 3D scanned in Chapter 4. However, they accurately replicate their depth and the angle at which they penetrate the insulation.

To optimize computational efficiency, the model was bisected, focusing on the segment containing the defect. This significantly reduced computational demands without influencing the accuracy of the electric field simulations. The final 3D model is shown in Figure 6.1, and a more detailed 2D view of the cut region can be seen in Figure 6.2, highlighting the specific modifications to the insulation geometry.

(a) Isometric view

(b) Front view
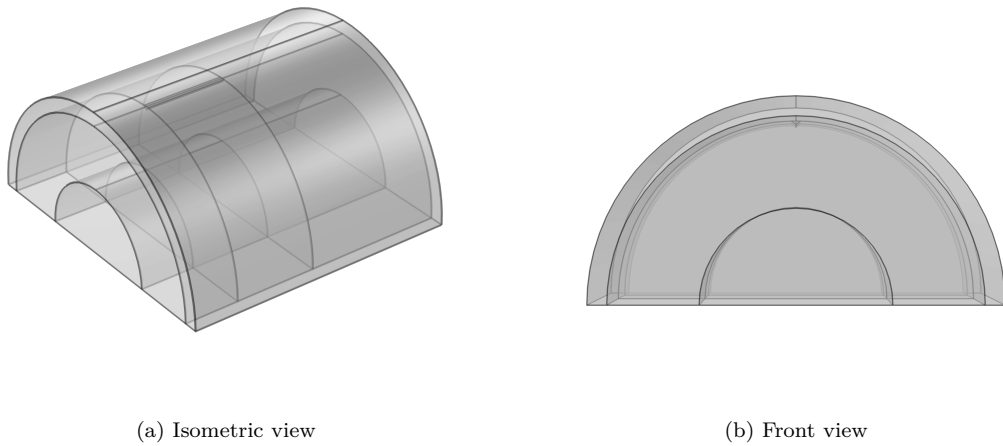
Figure 6.1: Views of the 3D simulation model, constructed in COMSOL.

(a) 2D view of the simulation model, visualizing the cut region

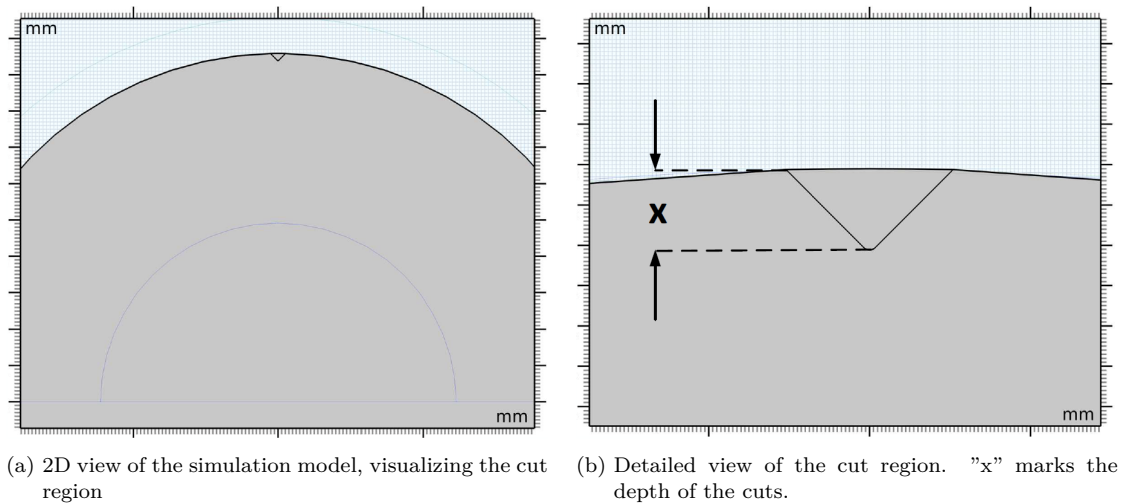(b) Detailed view of the cut region. "x" marks the depth of the cuts.

Figure 6.2: Views of the cut region in the simulation model. Dimensional specifics are not shown due to confidentiality.

6.2 Simulation scenarios

A series of simulations was conducted to assess the electric field distribution under various conditions. These scenarios were chosen to replicate possible conditions of the HV cable end as discussed in Chapter 3, to evaluate both the impact of different materials in contact with the cuts on the surface of the HV cable's insulation and the possibility of oil-residue filling the voids. The permittivity of the materials used in the simulation is presented in Table 6.1, and the scenarios include:

- **Air-filled void in contact with semiconductor**:
  This scenario simulates a void caused by a cut in the insulation's surface, filled with air ($\varepsilon_r = 1$), and in contact with a semiconductor, modeled as a perfect electric conductor ($\varepsilon_r = \infty$).

- **Air-filled void in contact with EPDM**:
  Here, the void is filled with air, and the outer material is modeled as EPDM, an insulating material used in the body of a PMJ (see Section 2.1.2), with a permittivity of 2.73. This simulation investigates the insulating layers' influence on the field enhancement caused by the void, reflecting the installation condition where a cut is positioned beneath the PMJ's EPDM insulation rather than directly under the semiconductor.

- **Oil-filled void in contact with semiconductor**:
  This scenario explores a void filled with silicone oil ($\varepsilon = 2.7$) against a layer modeled as a perfect electric conductor. It represents the condition where residual oil might fill the void during the PMJ installation, influencing the dielectric characteristics and the overall electric field distribution.

- **Oil-filled void in contact with EPDM**:
  Similar to the previous scenario, but with the void in contact with insulating EPDM material, this scenario examines the effects of a smaller permittivity contrast between the void and the surrounding insulation on the electric field distribution.

For each scenario, two sets of simulations were conducted to examine both the intended and the measured cut depths encountered in the experiments:

1. **Intended cut depths simulation**: Used the intended cut depths of 1.0mm, 1.2mm, 1.4mm, 1.6mm, and 1.8mm to investigate a controlled range of defect sizes.

2. **Measured cut depths simulations**: Utilized actual measured cut depths obtained from 3D scans in Chapter 4 to reflect the conditions present in the PDIV measurements in Chapter 5, and their effects on field distribution.

Table 6.1: Relative permittivity (ε_r) for materials used in simulations.

Material		Permittivity (ε_r)
Air	=	1
XLPE	=	2.5
Silicon oil	=	2.7
EPDM	=	2.72
Conductor	=	∞
Semiconductor	=	∞

6.3 Electric field simulations

This section presents the electric field simulations conducted under the four various scenarios, separated into intended and measured cut depths. These simulations were performed to clarify how different materials and defect sizes influence the electric field within an HV cable's insulation.

6.3.1 Visualization of electric field lines and intensity

To visually represent the influence of both the scenarios and cut depths on electric field behavior, 2D plots from the simulations were made. These present the electric field intensity at the cut region for the intended cut depths of 1.0 mm and 1.8 mm under the different scenarios, shown in Table 6.2.

Table 6.2: 2D plots visualizing the electric field intensity (kV/mm) for cuts under different scenarios.

Scenario	1.0 mm	1.8 mm
Air-filled void in contact with semiconductor		
Air-filled void in contact with EPDM		
Oil-filled void in contact with semiconductor		
Oil-filled void in contact with EPDM		

73
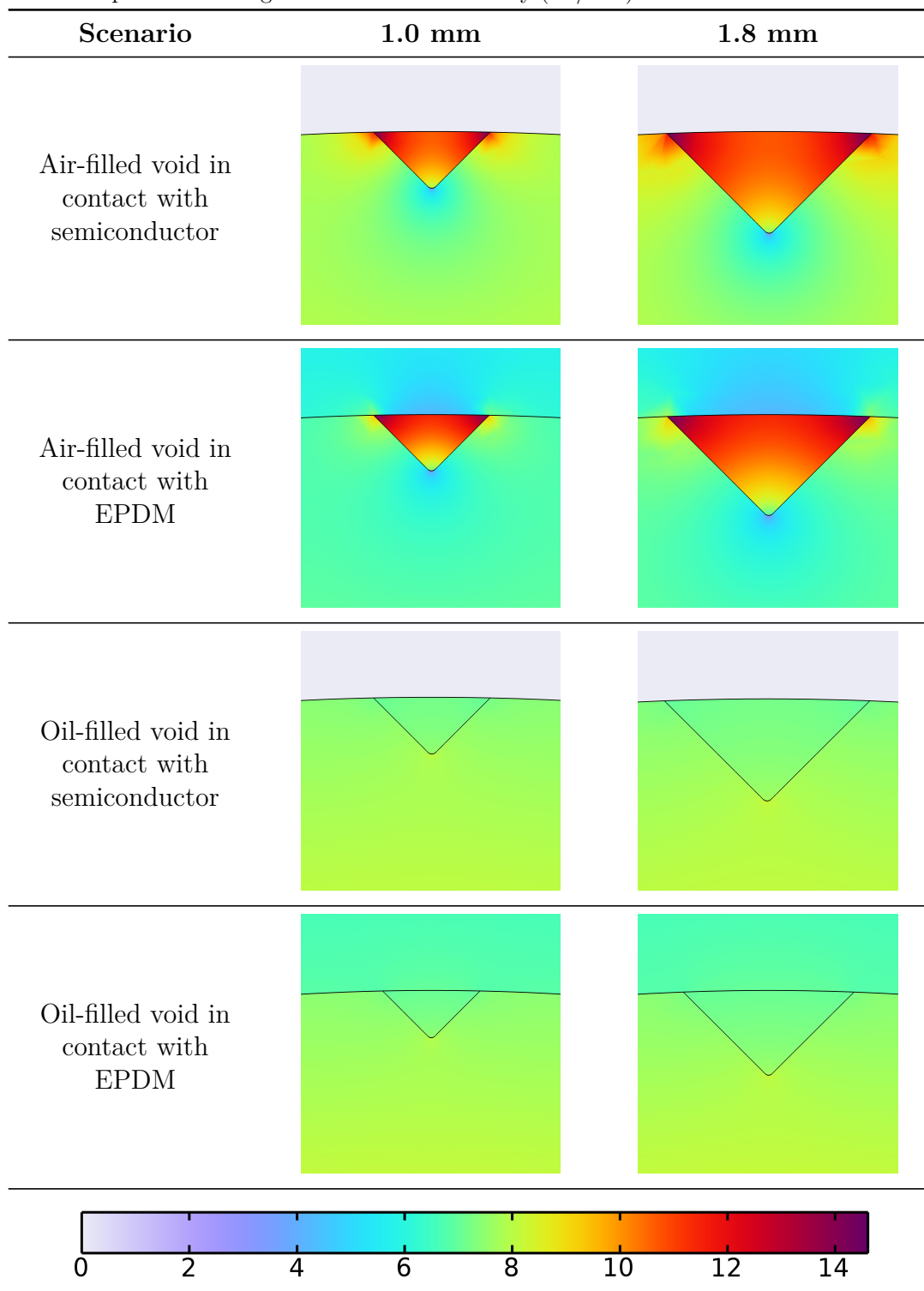
As seen in Table 6.2, for air-filled voids in contact with a semiconductor, there is a pronounced concentration of higher field intensity within the void compared to the surrounding XLPE insulation. Notably, higher field intensities are observed at the edges of the cuts, specifically at the triple-points where air, XLPE, and semiconductor meet, compared to the center of the cut. With EPDM as the material in contact with the void, the distribution of the electric field intensity extends into both the void and the insulation, consequently resulting in lower field enhancement at the triple-points.

In the oil-filled scenarios, the electric field intensity within and surrounding the void displays a more consistent distribution, due to the permittivity of the oil closely matching that of the insulating XLPE material, resulting in significantly reduced field enhancements.

6.3.2 Simulated electric field intensity

To accurately quantify electric field intensities for determining the FEF and calculating the PDIV, the field intensities across all scenarios and cut depths were simulated along the radial axis of the cable. These results were plotted in 1D graphs together with analytically calculated field intensities, based on the theory in Section 2.2.2, assuming an undamaged insulation surface. A visual representation of the simulation domain along the radial axis is shown in Figure 6.3.
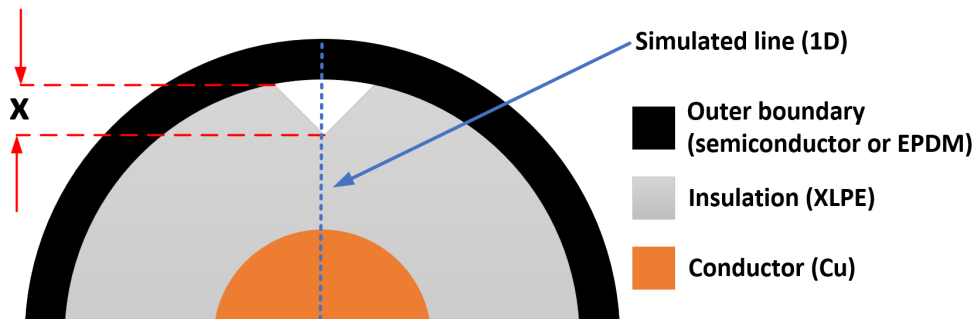
Figure 6.3: Representation of the simulation domain. ”x” marks the depth of the cuts.

It is important to note why the simulations were specifically performed along this radial axis, rather than focusing on the regions at the ”triple-point” of the cut where the electric field intensity peaked, as observed in Table 6.2. While the field intensity, and consequently the FEF is higher at these points, the much smaller gap distance at these locations results in a significantly higher breakdown voltage according to Paschen's Law, as detailed in Section 2.3.3, making these points less critical for PDIV prediction.

Simulations based on intended cut depths

Simulations were performed using the intended cut depths to understand the behavior of electric fields in response to a wider range of void sizes. Figures 6.4 to 6.7 present both the simulated electric field intensity and the analytically calculated field intensity derived from (2.7), assuming an undamaged insulation surface. The field intensities are plotted along the radial axis from the conductor to the insulation and surrounding material, zoomed in on the region near the defects to capture the deviations caused by the cuts precisely.

Figure 6.4 illustrates the electric field intensity for an air-filled void in contact with a semiconductor. Although the overall field intensity increases with deeper cuts, the local field intensity at the interface between the air-filled void and the semiconductor remains relatively consistent across different depths. This consistency indicates that while cut depth affects the overall distribution of the electric field, it does not significantly increase the local electric field intensity at the interface.

Figure 6.5 demonstrates the electric field intensity for an air-filled void in contact with EPDM material. Compared to the scenarios involving a semiconductor, there is a pronounced increase in the local field intensity at the interface with the EPDM. This effect is consistent across all cut depths, indicating that the EPDM material's properties significantly influence the field distribution, leading to enhanced local electric field intensities at the interface.

Figure 6.6 demonstrates how the silicon oil's permittivity, which is closer to that of the EPDM material than a perfect conductor, results in a much less drastic increase in the electric field intensity at the voids compared to the air-filled counterpart. This increase is notably localized at the edge of the cuts, closer to the conductor, compared to the air-filled scenarios.

Figure 6.7 shows, similarly to Figure 6.6, a relatively small field enhancement for the oil-filled voids in contact with EPDM. Additionally, the electric field intensity is lower than when in contact with a semiconductor, resulting in a lower field intensity than the analytically calculated field. This indicates that the silicone oil's similar permittivity to EPDM drastically decreases the field intensity when the oil-filled void is in contact with EPDM.

Figure 6.4: 1D plot of the simulated and analytically calculated electric field intensity for an air-filled void in contact with a semiconductor.

Figure 6.5: 1D plot of the simulated and analytically calculated electric field intensity for an air-filled void in contact with EPDM.
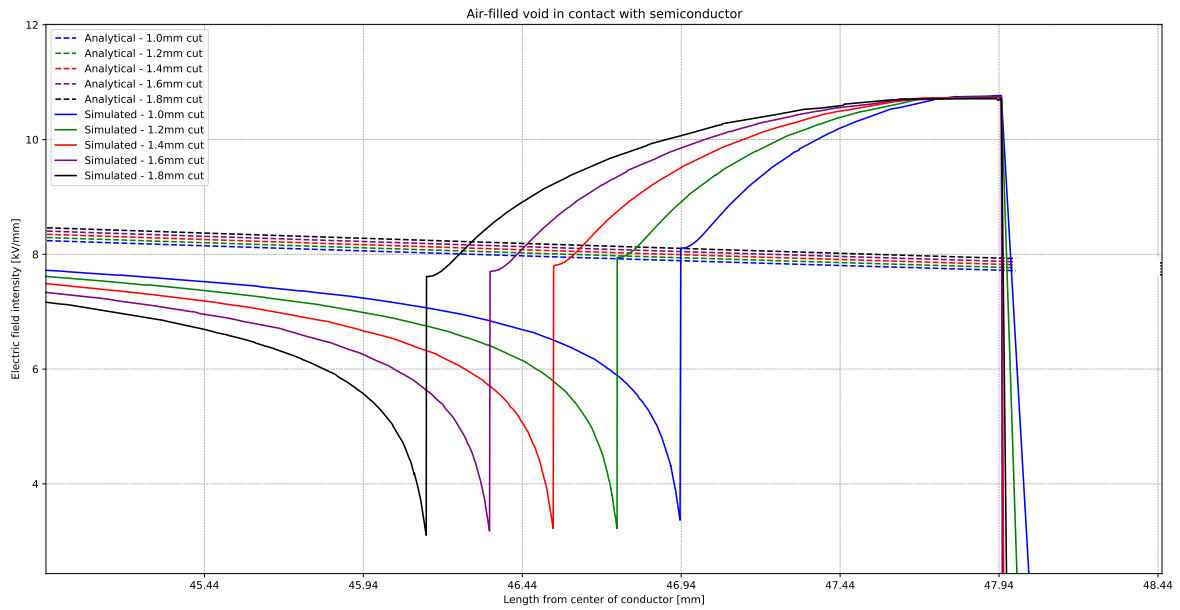
Figure 6.6: 1D plot of the simulated and analytically calculated electric field intensity for an oil-filled void in contact with a semiconductor.
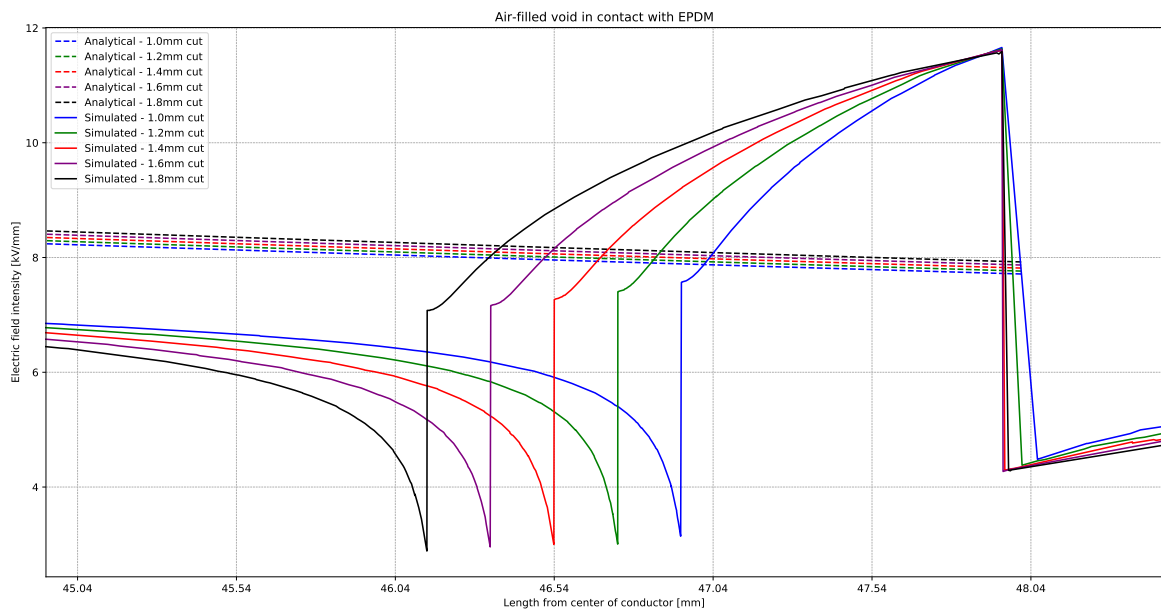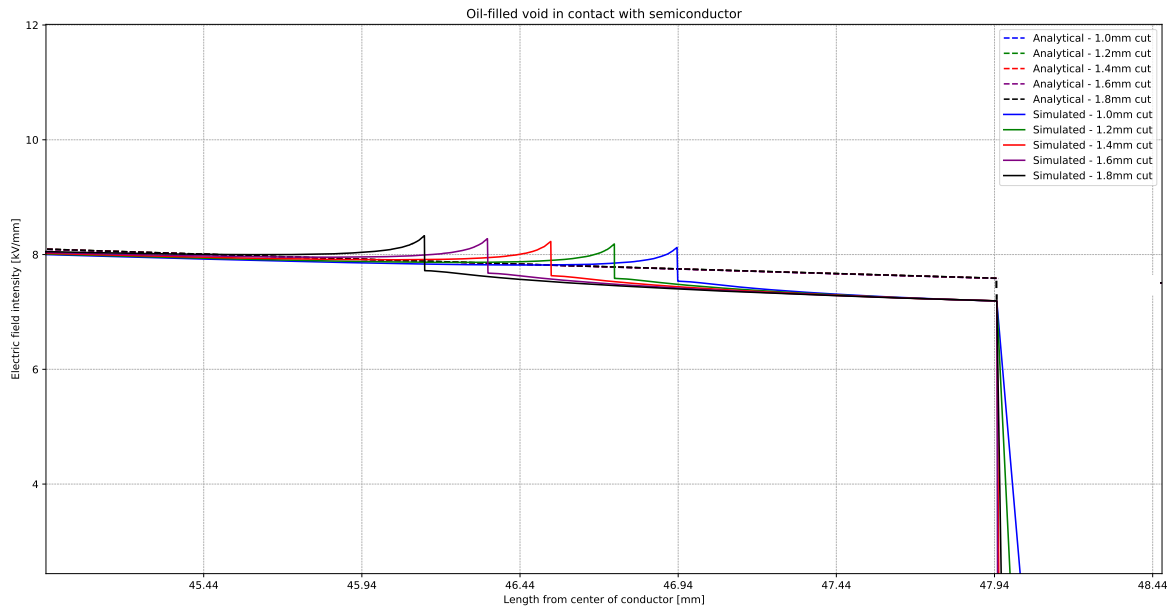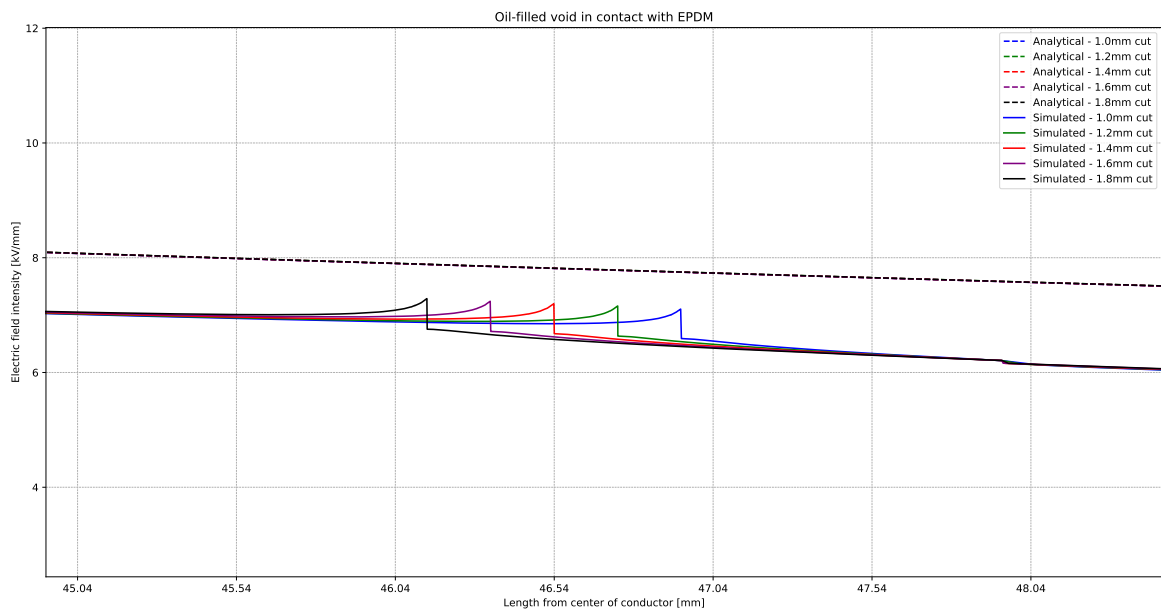

Figure 6.7: 1D plot of the simulated and analytically calculated electric field intensity for an oil-filled void in contact with EPDM

Simulations based on measured cut depths

The same simulations were repeated using the measured cut depths. These showed a similar trend to those performed in Section 6.3.2 and can be found in Appendix C.

6.4 Calculation of the Field Enhancement Factor (FEF) and Partial Discharge Inception Voltage (PDIV)

The simulated electric field values for all scenarios and cut depths were exported from COMSOL Multiphysics®, to perform precise calculations of the FEF and PDIV in Python.

Firstly, for the air-filled scenarios, the initial breakdown field, E_{bd}, was calculated with (6.3).

$$E_{bd} = \frac{V_b}{d} \quad [\text{kV/mm}] \tag{6.3}$$

where V_b is the breakdown voltage calculated from Paschen's Law (kV) (2.13), and d is the gap distance (mm). In oil-filled scenarios, the breakdown strength of 35 kV/mm for silicone oil [16] was used as E_{bd}, due to Paschen's Law only applying to gases.

The FEF, which quantifies the intensification of the electric field by defects compared to an undamaged scenario, as detailed in Section 2.2.4, was calculated using (6.4).

$$FEF = \frac{E_{local}}{E_{reference}} \tag{6.4}$$

where E_{local} was the highest electric field intensity caused by the cuts, exported from the simulations in Section 6.3.2, and $E_{reference}$ was the analytically calculated field intensity at the same radial distance but in an undamaged insulation scenario, derived from Equation 2.7.

The FEF was then utilized to calculate the corrected breakdown field, $E_{bd,corr}$, which accounts for the variations in field strength due to the defects, calculated by (6.5).

$$E_{bd,corr} = \frac{E_{bd}}{FEF} \quad [\text{kV/mm}] \tag{6.5}$$

Then, the PDIV for each scenario and cut depth were calculated to determine the voltage at which PD would initiate. The equation for PDIV (6.6) was based on (2.7), using the corrected breakdown field, $E_{bd,corr}$.

$$PDIV = E_{bd,corr} \cdot r_2 \cdot \ln(\frac{r_2}{r_1}) \quad [\text{kV}] \tag{6.6}$$

where r_1 is the radius of the conductor (mm), and r_2 is the distance from the center of the conductor to the respective depth of the cut (mm).

The resulting voltage reflects the maximum voltage applied to the conductor before PD occurs in the void, accounting for the electric field influenced by the geometry of the cuts. The Python script used for these calculations can be found in Appendix D.

6.4.1 Resulting FEF and PDIV

The results for the calculated FEF and PDIV are presented in four tables. The first two tables, Table 6.3 and 6.4, show the results for the intended cut depths, and Table 6.5 and 6.6, presents the results for the measured cut depths.

Table 6.3: Calculated FEF and PDIV for the intended cuts, air-filled

Condition	Cut depth	FEF	PDIV at different pressures		
			1 bar	2 bar	3 bar
Air-filled void in contact with semiconductor	1.0 mm	1.394	54.58 kV	97.37 kV	137.39 kV
	1.2 mm	1.383	53.03 kV	94.92 kV	134.15 kV
	1.4 mm	1.371	51.93 kV	93.17 kV	131.81 kV
	1.6 mm	1.365	50.56 kV	90.93 kV	128.81 kV
	1.8 mm	1.351	49.79 kV	89.73 kV	127.23 kV
Air-filled void in contact with EPDM	1.0 mm	1.510	50.41 kV	89.93 kV	126.89 kV
	1.2 mm	1.497	48.98 kV	87.68 kV	123.91 kV
	1.4 mm	1.483	47.87 kV	85.91 kV	121.57 kV
	1.6 mm	1.475	46.78 kV	84.14 kV	119.29 kV
	1.8 mm	1.461	46.03 kV	82.95 kV	117.61 kV

Table 6.4: Calculated FEF and PDIV for the intended cuts, oil filled

Condition	Cut depth	FEF	PDIV
Oil-filled void in contact with semiconductor	1.0 mm	1.048	534.98 kV
	1.2 mm	1.052	445.83 kV
	1.4 mm	1.053	381.91 kV
	1.6 mm	1.055	334.52 kV
	1.8 mm	1.056	296.55 kV
Oil-filled void in contact with EPDM	1.0 mm	0.917	611.66 kV
	1.2 mm	0.920	509.68 kV
	1.4 mm	0.921	436.56 kV
	1.6 mm	0.923	382.34 kV
	1.8 mm	0.924	338.91 kV

Table 6.5: Calculated FEF and PDIV for the measured cuts, air-filled

Condition	Cut depth	FEF	PDIV at different pressures		
			1 bar	2 bar	3 bar
Air-filled void in contact with semiconductor	0.5528 mm	1.418	60.88 kV	107.25 kV	150.40 kV
	0.6526 mm	1.411	59.09 kV	104.48 kV	146.78 kV
	1.0712 mm	1.390	54.09 kV	96.60 kV	136.37 kV
	1.0736 mm	1.388	54.14 kV	96.70 kV	136.51 kV
	1.1152 mm	1.398	53.65 kV	95.89 kV	135.42 kV
Air-filled void in contact with EPDM	0.5528 mm	1.535	56.21 kV	99.02 kV	138.85 kV
	0.6526 mm	1.521	54.79 kV	96.88 kV	136.10 kV
	1.0712 mm	1.505	56.21 kV	89.22 kV	125.96 kV
	1.0736 mm	1.507	49.84 kV	89.03 kV	125.68 kV
	1.1152 mm	1.502	49.64 kV	88.73 kV	125.31 kV

Table 6.6: Calculated FEF and PDIV for the measured cuts, oil-filled

Condition	Cut depth	FEF	PDIV
Oil-filled void in contact with semiconductor	0.5528 mm	1.042	984.59 kV
	0.6526 mm	1.044	832.08 kV
	1.0712 mm	1.050	503.91 kV
	1.0736 mm	1.049	503.00 kV
	1.1152 mm	1.051	483.93 kV
Oil-filled void in contact with EPDM	0.5528 mm	0.910	1126.76 kV
	0.6526 mm	0.914	951.17 kV
	1.0712 mm	0.918	576.68 kV
	1.0736 mm	0.918	575.37 kV
	1.1152 mm	0.919	553.06 kV

From the data presented in the tables, several consistent trends across all scenarios are observed. Notably, the PDIV decreases with deeper cuts, and for air-filled voids, the PDIV increases with elevated pressures.

In scenarios involving air-filled voids, whether in contact with semiconductor or EPDM, the FEF decreases as the cut depth increases. However, while the FEF trend is similar for both materials, the resulting PDIV is lower when voids are in contact with EPDM compared to semiconductor. In contrast, oil-filled voids show much lower FEF and significantly higher PDIV than air-filled voids.

6.5 Comparing calculated and measured PDIV

The resulting PDIV obtained from simulations and calculations at various cut depths for different scenarios was compared with the empirical PDIV measurements of the cable end to evaluate the accuracy of the methodology to predict PDIV. Due to their significantly higher values, PDIVs for oil-filled scenarios are not included since they exceeded the measured values by several hundred kV. The comparison is presented in Figure 6.8.
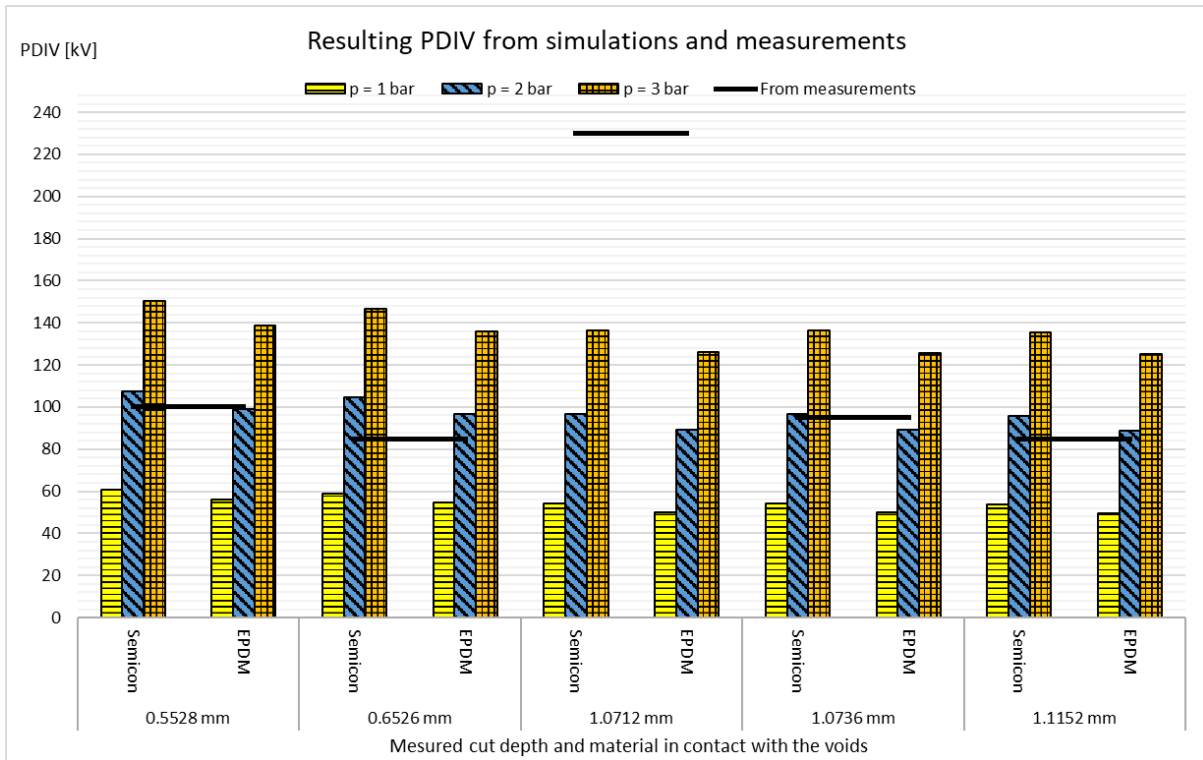
Figure 6.8: Comparison of the predicted PDIV from the air-filled void simulations and measured PDIV.

As seen in Figure 6.8, certain cut depths such as 0.5528 mm and 1.0736 mm show a close similarity between the measured and simulated values at a pressure of 2 bar. In contrast, other cut depths demonstrate larger differences, particularly at 1.0712 mm where the measured PDIV substantially exceeds all calculated air-filled results.

6.6 Discussion

Limitations of the simulation model

The simulation model's simplicity presents limitations, particularly regarding the geometric representation of voids. The physical cuts on the test object's insulation, detailed by the 3D scanning in Chapter 4, had irregularities that were not implemented in the simulation model. Furthermore, the use of generalized permittivity values for materials like silicone oil and XLPE insulation could have also altered the outcomes. Since a material's permittivity significantly influences electric field behavior, incorporating specific material data would improve the accuracy and ensure that the results would be even more representative of the test object's behavior.

Efforts were made to import the mesh from the laser scans into COMSOL for simulations of the electric field distribution and enhancement around the precise geometry of the cuts. However, due to various challenges and time constraints, this integration was unsuccessful.

Resulting FEF and PDIV

From the simulations and subsequent calculations, it was found that the PDIV was lower for air-filled voids in contact with EPDM compared to a semiconductor. One would expect the opposite, given that the semiconductor was modeled with infinitely high permittivity, leading to a pronounced distortion of the electric field. Table 6.2 reveals a higher field intensity at the triple-points, which is consistent with expectations of enhanced electric field concentration at these points. However, when the void was in contact with EPDM, the electric field intensity appeared to be more evenly distributed across the surface of the void rather than concentrated at the triple-points. This was confirmed by Figure 6.5, where the field intensity was higher at the interface between void and EPDM, along the radial axis. This explains why the resulting PDIV was lower for voids in contact with EPDM.

Additionally, the simulations showed an unexpected trend of a slight increase in FEF with larger oil-filled voids. This was most likely because of the more uniform electric field distribution within the voids caused by the silicone oil. This uniformity reduced the electric field intensification typically observed at the void boundaries, thereby slightly increasing the FEF as the void size increased.

The notably high PDIV observed in oil-filled void scenarios underscores the significant impact of the dielectric strength of silicone oil, which is substantially higher than that of air. This characteristic of silicone oil, having a breakdown strength of 35 kV/mm, substantially increased the PDIV, reflecting its potential to sustain higher electric fields without initiating discharge. However, it is important to note that these values more accurately represent the breakdown voltage, not the voltage at which PD is initiated. This is because the dielectric strength used for calculations corresponds to the material's capability to prevent complete breakdown, rather than just the initiation of PD. Consequently, the actual PDIV for oil-filled voids could be lower than those presented.

The lack of specific pressure data within the test object's voids adds a layer of uncertainty to PDIV estimations, particularly since Paschen's Law, which is central to these calculations, heavily depends on the product of pressure and distance.

Comparing simulated and measured PDIV results

The simulations generally predicted PDIV values quite accurately, despite the model's simplifications, assuming that the physical voids experienced a pressure close to 2 bar during the PDIV measurements. It was also seen that the material in contact with the void, whether semiconductor or EPDM, did not significantly influence the simulated PDIV values as much as the pressure did.

For the cut depths of 0.5528 mm and 1.0736 mm, the simulated PDIV closely matches the measured values in scenarios of an air-filled void in contact with a semiconductor and EPDM, respectively, both at 2 bar pressure.

However, for the cut depths of 0.5528 mm and 1.1152 mm, the simulated PDIV did not match as closely with the measured values. Assuming that the pressure could vary around 2 bar, the simulations would still predict PDIV values close to the measured ones if the pressure in these voids were slightly below 2 bar.

The exception was observed at the cut depth of 1.0712 mm, where the significant increase in measured PDIV did not correspond with any of the simulated values. This may be due to the presence of silicone oil in the cut region, a substantially higher pressure within the void, or a combination of both factors, as mentioned in Section 3.5.

7 Discussion

This thesis explored the use of 3D laser scanning and simulations to predict PDIV in HV cable ends. This was done by introducing defects in the form of cuts and scanning these to determine the depths. These depths were then used in electric field simulations, which served as the base for calculating the FEF, used for the subsequent prediction of PDIV based on Paschen's Law. These PDIV values were compared to empirically measured PDIV values for the physical cable end, to validate the methodology. While this research provided insightful data, it also revealed issues affecting the results' accuracy and applicability in practical settings.

The precision and accuracy of the data derived from 3D scans, specifically the measured depths of the cuts, played an important role in the electric field simulations. The rough and irregular cuts, resulting from the tools used to make the cuts, introduced uncertainties in the resulting 3D scans, which could have misrepresented the cuts as shallower than they were. This could lead to variations between the predicted and empirically measured PDIV. By improving both the method and tools used for making the cuts to ensure they are easily reproducible, and refining the scanning procedures, the scans would more accurately reflect the true geometry and depths of the cuts. This would further validate the methodology for predicting PDIV by enabling more precise comparisons with the measured PDIV of controlled defects. In practical jointing scenarios, where potential defects are often irregular or rough, developing a specific scanning procedure to ensure the capture of the true geometry of these defects would enhance the reliability of PDIV predictions in real-world scenarios.

Furthermore, the electric field simulations in this study faced some limitations due to the simplified simulation model, particularly the use of 'ideal' cuts and generalized permittivities for the materials. The maximum depth derived from the 3D scans was used rather than a detailed mesh of the actual cut geometry, which was not integrated into the model due to technical limitations and time constraints. These simplifications could potentially impact the reliability of the calculated FEF, and consequently the predicted PDIV. A more detailed simulation model, based on the actual geometry obtained from the scans, and utilizing precise material properties mirroring the physical objects' materials would allow for more representative PDIV predictions and their applicability to real-world scenarios. However, the use of such detailed simulation models would significantly increase the computational time required to run the electric field simulations.

While the challenges for 3D scanning and limitations for the simulations were important factors for the predictions of PDIV, physical factors could also influence the reliability of these. During the study, a significant observation was the impact of experimental conditions on PDIV predictions, like pressure, location of the cuts, and the presence of silicone oil. Initially, the focus was on investigating air-filled voids due to the extensive theory behind breakdown in gases, and to avoid exceeding the rated voltage for the test setup during PDIV measurements. However, in this study, the presence of residual silicone oil in the voids was found to be the most influential factor on the predicted PDIV, more so than pressure variations or the location of the cuts, whether in contact with semiconductor or EPDM. Despite thorough cleaning procedures, completely removing silicone oil from the cut regions proved challenging, suggesting a need for improved cleaning methods or alternative lubrication materials. However, silicone oil is commonly used as a lubricant in practical jointing scenarios, emphasizing the need to develop a more precise method for predicting PDIV in liquid-filled voids to enable more accurate predictions. It was also observed that the pressure variations, while impacting PDIV predictions, were found to be relatively consistent throughout the study, typically around 2 bar based on comparisons between PDIV measurements and calculated PDIV predictions for different pressures.

Although the thesis demonstrated the methodology's potential under laboratory conditions, translating these findings to real-world applications could introduce additional challenges. Field conditions often include more variable factors, such as inconsistent temperatures and varying installation procedures, which were not considered in this study. These factors could influence the reliability of the methods used for predicting PDIV, indicating the need for further research. Even though PDIV predictions could be considered a more strict verification than traditional PD measurement testing, it would be more practical and efficient, as it can be performed directly at the site of the jointing without the need for setting up test circuits or utilizing other PD detection methods. Additionally, this method would exceed the conventional visual quality control performed by operators, providing documented assurance that the joint will not be a source of PD during operation. Regardless, the methodology shows great promise for enhancing quality control in practical HV cable jointing scenarios, though additional tests involving various types of defects and on-site applications would be necessary to further validate its effectiveness.

8 Conclusion and future work

8.1 Conclusion

This thesis has demonstrated the potential of 3D laser scanning technology for predicting the PDIV of air-filled voids in HV cable ends. By integrating cut depths derived from 3D scans into simulations and calculations, and comparing these with empirical PDIV measurements, the predicted PDIV proved quite accurate, under the assumption of a void pressure around 2 bar in the test setup.

The HandySCAN BLACK™|Elite 3D scanner utilized in the study proved effective and sufficiently accurate to create precise 3D models of the defect regions. However, obtaining accurate scans necessary for detailed geometrical analysis depended heavily on the scanning procedure.

The simplified simulation model used for calculating the FEF and predicting the PDIV proved effective. Implementing the physical geometry of the cuts derived from the 3D scans, and specific material properties could provide more accurate and reliable results.

The study also revealed the impact of silicone oil, pressure variations, and defect location on the PDIV predictions' reliability. Silicone oil in the defect region was found to be the most impactful factor, significantly influencing the accuracy of the predicted values. Although void pressure variations affected PDIV predictions, these were relatively consistent throughout the study. In contrast, the location of the defect, whether in contact with EPDM or semiconductive material, had less impact on the predicted PDIV values. This emphasizes the importance of controlling these conditions to ensure the predictions are valid and applicable to real scenarios.

In conclusion, the findings confirm that 3D laser scanning technology can significantly enhance the quality control of HV cable installations under known conditions.

8.2 Future work

Further research is needed to validate and optimize this methodology based on the findings and challenges identified in this thesis. The following recommendations are proposed for continued development:

- Investigate and implement methods for making more precise and cleaner cuts in the insulation, reducing irregularities and material flings. This could enhance the accuracy of the electric field simulations, and consequently the FEF.

- Improve the simulation model to include exact geometries of the defects from 3D scans, as well as incorporating specific material data. This would increase the precision of the simulations and consequently the accuracy of PDIV predictions.

- Develop techniques to accurately measure and control the pressure within voids while ensuring they remain free from residual oil or explore using alternative lubricants or lubrication-free methods for PMJ installation. Precise control over these conditions is essential for confirming and refining the methodology used to predict PDIV, enhancing the accuracy and reliability of results.

- Further validate the methodology used to predict PDIV by comparing predicted values with more empirically measured PDIV values.

- Use the methodology for predicting PDIV of various types of defects. This will help validate how 3D laser scanning and PDIV estimation can be applied to other common defects found in HV cable jointing.

- Further validate the methodology for predicting PDIV through more empirical PDIV measurements across various setups under controlled conditions.

- Develop methods to accurately predict PDIV in liquid-filled voids, enhancing PDIV predictions for field applications such as jointing processes, where silicone oil is commonly used as a lubricant.

Bibliography

[1] Y. Xia, X. Song, J. He, Z. Jia and X. Wang, 'Simulation and partial discharge detection for typical defects of 10 kV cable the joint,' *The Journal of Engineering*, vol. 2019, Jan. 2019. DOI: `10.1049/joe.2018.8391`.

[2] S. Golubeva. 'What is laser 3D scanning?' (2022), [Online]. Available: `https://www.artec3d.com/learning-center/laser-3d-scanning` (visited on 11/04/2024).

[3] CREAFORM. 'Electrifying the Future with 3D Scanning Technologies,' CREA-FORM3D.COM. (2023), [Online]. Available: `https://www.creaform3d.com/blog/electrifying-the-future-with-3d-scanning-technologies/` (visited on 26/04/2024).

[4] E. Doedens, 'Surface quality determination of a high voltage cable end,' EP3901571A1, 21st Apr. 2020. [Online]. Available: `https://worldwide.espacenet.com/patent/search?q=pn%3DEP3901571A1`.

[5] A. Adam, A. Savastre, D. Dumitraș and R. Botiș, 'Study on the Use of 3D Scanning as a Verification Method in Technical Quality Control,' *Journal of Military Technology*, vol. 5, pp. 35–40, Jun. 2022. DOI: `10.32754/JMT.2022.1.05`.

[6] L. Deng, H. Deng, G. Liu, J. Zhao, H. Huang and L. Li, 'XLPE cable joint defects measurement method based on point cloud remapping,' *Measurement*, vol. 226, 2024. DOI: `https://doi.org/10.1016/j.measurement.2024.114139`.

[7] S. Duchesne, G. Parent, J. Moenecley and D. Roger, 'Prediction of PDIV in motor coils using finite element method,' pp. 638–641, 2016. DOI: `10.1109/ICD.2016.7547696`.

[8] G. S. Einan, 'Condition Assessment of Medium Voltage Cable Accessories,' M.S. thesis, Department of Electric Power Engineering, Norwegian University of Science and Technology, Norway, 2016.

[9] A. Haddad and D. Warne, *Advances in High Voltage Engineering*. London, United Kingdom: The Institution of Engineering and Technology, 2004, vol. 40, pp. 1–3, 139–149, 160, 471–481, 511–519, ISBN: 978-1-84919-038-1.

[10] RENblad. '9024 HS KABELNETT - TEORI FOR KABEL, SKJØTER OG EN-DEAVSLUTNINGER.' (2021), [Online]. Available: `https://www.ren.no` (visited on 08/04/2024).

[11] T. Worzyk, *Submarine Power Cables*. Berlin: Springer Berline Heidelberg, 2009, pp. 17–19, 30–32, 110–112, ISBN: 978-3-642-01269-3.

[12] E. H. Doedens, 'Topographical Impact on Space Charge Injection, Accumulation and Breakdown in Polymeric HVDC Cable Interfaces,' Ph.D. dissertation, Chalmers University of Technology, Gothenburg, Sweden, 2010.

[13] A. Küchler, *High Voltage Engineering*. Schweinfurt, Germany: Springer Vieweg, 2017, pp. 164–180, 199–203, 258–263, 501–503, ISBN: 978-3-642-11992-7.

[14] H. D. Young and R. A. Freedman, *University Physics with Modern Physics*, 15th edition. Pearson Education, 2020, pp. 718, 728–729, 753–756, ISBN: 978-0-13-515955-2.

[15] S. J. Ling, W. Moebs and J. Sanny, *University Physics Volume 2*. Houston, Texas: OpenStax, Oct. 2016. [Online]. Available: `https://openstax.org/books/university-physics-volume-2/pages/5-6-electric-field-lines` (visited on 11/05/2024).

[16] C. L. Wadhwa, *High Voltage Engineering*. Daryaganj, India: New Age International Ltd, 2007, pp. xiii, 1–2, 19, 181–183, ISBN: 978-81-224-2323-5.

[17] E. Kuffel, W. S. Zaengl and J. Kuffel, *High Voltage Engineering: Fundamentals*, 2nd ed. Oxford, Boston: Butterworth-Heinemann, 2000, pp. 209–210, ISBN: 978-0-7506-3634-6.

[18] Y. Fu, P. Zhang, J. Verboncoeur and X. Wang, 'Electrical Breakdown from Macro to Micro/Nano Scales: A Tutorial and a Review of the State of the Art,' *Plasma Research Express*, vol. 2, pp. 4–9, Jan. 2020. DOI: `10.1088/2516-1067/ab6c84`.

[19] F. Kreuger, *Industrial High Voltage Volume 1: Electric Fields, Dielectrics, Constructions*. IOS Press, 1991, pp. 76–83, 119, ISBN: 978-90-6275-561-5.

[20] M. Sze and M. Lachance. 'A Guide for Partial Discharge Measurements on medium voltage (MV) and high voltage (HV) apparatus. Part 1 - Introduction.' (Oct. 2020).

[21] H. M. Ryan, *High-Voltage Engineering and Testing 3rd Edition*. London, United Kingdom: The Insitution of Engineering and Technology, 2013, pp. 599–614, ISBN: 978-1-84919-263-7.

[22] *High-voltage test techniques - Partial discharge measurements*, IEC 60270, 2015.

[23] M. Sze and M. Lachance. 'A Guide for Partial Discharge Measurements on medium voltage (MV) and high voltage (HV) apparatus. Part 2 - Measurements according to IEC60270.' (Sep. 2020).

[24] M. U. Zuberi, A. Masood, E. Husain and A. Anwar, 'Estimation of partial discharge inception voltages due to voids in solid sheet insulation,' in *2013 IEEE Electrical Insulation Conference (EIC)*, 2013, pp. 124–128. DOI: `10.1109/EIC.2013.6554217`.

[25] L. Elorza Azpiazu, G. Almandoz, A. Egea, G. Ugalde and X. Badiola, 'Study of Partial Discharge Inception Voltage in Inverter Fed Electric Motor Insulation Systems,' *Applied Sciences*, vol. 13, no. 4, 2023. DOI: `10.3390/app13042417`.

[26] H. Illias, Teo Soon Yuan, A. H. A. Bakar, H. Mokhlis, G. Chen and P. L. Lewin, 'Partial discharge patterns in high voltage insulation,' in *2012 IEEE International Conference on Power and Energy (PECon)*, Dec. 2012, pp. 750–755. DOI: 10.1109/PECon.2012.6450316.

[27] CAPTURE3D. 'How Does a 3D Scanner Work?' CAPTURE3D.COM. (2024), [Online]. Available: `https://www.capture3d.com/knowledge-center/blog/how-does-a-3d-scanner-work` (visited on 11/04/2024).

[28] A.-B. Mostafa and M. Ebrahim, '3D Laser Scanners' Techniques Overview,' *International Journal of Science and Research (IJSR)*, vol. 4, pp. 5–611, Oct. 2015.

[29] iReal3D. 'What are markers, and why are they used in 3d scanning?' IREAL3DSCAN.COM. (Jan. 2024), [Online]. Available: `https://www.ireal3dscan.com/news/what-are-markers-and-why-are-they-used-in-3d-scanning/` (visited on 09/05/2024).

[30] *Power Cables with Extruded Insulation and Their Accessories for Rated Voltages above 150 kV (Um = 170 kV) up to 500 kV (Um = 550 kV) - Test Methods and Requirements*, IEC 62067, 2022.

[31] CREAFORM. 'HandySCAN 3D|BLACK Series,' CREAFORM3D.COM. (2024), [Online]. Available: `https://www.creaform3d.com/en/portable-3d-scanner-handyscan-3d` (visited on 19/04/2024).

[32] MLT. 'Nexans Surfical - QC av kabelender for terminering og skjøter,' MLT-NORGE.NO. (2024), [Online]. Available: `https://www.mltnorge.no/cases/nexans-surfical-qc-av-kabelender-for-terminering-og-skjoter/` (visited on 26/04/2024).

[33] OMICRON, 'MPD 800 User Manual,' 2021.

[34] OMICRON. 'MPD 800 Universal Partial Discharge Measurement and Analysis System,' OMICRONENERGY.COM. (2024), [Online]. Available: `https://www.omicronenergy.com/en/products/mpd-800/` (visited on 12/02/2024).

[35] OMICRON. 'CAL 542 Charge calibrator,' OMICRONENERGY.COM. (2024), [Online]. Available: `https://www.omicronenergy.com/en/products/cal-542/` (visited on 12/02/2024).

[36] COMSOL. 'An Introduction to the Theory of Electrostatics,' COMSOL.COM. (Feb. 2019), [Online]. Available: `https://www.comsol.com/multiphysics/electrostatics-theory?parent=electromagnetics-072-162` (visited on 12/04/2024).

Appendix A

MATLAB script for finding the maximum depths of height maps

The MATLAB script utilized for finding and presenting the maximum depths of the cuts, based on the height maps from the Surfical algorithm is presented below.

```matlab
clear all

figureFiles = {'filename1.fig, filename2.fig, ...'};

individualMinDepths_mm = zeros(size(figureFiles));

for fileIdx = 1:length(figureFiles)
    f = openfig(figureFiles{fileIdx}, 'invisible');
    individualMinDepth = inf;
    ax = findall(f, 'type', 'axes');
    for idx = 1:length(ax)
        if ~strcmpi(ax(idx).Tag, 'Colorbar')
            children = ax(idx).Children;
            for cIdx = 1:length(children)
                child = children(cIdx);
                if isprop(child, 'CData')
                    cData = get(child, 'CData');
                    individualMinDepth = min(
    individualMinDepth, min(cData(:)));
                end
            end
        end
    end
    individualMinDepths_mm(fileIdx) = individualMinDepth *
    1000;
    close(f);
```

```matlab
25  end
26
27  for fileIdx = 1:length(figureFiles)
28      fprintf('Minimum depth for %s is: %.4f mm\n', figureFiles{
        fileIdx}, individualMinDepths_mm(fileIdx));
29  end
```

Appendix B

Resulting PRPD plots from PDIV measurements

The PRPD plots from the PDIV measurements performed on the cable end with different cut depths are presented in the figures below. Here, the apparent charge, the PD rate, and at which phase angle the discharge pulses occurred are shown.
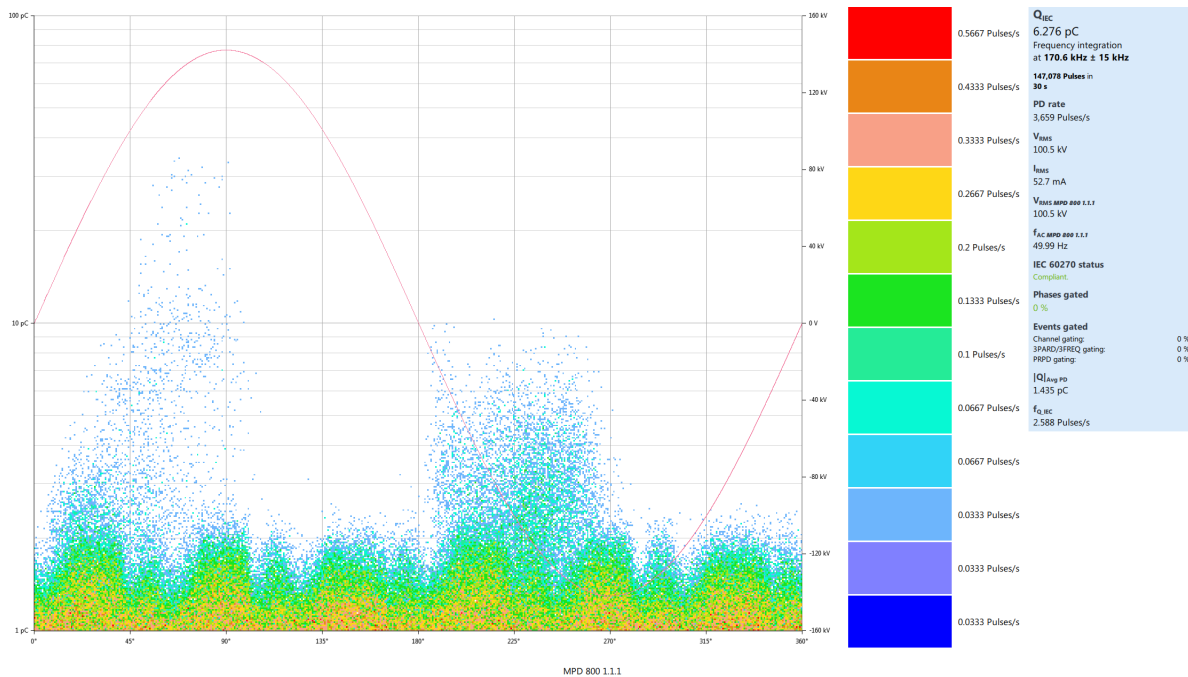
Cut depth = 0.5528 mm, PDIV = 100 kV
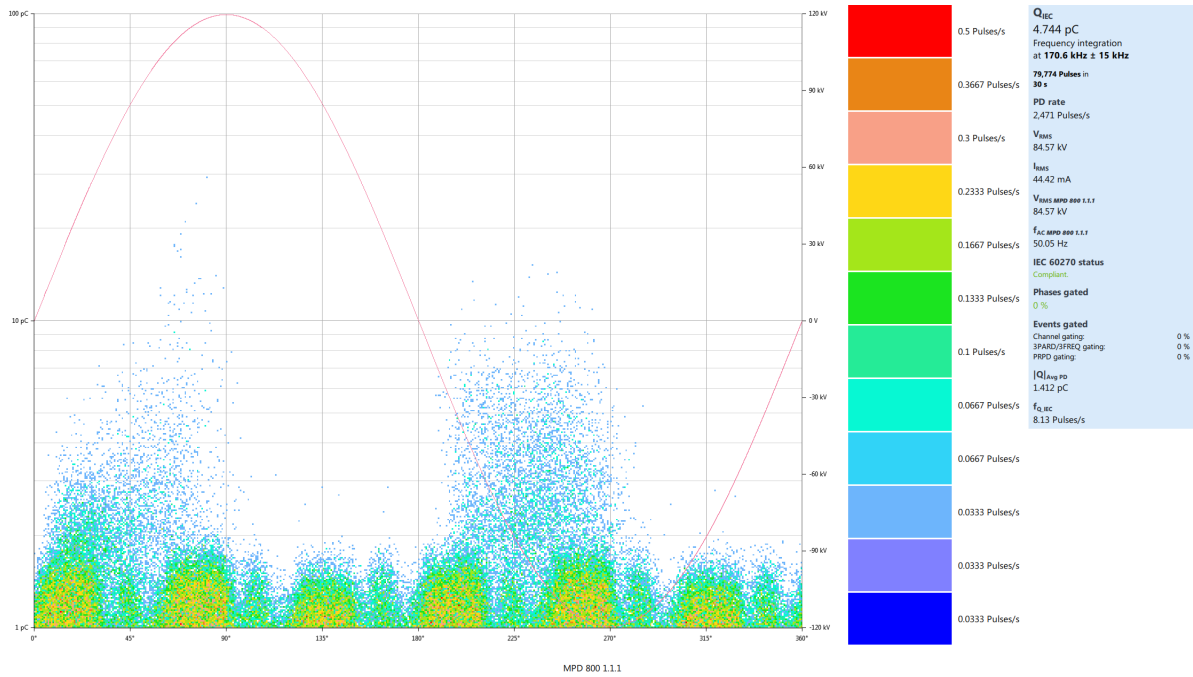
Cut depth = 0.6526 mm, PDIV = 85 kV
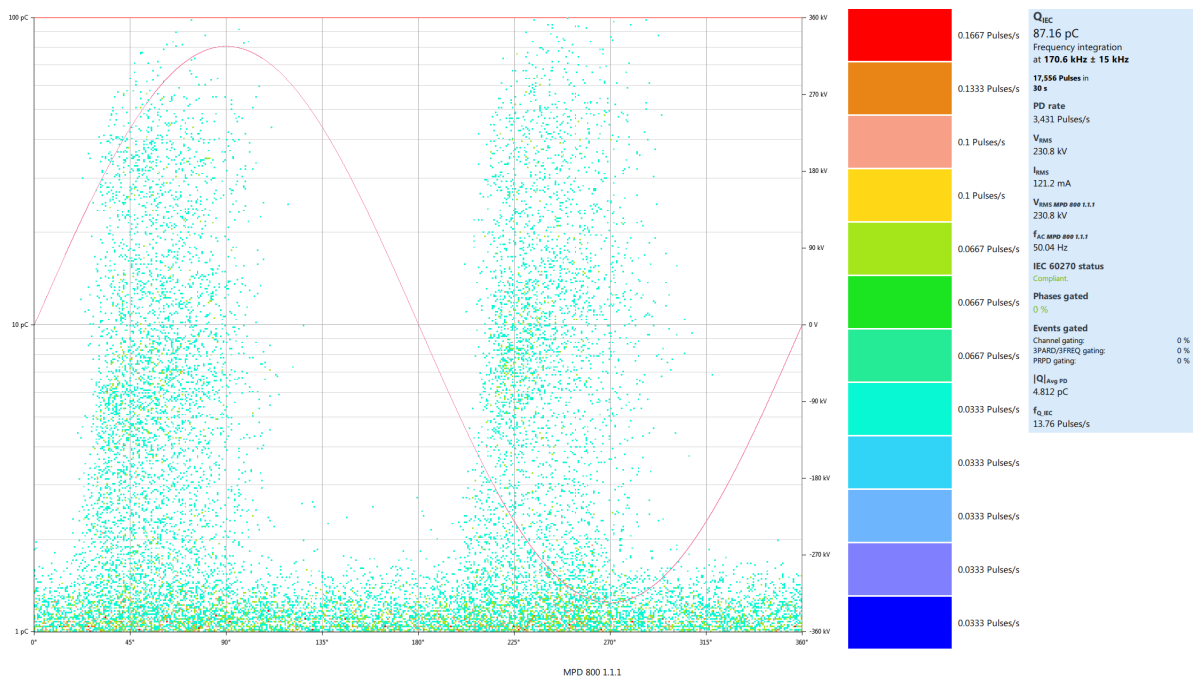
Cut depth = 1.0712 mm, PDIV = 230 kV
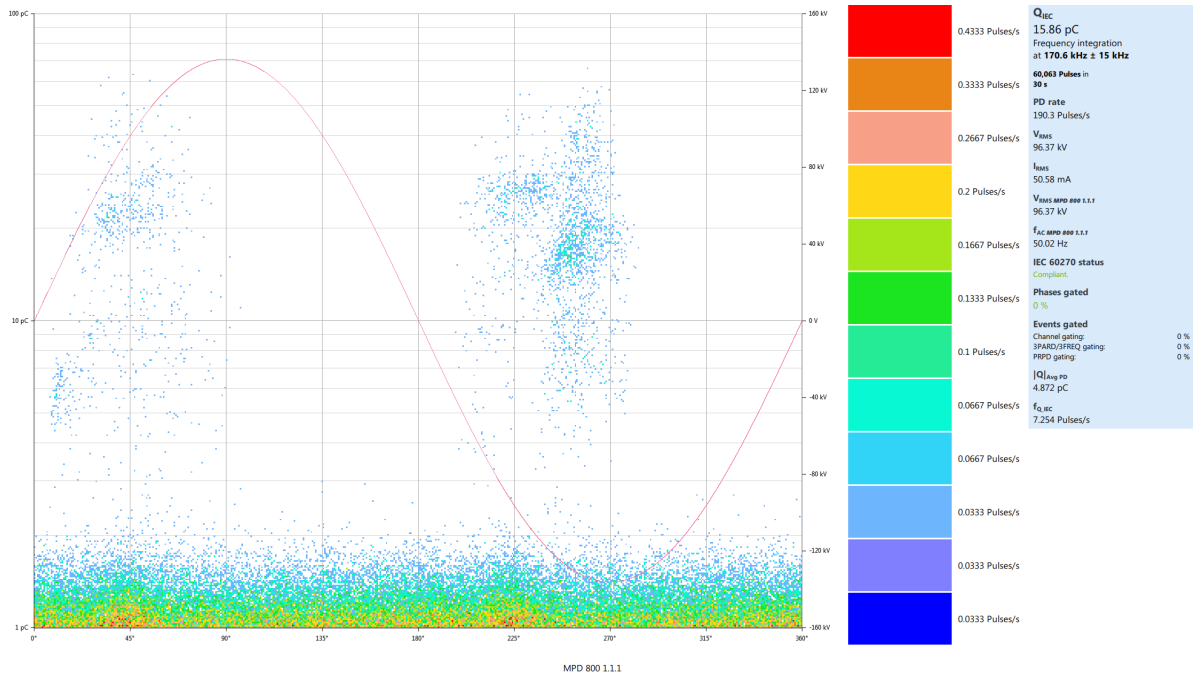
Cut depth = 1.0736 mm, PDIV = 95 kV
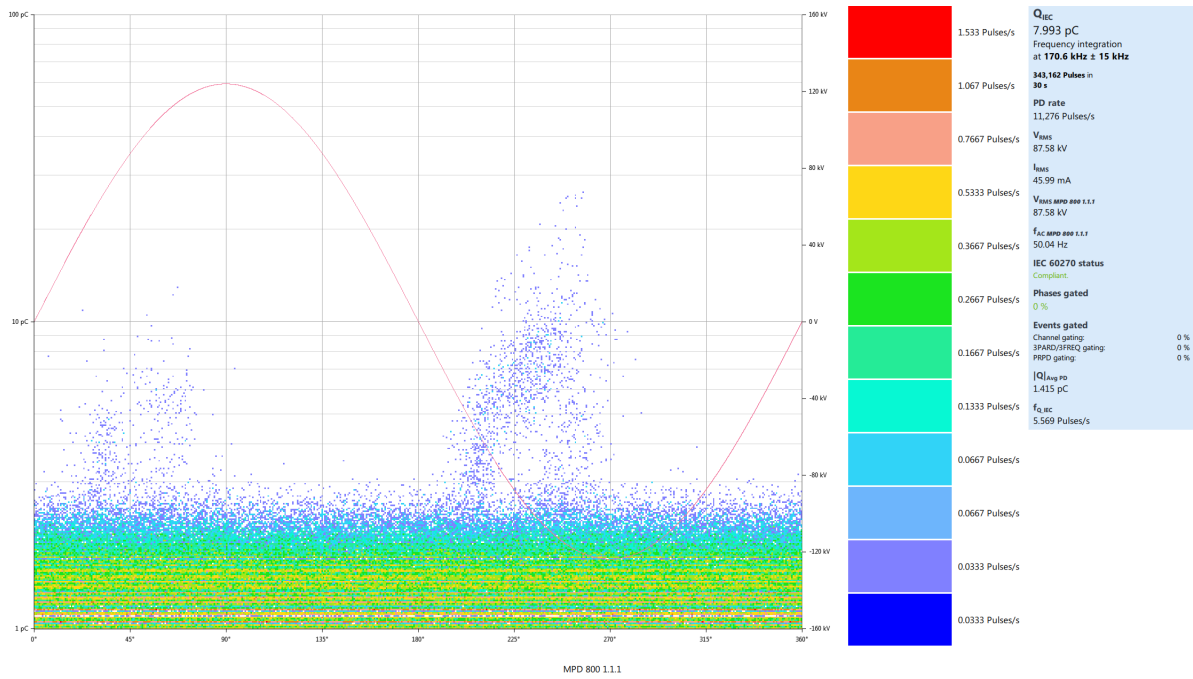
Cut depth = 1.1152 mm, PDIV = 85 kV

Appendix C

Resulting 1D plots from COMSOL simulations

This appendix presents the 1D plots of the electric field intensity along the radial axis of the simulation model. It is divided into the intended and the measured cut depths. For all scenarios, two plots are shown. One for the whole radial axis, ranging from the conductor to the outer boundary, and one zoomed into the region of the cuts.

Intended cut depths
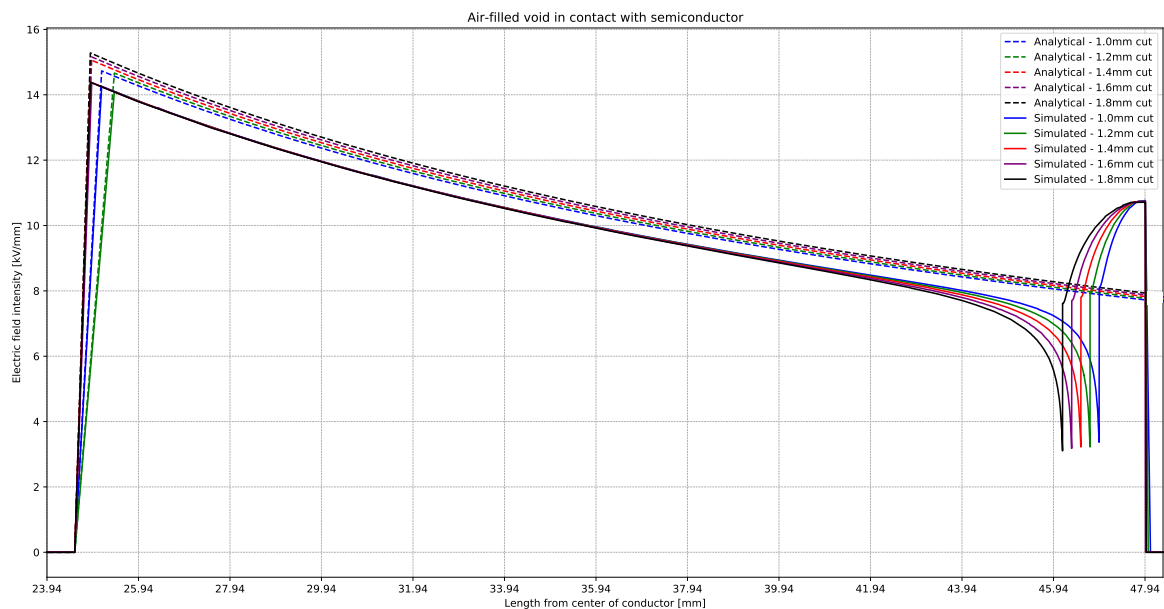
Air-filled void in contact with semiconductor.
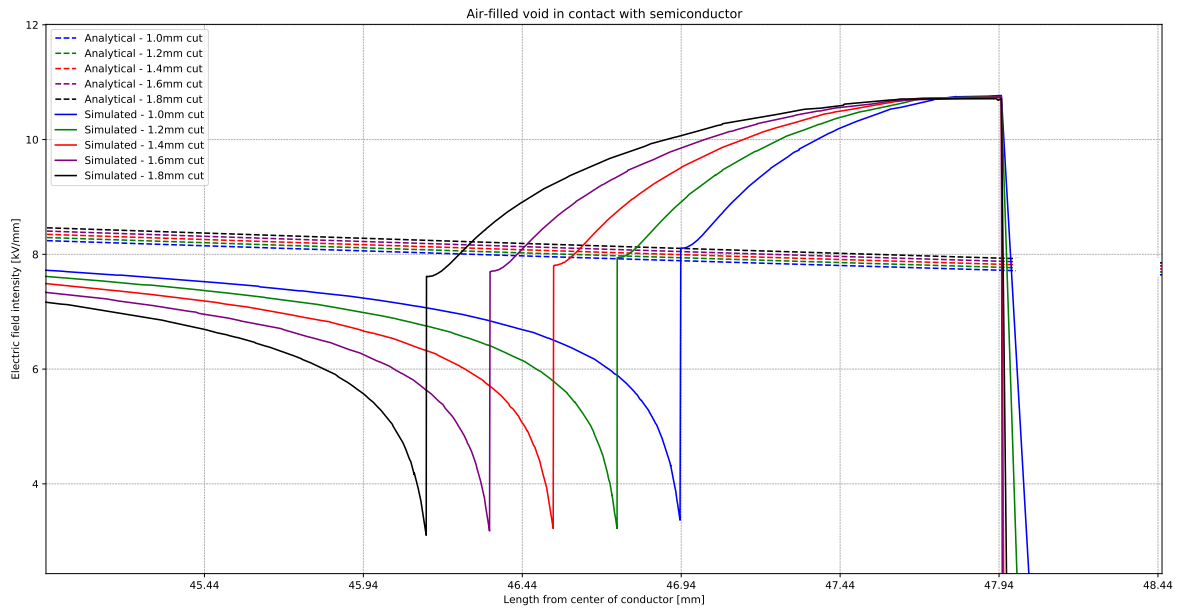
Air-filled void in contact with semiconductor, zoomed in.
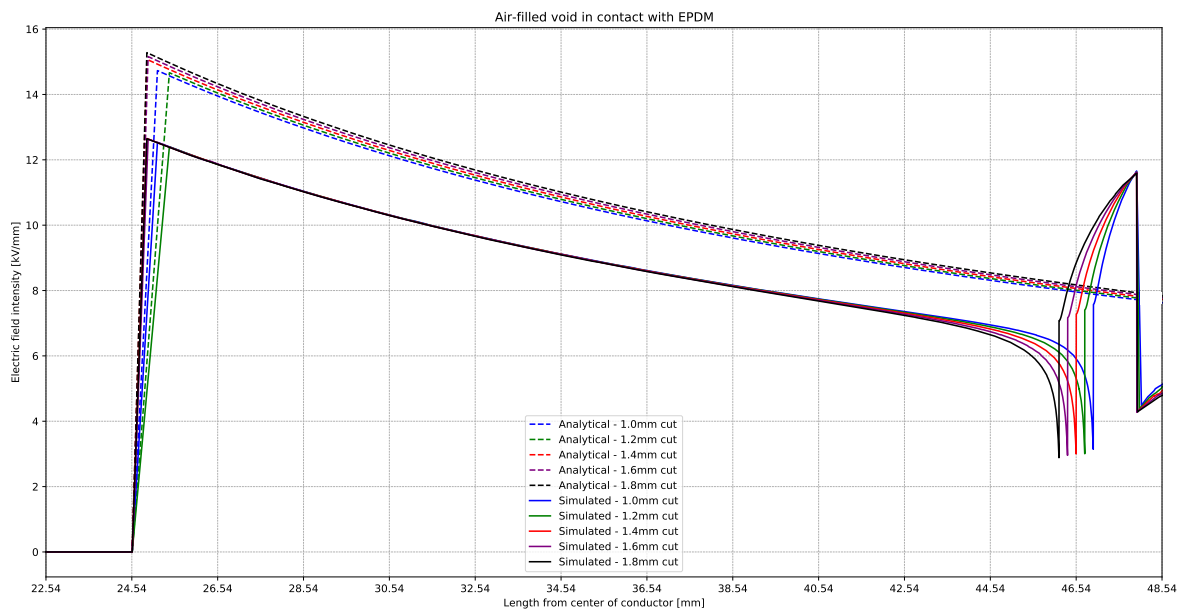
Air-filled void in contact with EPDM.
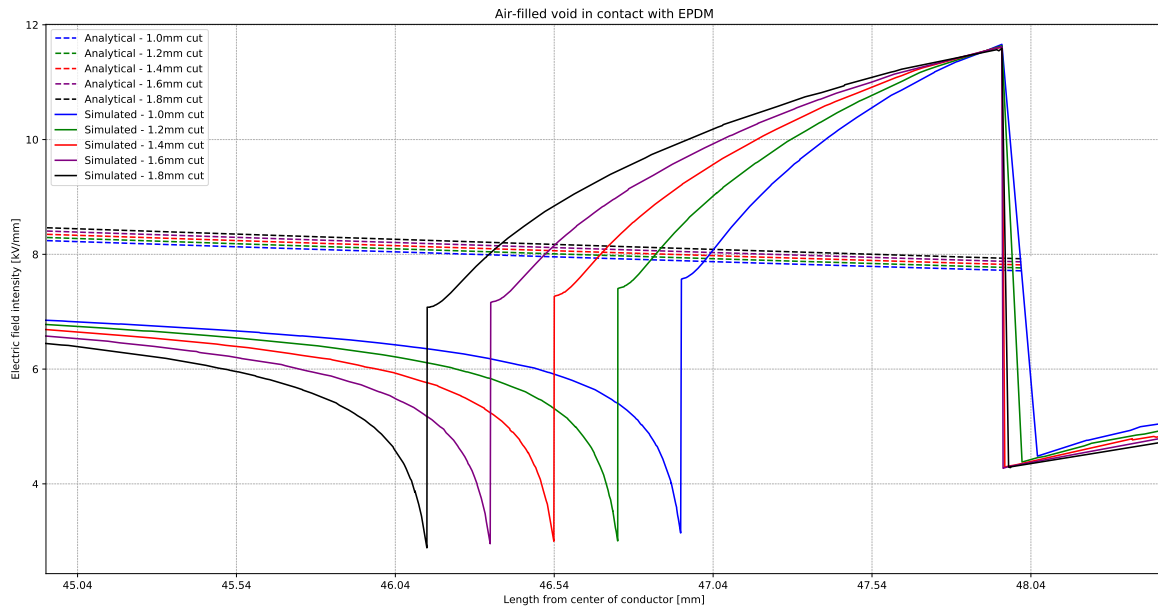
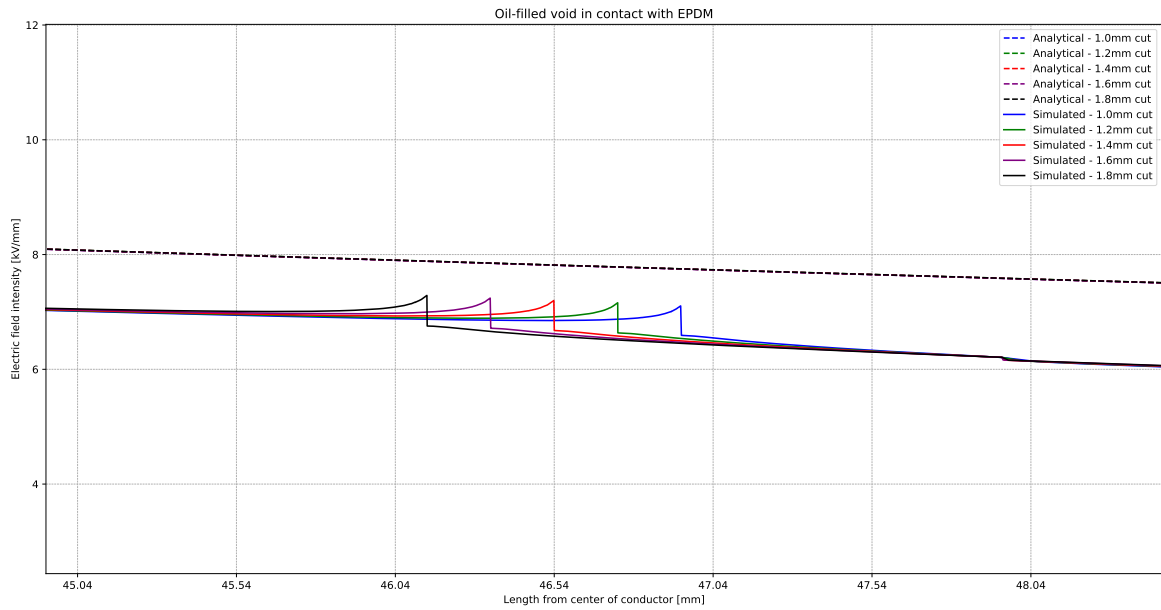Air-filled void in contact with EPDM, zoomed in.
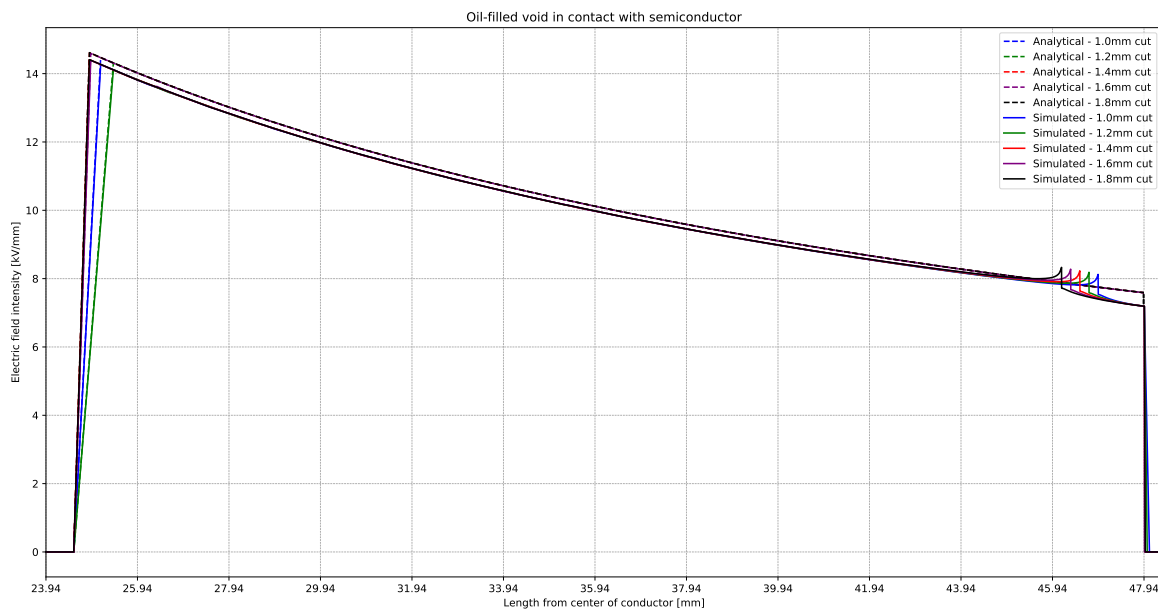
Oil-filled void in contact with semiconductor.
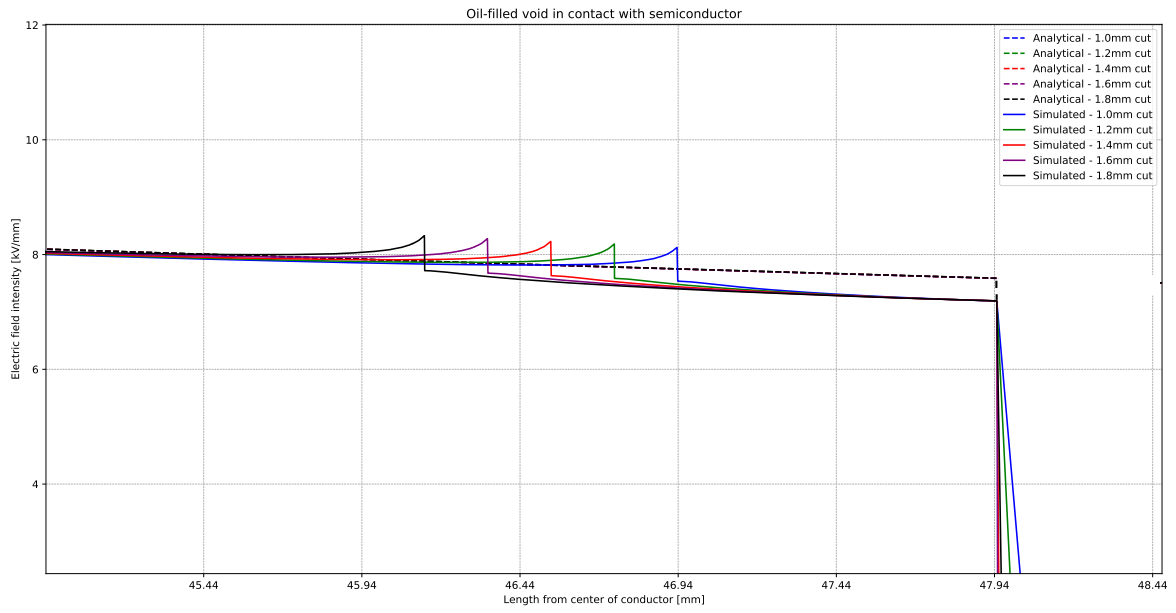
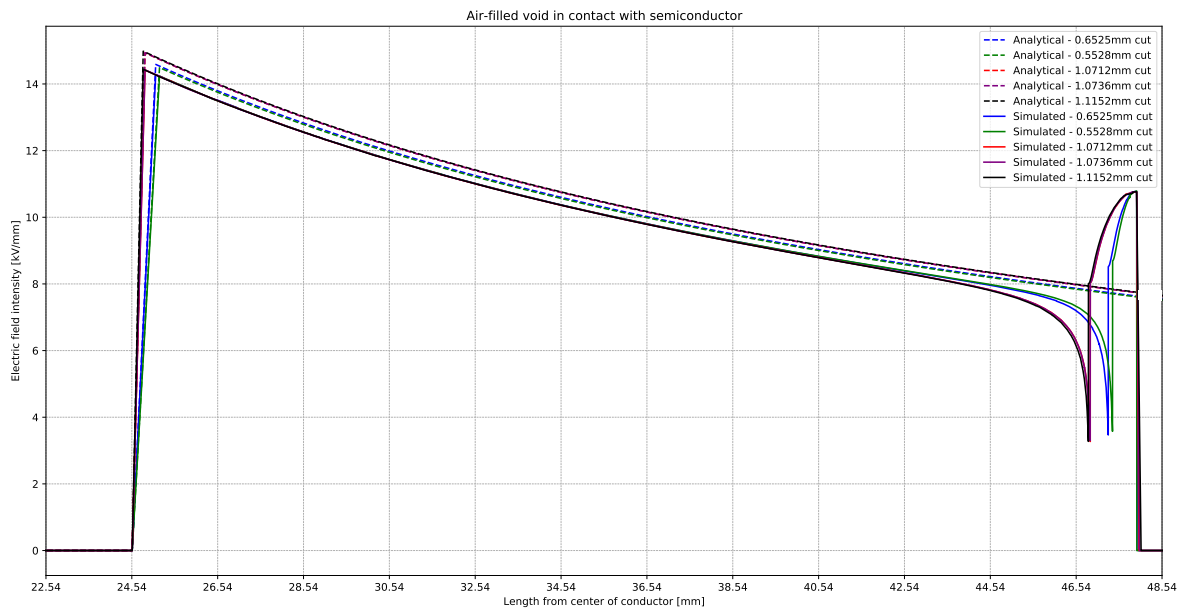Oil-filled void in contact with semiconductor, zoomed in.
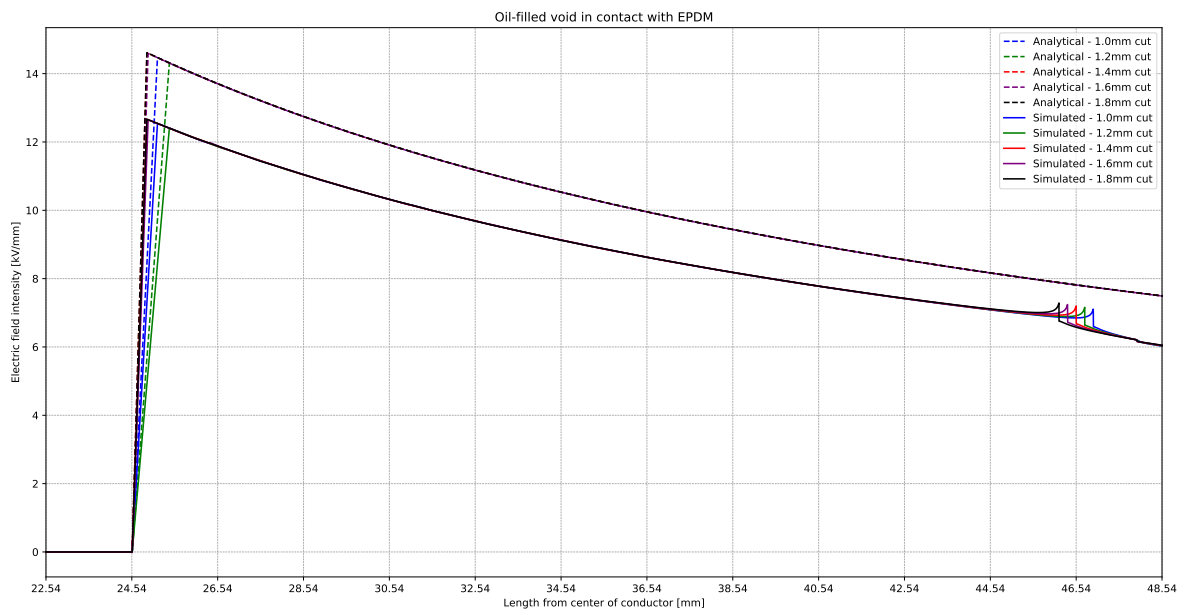
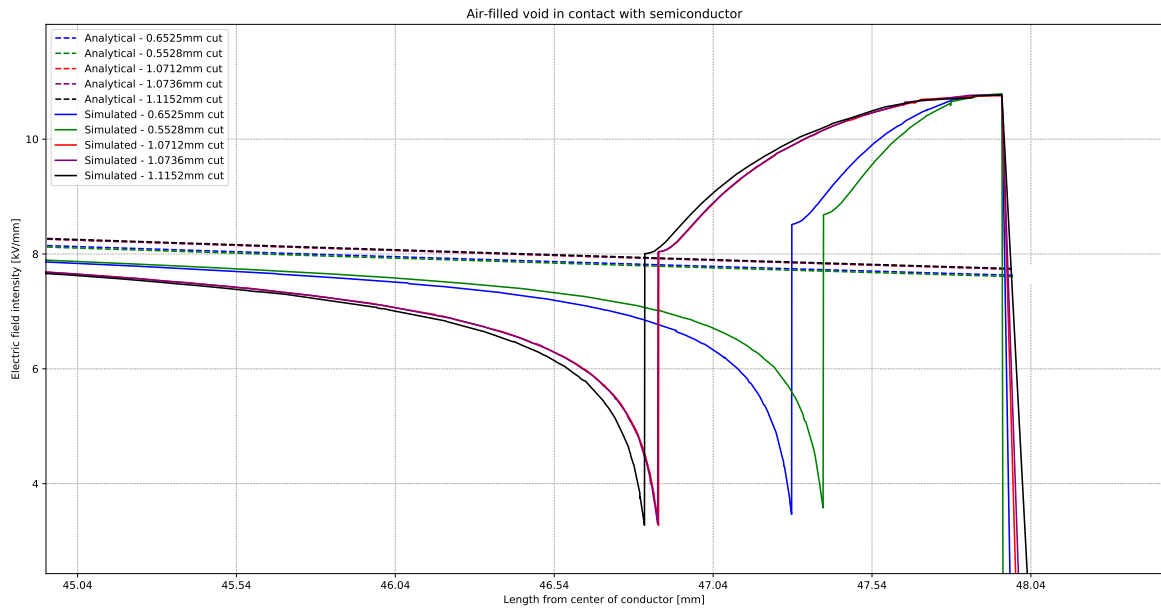Oil-filled void in contact with EPDM.

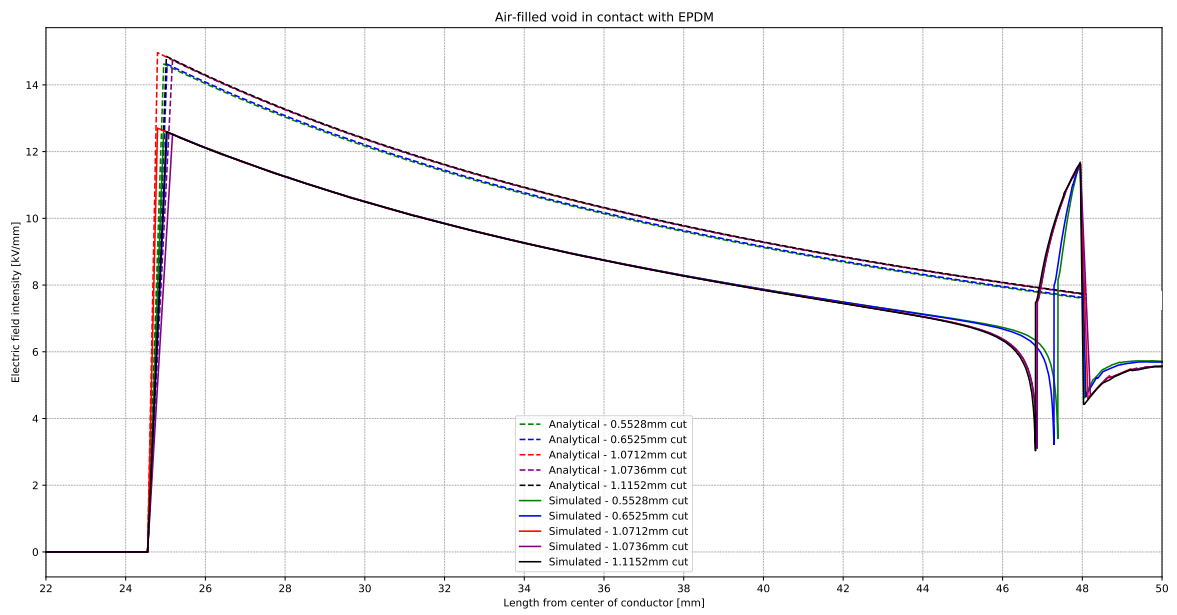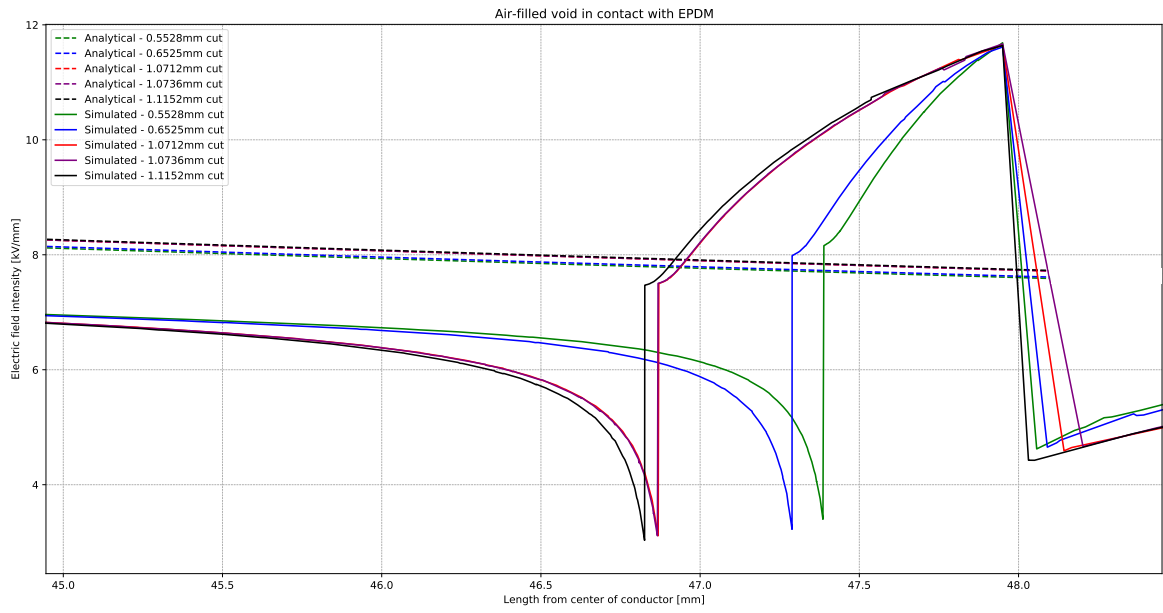Oil-filled void in contact with EPDM, zoomed in.

Measured cut depths

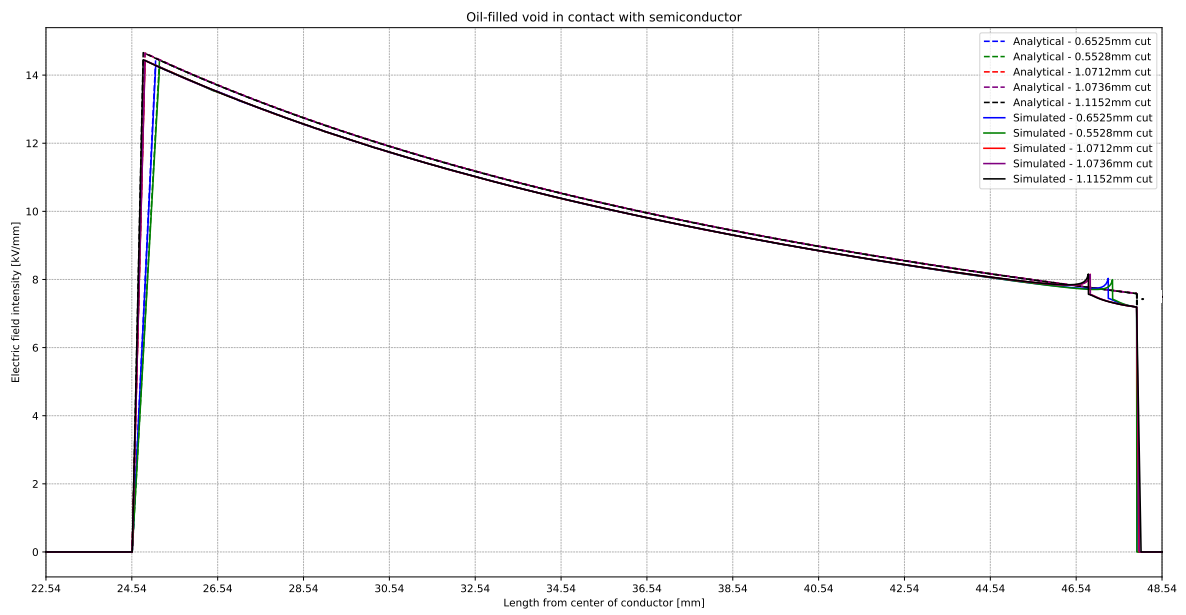Air-filled void in contact with semiconductor.

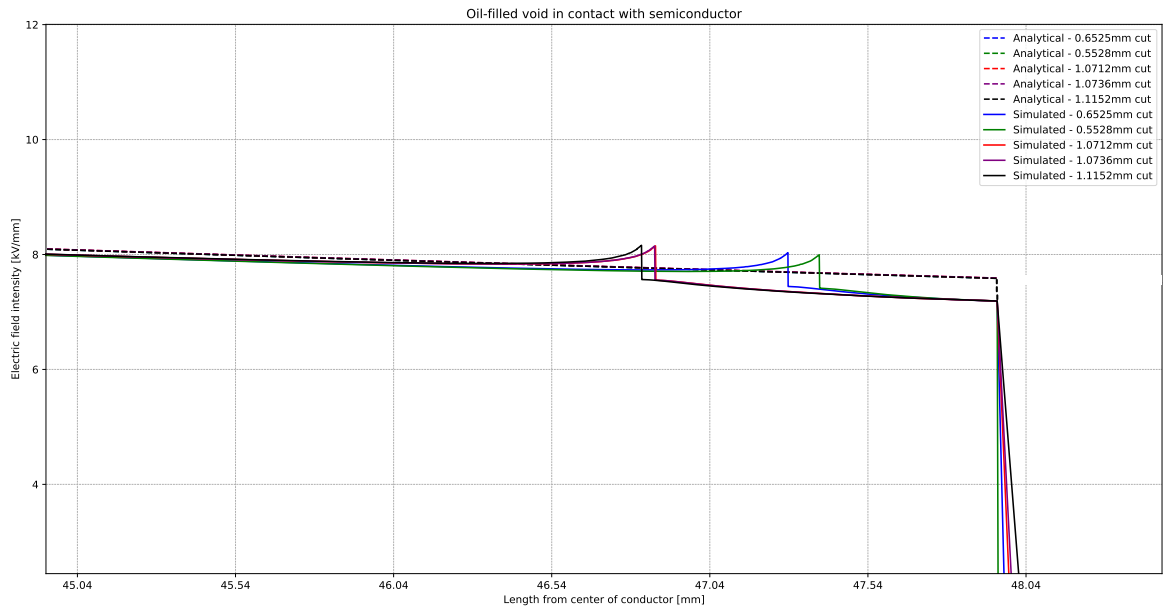Air-filled void in contact with semiconductor, zoomed in.

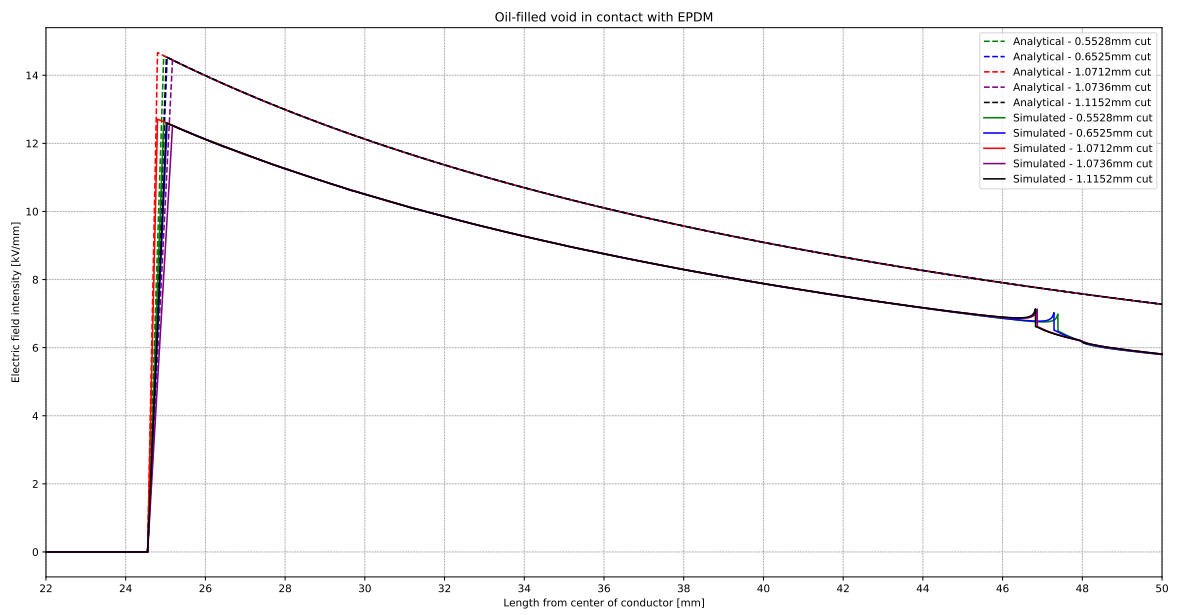Air-filled void in contact with EPDM.

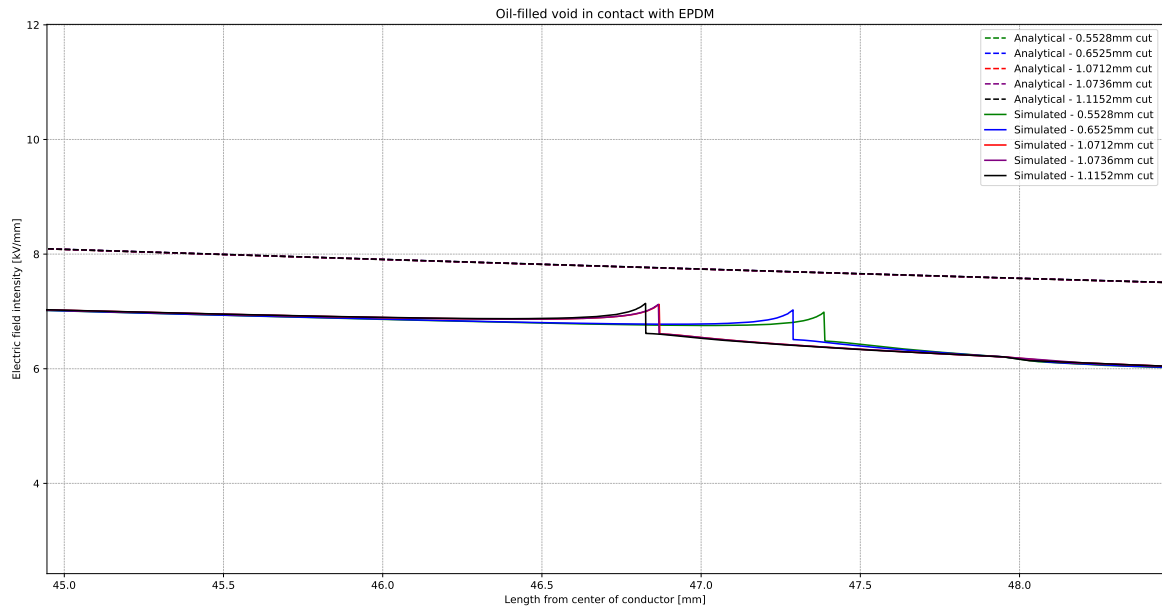Air-filled void in contact with EPDM, zoomed in.

Oil-filled void in contact with semiconductor.

Oil-filled void in contact with semiconductor, zoomed in.

Oil-filled void in contact with EPDM.

Oil-filled void in contact with EPDM, zoomed in.

Appendix D

Python script for calculating FEF and PDIV

The Python script used for importing and plotting the simulated data, as well as calculating the FEF and PDIV is presented below. Some variables are generalized since they depend on the specific simulation data.

```python
import pandas as pd
import matplotlib.pyplot as plt
import numpy as np

excel_file_path = r"filepath.xls"
data = pd.read_excel(excel_file_path, skiprows=1)

x1 = data.iloc[:, 0]
y1 = data.iloc[:, 1]
x2 = data.iloc[:, 2]
y2 = data.iloc[:, 3]
x3 = data.iloc[:, 4]
y3 = data.iloc[:, 5]
x4 = data.iloc[:, 6]
y4 = data.iloc[:, 7]
x5 = data.iloc[:, 8]
y5 = data.iloc[:, 9]

#%% Function for finding local minima and maxima for the electric field intensity

def find_local_extrema(x_series, y_series):
    maxima_data = x_series[(x_series >= 46) & (x_series <= 48)]
    minima_data = x_series[(x_series >= 46) & (x_series <= 48)]
    max_index = y_series[maxima_data.index].idxmax()
    min_index = y_series[minima_data.index].idxmin()
    local_maxima_y = y_series[max_index]
    local_minima_y = y_series[min_index]

    return local_maxima_y, local_minima_y

#%% Function for finding r2

def r2(x_series, y_series):
    minima_range = data[(x_series >= 46) & (x_series <= 48)]
    min_index = minima_range[y_series.name].idxmin()
    local_minima_x = x_series.loc[min_index]
    r2 = local_minima_x

    return r2

#%% Function for calculating gap distance (d)

def total_length(x_series, y_series):
    maxima_range = data[(x_series >= 47) & (x_series <= 48)]
    minima_range = data[(x_series >= 46) & (x_series <= 48)]
    max_index = maxima_range[y_series.name].idxmax()
    min_index = minima_range[y_series.name].idxmin()
    local_maxima_x = x_series.loc[max_index]
    local_minima_x = x_series.loc[min_index]
    total_length = local_maxima_x
    d = (total_length - local_minima_x) #[mm]

    return d

#%% Function for calculating breakdown voltage based on Paschen's Law
```

```python
57  def V_breakdown(d):
58      A = 1130 # [1/(mm bar)]
59      B = 27.4 # [kV/(mm bar)]
60      gamma = 0.025
61      p = 3 # [bar]
62      p_d = p*d # [mm bar]
63      Vb = (B * p_d) / (np.log((A * p_d) / np.log(1 + (1 / gamma))))
64
65      return Vb
66
67  #%% Analytical calculation of the electric field, with no cuts
68
69  def E(x, r1, r2):
70      V = 240e3 # [V]
71      r1_m = r1 / 1000  # Convert r1 from mm to meters
72      r2_m = r2 / 1000  # Convert r2 from mm to meters
73      x_m = x / 1000    # Convert x from mm to meters
74
75      E_field = np.zeros_like(x_m)
76      outside_conductor = (x_m > r1_m)
77      E_field[outside_conductor] = V / (np.log(r2_m / r1_m) * x_m[outside_conductor]) / 1e6  # Convert from V/m to MV/m
78
79      return E_field
80
81  #%% Calculating analytically the electric field for all cuts
82
83  r1 = 24.55 # [mm]
84
85  r2_1mm = r2(x1,y1)
86  r2_12mm = r2(x2,y2)
87  r2_14mm = r2(x3,y3)
88  r2_16mm = r2(x4,y4)
89  r2_18mm = r2(x5,y5)
90
91  E_1mm = E(x1, r1, r2_1mm)
92  E_12mm = E(x2, r1, r2_12mm)
93  E_14mm = E(x3, r1, r2_14mm)
94  E_16mm = E(x4, r1, r2_16mm)
95  E_18mm = E(x5, r1, r2_18mm)
96
97  #%% Plotting
98  x_start = 22
99  x_end = 50
100 colors = ['blue', 'green', 'red', 'purple', 'black']  # Define a list of colors for each cut
101 plt.figure(figsize=(12, 6))
102
103 # Plot analytical lines
104 plt.plot(x1, E_1mm, label='Analytical - x mm cut', linestyle='--', color=colors[0])
105 plt.plot(x2, E_12mm, label='Analytical - x mm cut', linestyle='--', color=colors[1])
106 plt.plot(x3, E_14mm, label='Analytical - x mm cut', linestyle='--', color=colors[2])
107 plt.plot(x4, E_16mm, label='Analytical - x mm cut', linestyle='--', color=colors[3])
108 plt.plot(x5, E_18mm, label='Analytical - x mm cut', linestyle='--', color=colors[4])
109
110 # Plot simulated lines
111 plt.plot(x1, y1, label='Simulated - x mm cut', color=colors[0])
112 plt.plot(x2, y2, label='Simulated - x mm cut', color=colors[1])
113 plt.plot(x3, y3, label='Simulated - x mm cut', color=colors[2])
114 plt.plot(x4, y4, label='Simulated - x mm cut', color=colors[3])
115 plt.plot(x5, y5, label='Simulated - x mm cut', color=colors[4])
116
117 plt.title('X-filled void in contact with X')
118 plt.xlabel('Length from center of conductor [mm]')
119 plt.ylabel('Electric field intensity [kV/mm]')
120 plt.xlim(x_start, x_end)
121 plt.xticks(np.arange(x_start, x_end, step=2))
122 plt.grid(True, which='both', axis='both', linestyle='--', linewidth=0.5)
123 plt.legend()
124 plt.show()
125
126 #%% Function for calculating FEF
127
128 def calculate_FEF(x_simulated, y_simulated, x_analytical, y_analytical, x_range=(47, 49)):
129
130     mask_sim = (x_simulated >= x_range[0]) & (x_simulated <= x_range[1])
131     mask_ana = (x_analytical >= x_range[0]) & (x_analytical <= x_range[1])
132     x_sim_restricted = x_simulated[mask_sim]
133     y_sim_restricted = y_simulated[mask_sim]
134     y_ana_restricted = y_analytical[mask_ana]
135     max_sim_y = np.max(y_sim_restricted)
136     max_sim_pos_index = np.argmax(y_sim_restricted.values)
137     max_sim_x = x_sim_restricted.iloc[max_sim_pos_index]
138     closest_x_ana_pos_index = (np.abs(x_analytical[mask_ana].values - max_sim_x)).argmin()
139     y_ana_restricted = pd.Series(y_ana_restricted)
140     max_ana_y = y_ana_restricted.iloc[closest_x_ana_pos_index]
141     FEF = max_sim_y / max_ana_y
142
```

```python
143        return FEF
144
145 #%% FEF calculations
146
147 FEF_1mm = calculate_FEF(x1, y1, x1, E_1mm)
148 FEF_12mm = calculate_FEF(x2, y2, x2, E_12mm)
149 FEF_14mm = calculate_FEF(x3, y3, x3, E_14mm)
150 FEF_16mm = calculate_FEF(x4, y4, x4, E_16mm)
151 FEF_18mm = calculate_FEF(x5, y5, x5, E_18mm)
152 print("FEF for 1.0mm cut is:", np.round(FEF_1mm,3))
153 print("FEF for 1.2mm cut is:", np.round(FEF_12mm,3))
154 print("FEF for 1.4mm cut is:", np.round(FEF_14mm,3))
155 print("FEF for 1.6mm cut is:", np.round(FEF_16mm,3))
156 print("FEF for 1.8mm cut is:", np.round(FEF_18mm,3))
157
158 #%% PDIV calculations
159
160 d_1mm = total_length(x1, y1) #[mm]
161 d_12mm = total_length(x2, y2) #[mm]
162 d_14mm = total_length(x3, y3) #[mm]
163 d_16mm = total_length(x4, y4) #[mm]
164 d_18mm = total_length(x5, y5) #[mm]
165
166 Vb_1mm = V_breakdown(d_1mm)
167 Vb_12mm = V_breakdown(d_12mm)
168 Vb_14mm = V_breakdown(d_14mm)
169 Vb_16mm = V_breakdown(d_16mm)
170 Vb_18mm = V_breakdown(d_18mm)
171
172 E_bd_1mm = (Vb_1mm*1000)/d_1mm
173 E_bd_12mm = (Vb_12mm*1000)/d_12mm
174 E_bd_14mm = (Vb_14mm*1000)/d_14mm
175 E_bd_16mm = (Vb_16mm*1000)/d_16mm
176 E_bd_18mm = (Vb_18mm*1000)/d_18mm
177
178 E_bd_corr_1mm = E_bd_1mm/FEF_1mm
179 E_bd_corr_12mm = E_bd_12mm/FEF_12mm
180 E_bd_corr_14mm = E_bd_14mm/FEF_14mm
181 E_bd_corr_16mm = E_bd_16mm/FEF_16mm
182 E_bd_corr_18mm = E_bd_18mm/FEF_18mm
183
184 PDIV_1mm = (E_bd_corr_1mm*(r1*np.log(r2_1mm/r1)))/1000
185 PDIV_12mm = (E_bd_corr_12mm*(r1*np.log(r2_12mm/r1)))/1000
186 PDIV_14mm = (E_bd_corr_14mm*(r1*np.log(r2_14mm/r1)))/1000
187 PDIV_16mm = (E_bd_corr_16mm*(r1*np.log(r2_16mm/r1)))/1000
188 PDIV_18mm = (E_bd_corr_18mm*(r1*np.log(r2_18mm/r1)))/1000
189
190 print("PDIV for x mm cut is: ", np.round(PDIV_1mm,2), "kV.")
191 print("PDIV for x mm cut is: ", np.round(PDIV_12mm,2), "kV.")
192 print("PDIV for x mm cut is: ", np.round(PDIV_14mm,2), "kV.")
193 print("PDIV for x mm cut is: ", np.round(PDIV_16mm,2), "kV.")
194 print("PDIV for x mm cut is: ", np.round(PDIV_18mm,2), "kV.")
```